Coastal
Marine
Institute

University of Alaska

Water and Ice Dynamics in Cook Inlet

Mark Johnson
Principal Investigator

Final Report
OCS Study MMS 2008-061

June 2008

Minerals Management Service
Department of the Interior

and the

School of Fisheries & Ocean Sciences

University of Alaska Fairbanks

Contact information

email: sharice@sfos.uaf.edu
phone: 907.474.7208
fax: 907.474.7204
Coastal Marine Institute
School of Fisheries and Ocean Sciences
University of Alaska Fairbanks
P. O. Box 757220
Fairbanks, AK 99775-7220

Table of Contents

List of Figures

Chapter 1

Chapter 2

Chapter 3

Chapter 4

List of Tables

Chapter 1

Chapter 2

Chapter 3

Chapter 4

Appendix: Comparison results of simulated and observed tidal ellipses

Executive Summary

To help validate the model and understand better the Cook Inlet tidal rips, 50 drifting buoys were deployed for us by Cook Inlet Spill Prevention and Response, Inc. (CISPRI). Velocities are computed using centered differences. Tidal fronts are typically associated with convergence zones. In Cook Inlet, drifting sea ice tends to collect along tide rip fronts thereby providing strong visual signatures for frontal locations.

A 3-D tidal model (Finite Volume Community Model – FVCOM) of Cook Inlet with spatial resolution of 160 m near the coastline and 13 km along the open boundary has been used to simulate the eight major tidal waves in this region (five semidiurnal and three diurnal). Tidal data are from satellite-based archives of tidal constituents for the Gulf of Alaska and Northern Pacific Ocean. Model results of the tidal elevations and phases of the four major waves are in good agreement with observations. Radar backscatter (brightness) from sea ice is typically larger than from open water. As a consequence, the ice edge (frontal) location exhibits a relatively large spatial gradient in radar backscatter. Frontal locations identified from nine SAR images acquired in February 2002, December 2003, January 2004, and February 2004 show that the greatest number of frontal features occurs in a zone extending southwestward from near the West Foreland to along and beyond the eastern shore of Kalgin Island. This zone roughly corresponds to the location of the West Rip and qualitatively agrees with the buoy observations and model results.

A simple statistical analysis was conducted to estimate the averaged absolute difference and standard deviation between model-predicted and observed Lagrangian velocities for drifters #36190 and #36193 experiments, and results are summarized in Table 2.1. The averaged model-data absolute difference for 4 deployments of drifter #36190 was 30 cm/s for U (east-west component) and 42 cm/s for V (north-south component) for the case with the only tidal force. This difference increased by about 2-3 cm/s when the T/S, winds, and surface heat flux were included. The standard deviation value was about 10 cm/s larger than the absolute difference values. The similar results were also shown for drifter #36193. This error is much smaller than the maximum value of tidal current velocity in the inlet but was the same order of magnitude as wind- and buoyancy-driven subtidal currents, suggesting that it is critical to resolve accurately the subtidal currents in Cook Inlet in order to provide the realistic water transport process in this region.

The results clearly show that the RAMS failed to predict the relatively large wind event even for a short time period of 24 hours. In addition to the wind speed, the model also seemed to have troubles in capturing the right direction during air-frontal passages. For example, in late September, the wind measurement shows a strong southward wind velocity of ~15 m/s at both NSFA2 and AUGA2, but RAMS predicted that the maximum wind velocity was directed eastward. The same evidence occurred in late October and November. In November, the phase of the model-predicted wind seemed to have a shift from the observed wind.

This comparison suggests that the Alaska regional RAMS needs to be improved in order to make it useful to drive the ocean model. A better meso-scale meteorological model system with data assimilation should be developed to provide a reliable and accurate wind field in Cook Inlet for the hindcast application and also ocean model simulation. Our Lagrangian particle tracking experiment clearly shows that the buoyancy- and wind-driven circulations play a critical role for particle trajectories and water transports in Cook Inlet. Without improvement in the meteorological forcing fields, it is impossible to simulate accurately the trajectories of drifters deployed in this region.

Chapter 1: Satellite Tracked Drifting Buoys

Introduction

This chapter summarizes the accomplishments from the satellite tracked drifting buoy portion of this project. Hourly time and position data were acquired from 50 buoys deployed in Cook Inlet beginning in April 2003 and ending in July 2007. Most buoys were deployed south of the Forelands and northeast of Kalgin Island, generally in sets of two or three. Fifteen buoys were equipped with drogues tethered at 7.5 m, 27 buoys had drogues tethered at 5 m, four had drogues tethered at 80 m, and four were without drogues. All buoys were equipped with Global Positioning System and telemetry software/hardware. Hourly GPS position (± 20 m) and time (to the second) were internally stored in the buoy hardware and transmitted several times per day to the ARGOS satellite system. ARGOS is a commercial satellite system designed for the telemetry of data from research projects such as this one. GPS position data were supplemented by position fixes computed by ARGOS positioning. All data were relayed to ground receive stations daily and the raw data were emailed to the PI on the following day. Three buoys failed to transmit data. The time history of data transmission for the remaining buoys is shown in Figure 1.1.

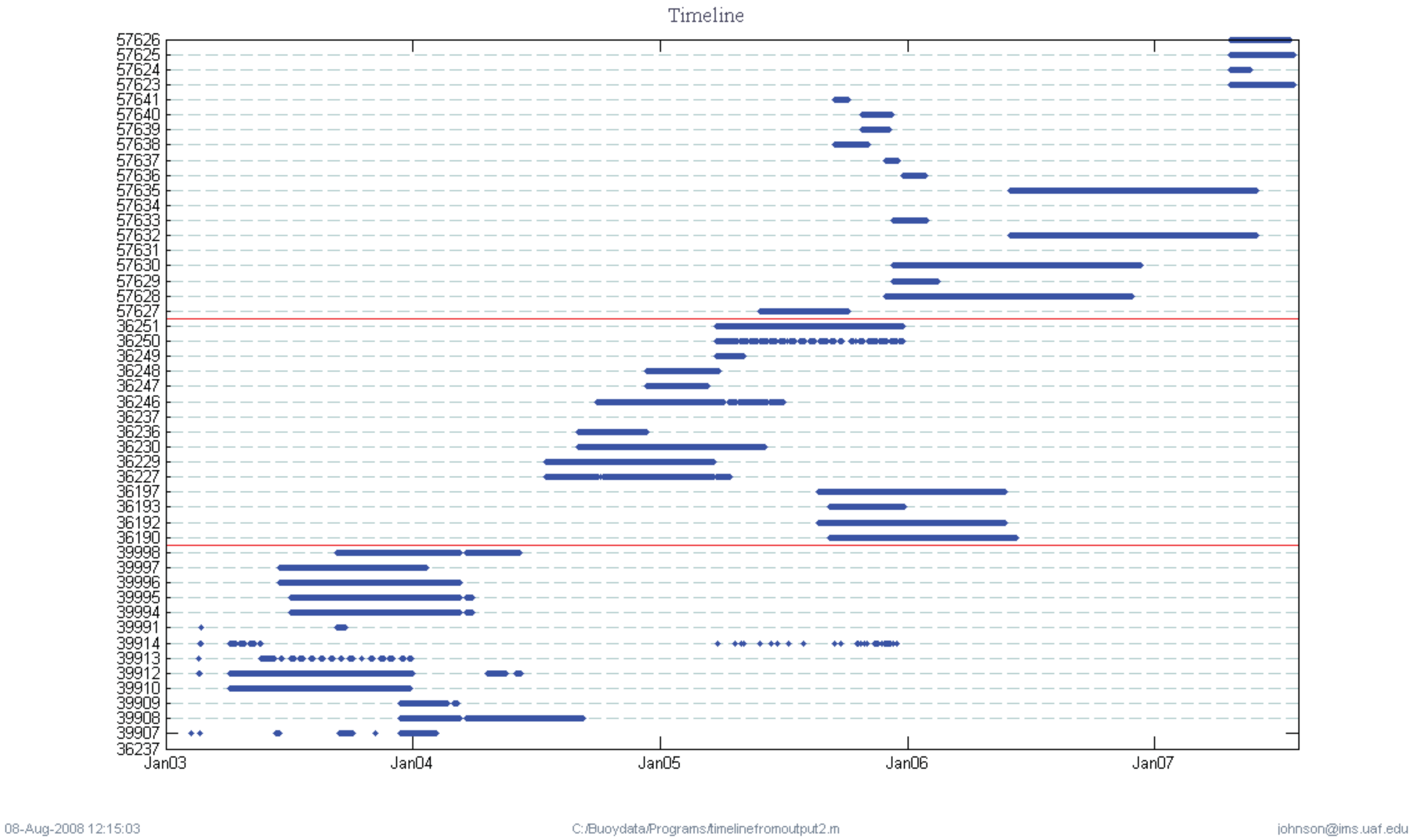

Figure 1.1. Timeline of data transmission from all buoys over the project duration. Buoy ID number is shown at left with time axis along abscissa from January 2003 through August 2007.

Summary

This program acquired 65,375 hours of data from Cook Inlet, the northern Gulf of Alaska, and the Bering Sea. Included are 34,700 hours of position and velocity data in Cook Inlet from The Forelands to Kennedy Entrance and Cape Douglas. The buoy data show a high-energy, high-velocity, and high convergence zone to the east of Kalgin Island aligned in the north-south direction with the bathymetric slope. The data were used to validate two numerical models. The buoy data and the models show that the circulation in Cook Inlet is dominated by tides. Winds and freshwater modify the tidal circulation slightly. Almost all buoys were deployed south of the Forelands, and many transited through Shelikof Strait. Several reached the Bering Sea and one looped counterclockwise around the northern Gulf of Alaska and ended near the Kenai Fjords National Park.

Objectives

The objectives of this program were to use near-surface drifters to identify regions of high tidal energy known as "tide rips" and use the position and velocity data for validation of a 2-D and 3-D numerical model. Comparisons between the model and the buoy data helped identify areas where the model can be improved.

Methodology

Almost all the buoys were initially deployed northeast of Kalgin Island by personnel from Cook Inlet Spill Prevention and Response, Inc. CISPRI provided valuable "in-kind" support for this program and deployed the buoys in accordance with the manufacturer's instructions. A magnet on the bottom of the buoy acts as a switch. When removed, the magnet turns on the internal GPS so it can begin data collection. In most cases, the magnet was removed a day or two in advance of deployment to allow the buoy to initialize with the satellites.

Early in the program, one buoy was deployed during moderate ice but failed almost immediately. We believe that ice destroyed the waterproof casing of the buoy causing it to sink. After that, all deployments were done after most of the ice cleared from Cook Inlet. Two other buoys failed to transmit in Alaska waters. Whether these failures were field or manufacturer related is unknown. Following a discussion with the manufacturer, Technocean, Inc., one of the failed buoys was replaced at no cost to this project.

Once deployed, the buoys drifted with the current at the depth of the drogue. The buoys are engineered to follow the fluid at the drogue depth, and complete engineering details about the drogue's ability to follow water can be found at technocean.com. All buoys were engineered so that the drag from the surface float and tether was small in comparison to the drag from the drogue (i.e. 1/20). The buoys were drogued to follow the current between 5 and 7.5 meters in all but eight cases. Four were drogued at 80 m to provide an estimate of the deep currents, and four were without drogues to provide an estimate of surface drift.

A normally operating drifter acquires GPS position fixes near the top of the hour and stores the data internally. During this project, data were stored in hexadecimal format in year 1, then in decimal format in years two and three. Both approaches minimize internal data storage requirements as well as transmission time to the satellite. The necessary software to process the data into hourly position data was written for this project by Johnson using MATLAB. Hourly GPS positions along with ARGOS satellite positions were transmitted via satellite up to four times daily to the ARGOS Service Center.

To ensure that data were not corrupted during transmission to the satellite or to the ground receive station, the number of bits to be transmitted in each packet was counted and that number was appended to the end of each data packet. As the data stream is processed, we computed the number of bits in each packet and compared that number with the number received at the end of the packet transmission. Only those packets where the transmitted bits agreed with the appended count, the checksum, were retained. About 5% of the data failed the checksum and were discarded and no further processing was done with the failed checksum data. In anticipation of this data loss, data storage in the buoy was intentionally redundant. There were very few data gaps due to transmission errors.

Errors in positioning

After the data were received and the checksum performed, the remaining data were converted to decimal latitude and longitude positions with time (year, month, day, hour, minute, second). The data are approximately hourly, and velocities were computed using centered finite-differences. Despite checksum error detection, the processed data still showed data spikes that cannot be real.

To quantify the position jumps outside of the ~20 m error associated with GPS positioning, we placed a buoy (57632) that had a damaged tether/drogue at CISPRI where it transmitted in a stationary location for 266 days. The resulting position data from a 154 day subset of these data characterize the position errors after all known transmission errors are removed (Figure 1.2). These are the errors inherent in the system used here, and may be due to poor GPS fixes, false acceptance of checksum errors, or processing errors. However, the regular spacing of the errors in Figure 1.2 suggest a precision or rounding error perhaps due to data storage within the buoy itself or truncation due to data transmission.

A histogram of the position data is shown in Figure 1.3 for the full 266 day record from stationary Buoy 57632. Most positions are within a few tens of meters of the mean, as expected. At both ends of the range, however, there are position fixes that are not possible.

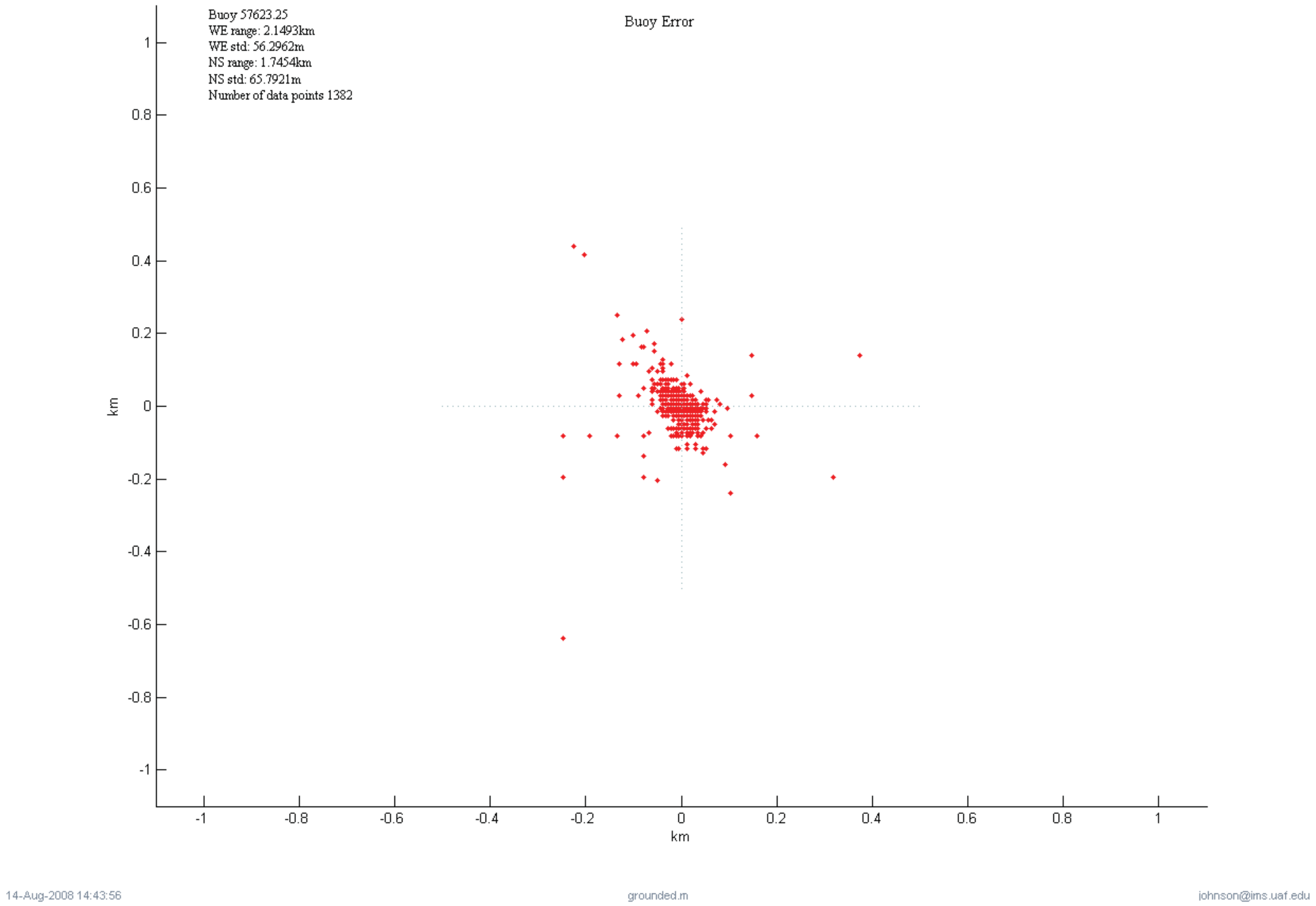

Figure 1.2. Positions on an x-y grid from stationary buoy 57632 over 154 days. Most positions fall within 0.2 km (200 m) of the mean position. The data range is about two km with a standard deviation of about 70 m. The error is larger in the east-west (longitude) dimension.

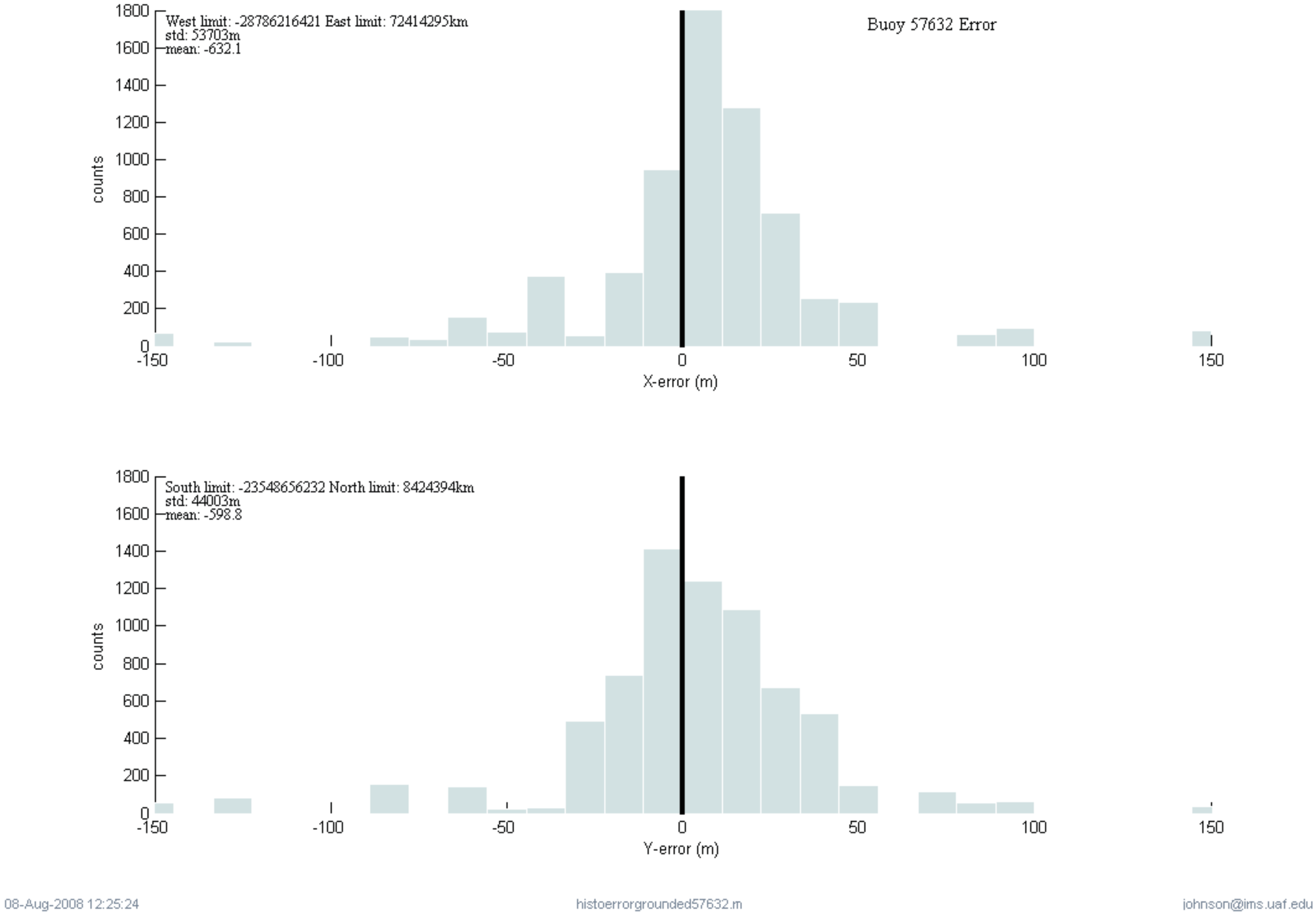

Figure 1.3. Histograms of position errors for stationary buoy 57632. Most position errors are a few tens of meters, in agreement with the GPS error of about twenty meters. Significant data jumps substantially raise the STD and the range of data values spans 100s of km.

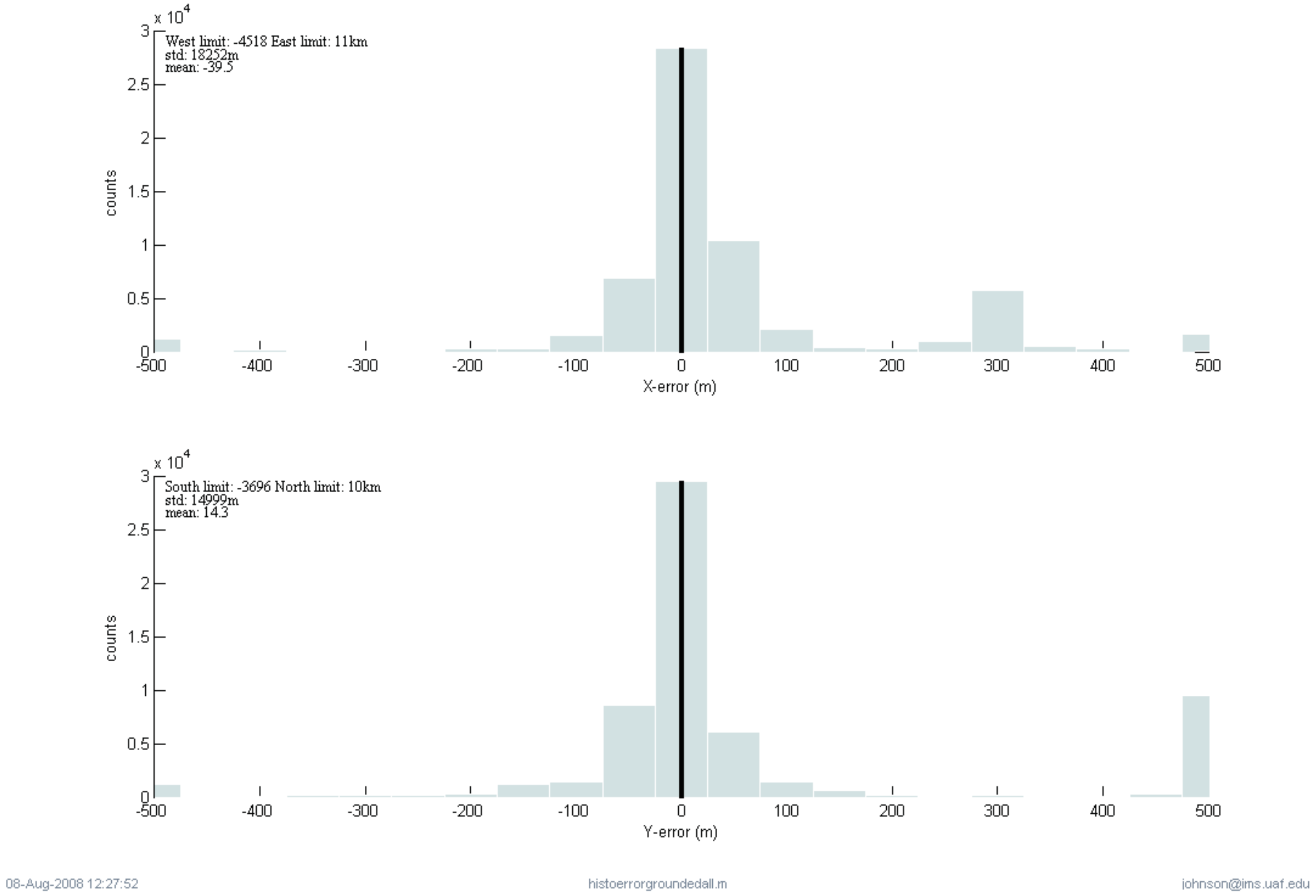

Figure 1.4. Positioning errors computed from all grounded/stationary buoys combined. Most errors are less than 100 m. Some large positioning errors occur, up to 4500 km in the west-east or x-direction and 3700 km in the north-south or y-direction. These large "jumps" were eliminated during visual inspection of the trajectories.

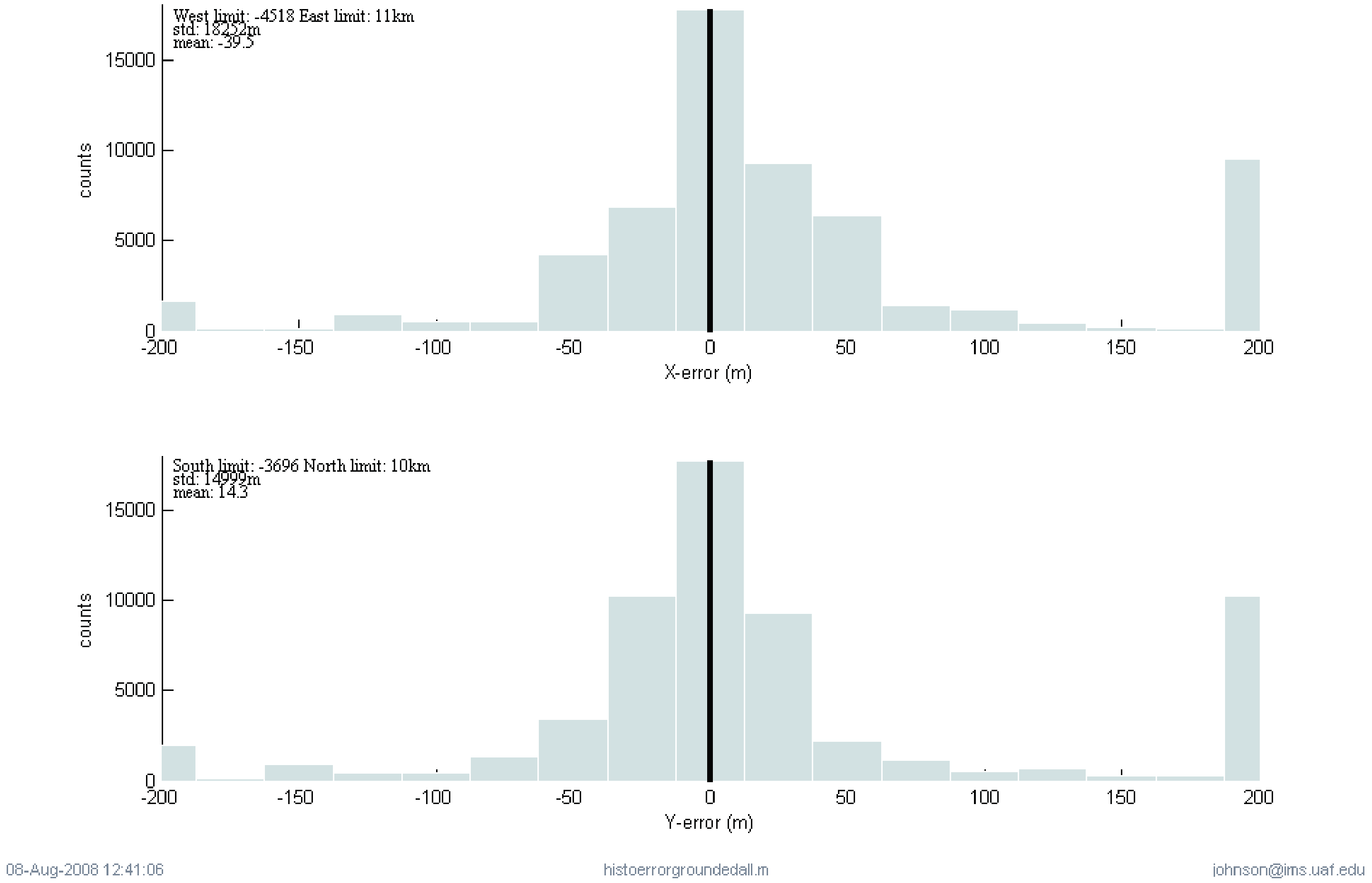

Figure 1.5. Positioning errors as in Figure 1.4 with range expanded about the mean. Note the different errors associated with longitude (top) and latitude (bottom).

To eliminate the remaining position "jumps", the data were further processed numerically to remove them using a cutoff for the computed acceleration. The data were then mapped and visually checked to ensure all abnormal shifts in position were removed. The data discussed in the remaining portion of this report reflect only those data that have been numerically and visually quality checked for accuracy. Data from grounded buoys are not included in the following discussion.

Processed data

The data density by month for buoys in Cook Inlet is shown in the following figures.

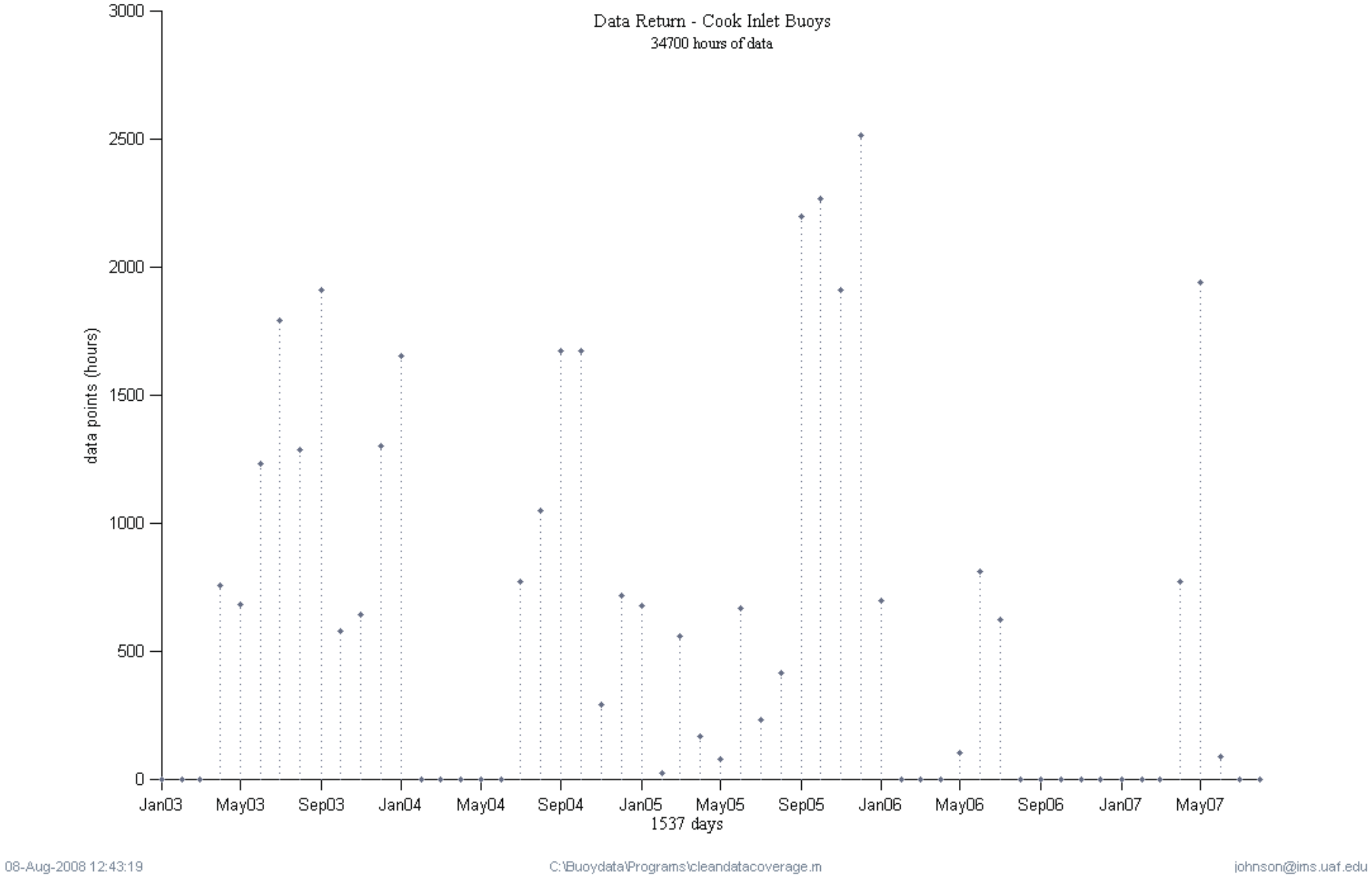

Figure 1.6. Number of data points of hourly data per month for buoys in Cook Inlet.

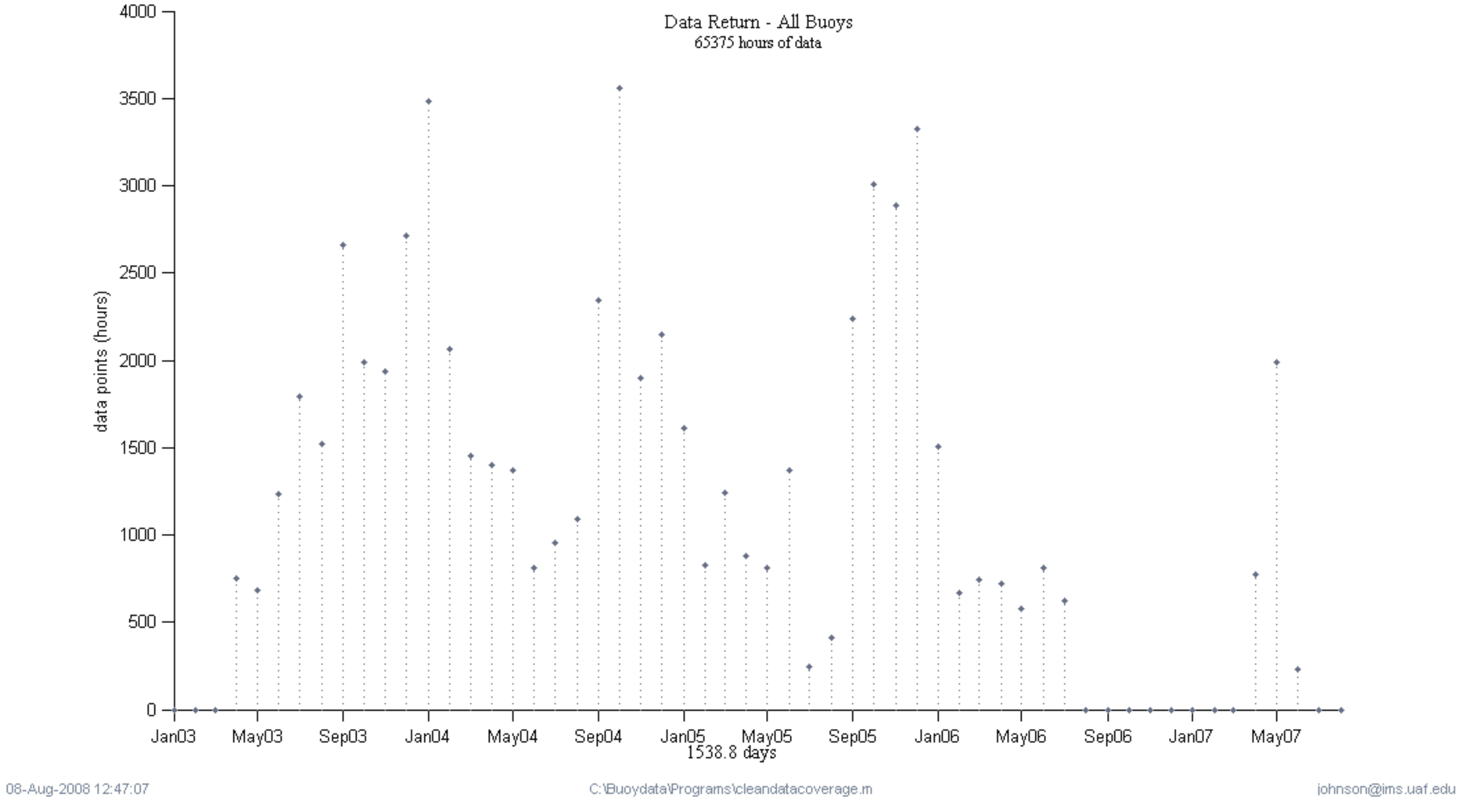

Figure 1.7. Number of data points of hourly data per month for all buoys.

The buoy positions, or trajectories, for the data in Cook Inlet are shown in Figure 1.8. The trajectories from buoys with drogues at 80 m are shown in Figure 1.9. The trajectories for buoys without drogues are shown in Figure 1.10. Figure 1.11 shows the trajectories of all buoys from the Bering Sea to the eastern Gulf of Alaska. All buoys that entered the Gulf of Alaska went through Shelikoff Strait.

A composite of the processed position data (latitude, longitude) and velocities (computed using centered differences) is shown in Figure 1.12.

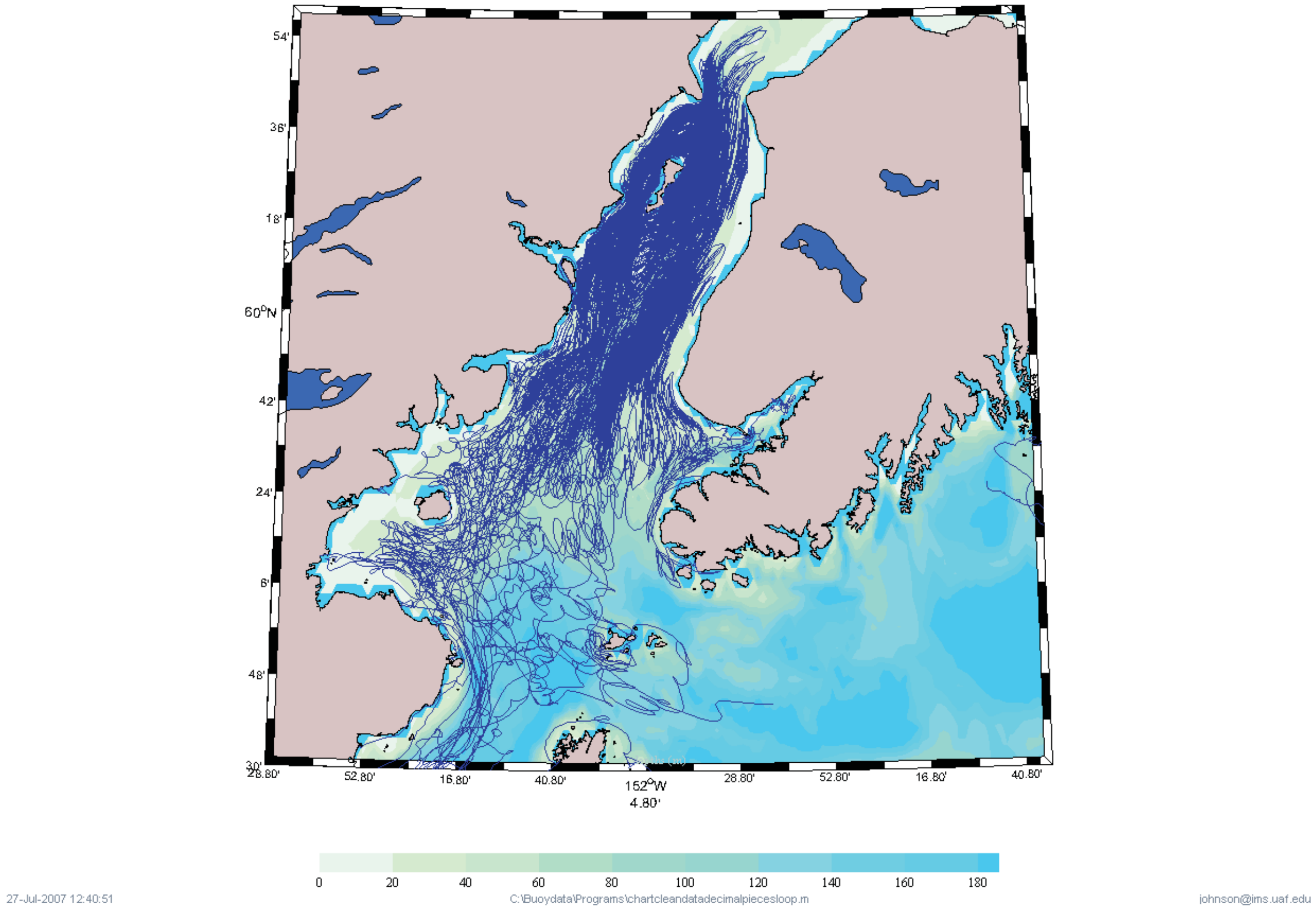

Figure 1.8. Trajectories of all buoys in the Cook Inlet region.

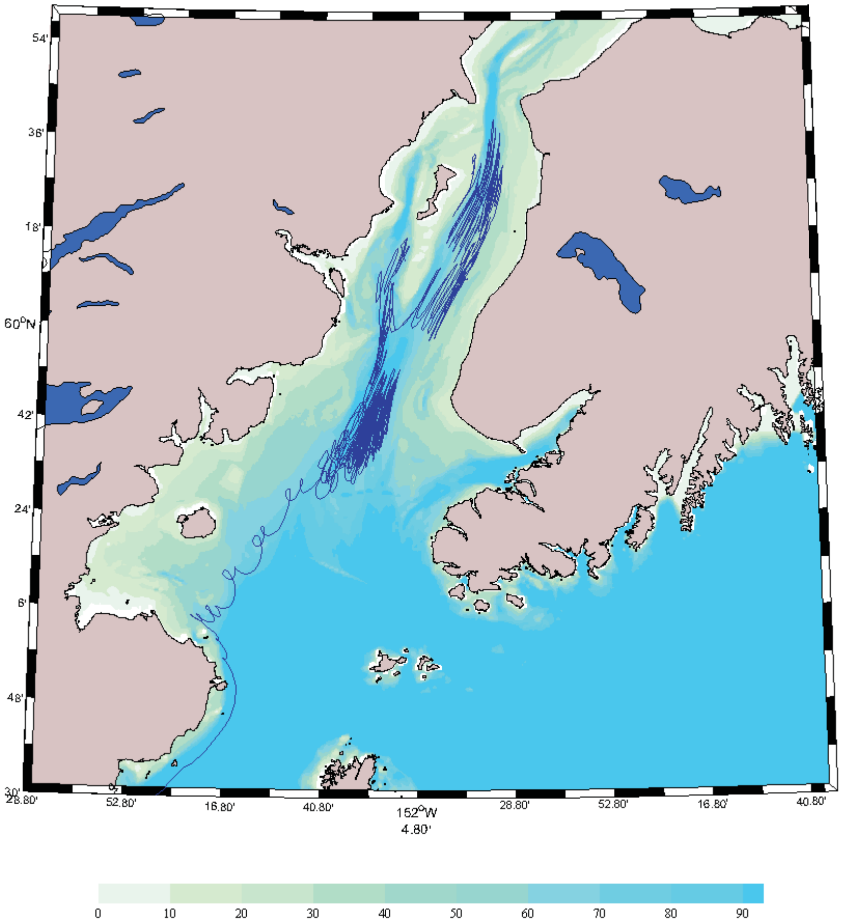

03-Aug-2007 11:07:56 C:\Buoydata\Programs\chartcleandatadecimalpiecesloop.m johnson@ims.uaf.edu

Figure 1.9. Trajectories of buoys with 80 m drogues. Note the alignment with the deep, central channel.

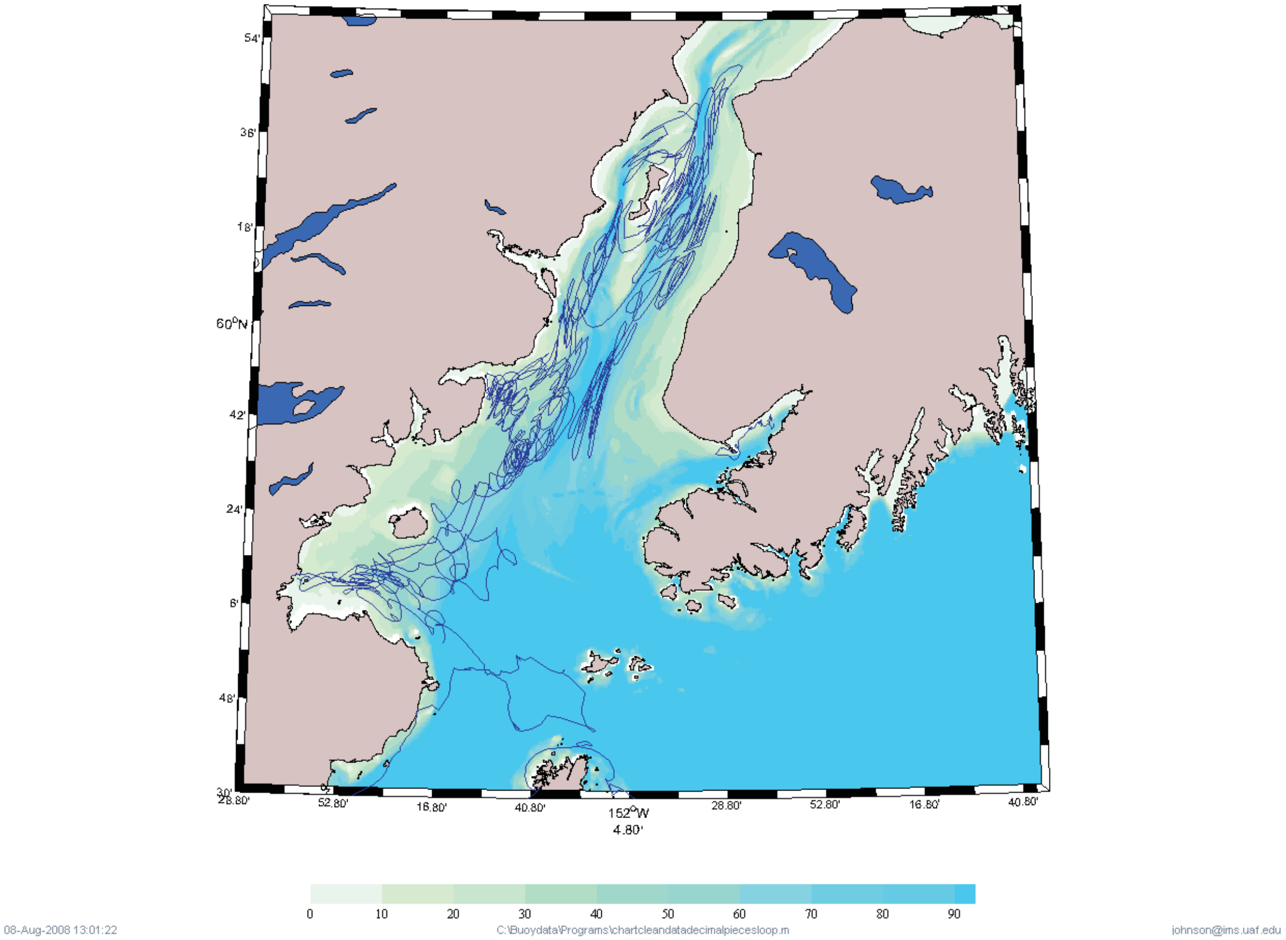

Figure 1.10. Trajectories of buoys without drogues. The behavior of these buoys shows no statistically significant difference from the drogued buoys.

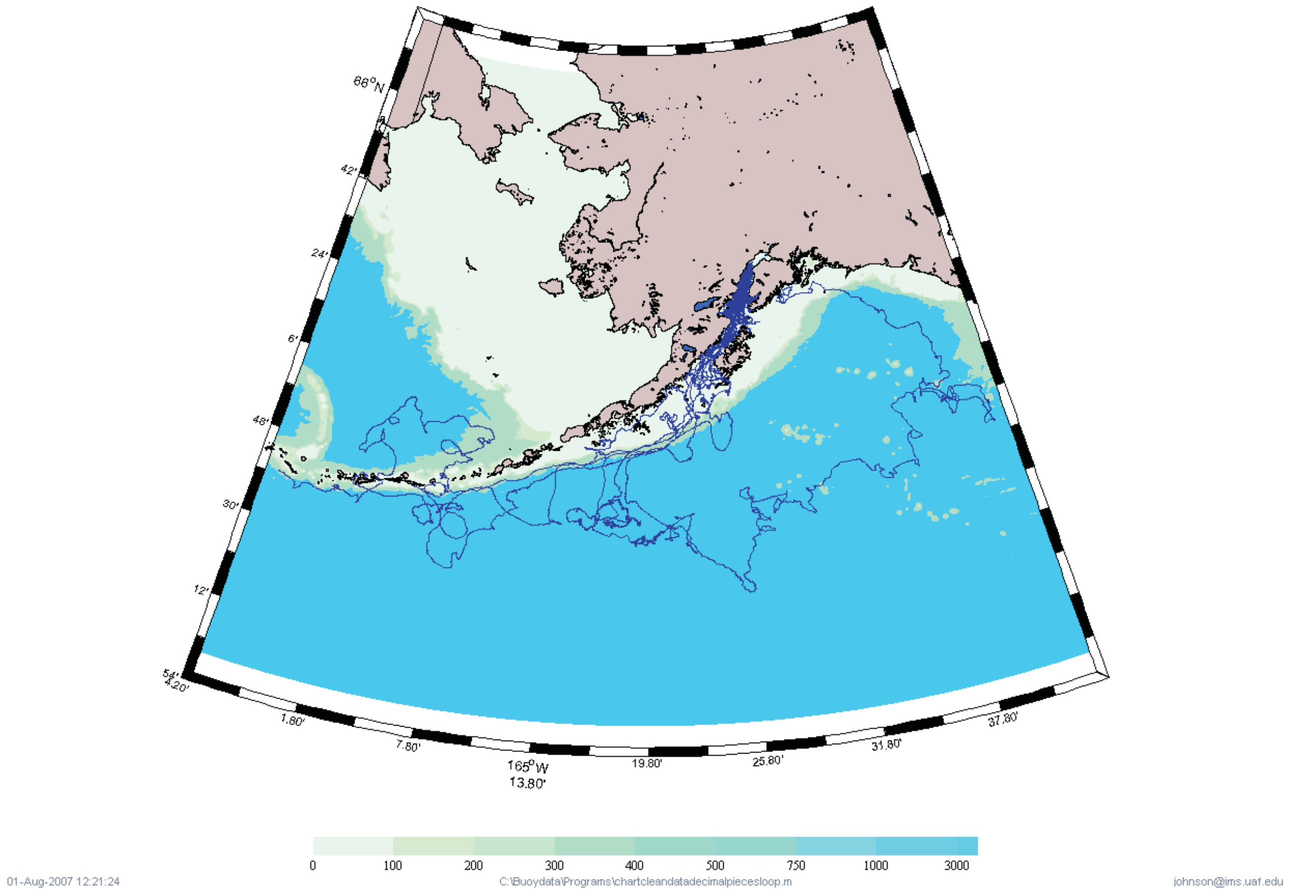

Figure 1.11. Trajectories of all buoys in the full domain. Note the trajectory entering the Bering Sea and returning to the Gulf of Alaska, and the trajectory circulating counter-clockwise in the Gulf of Alaska and returning nearly all the way to Cook Inlet. All buoys exiting Cook Inlet enter Shelikof Strait.

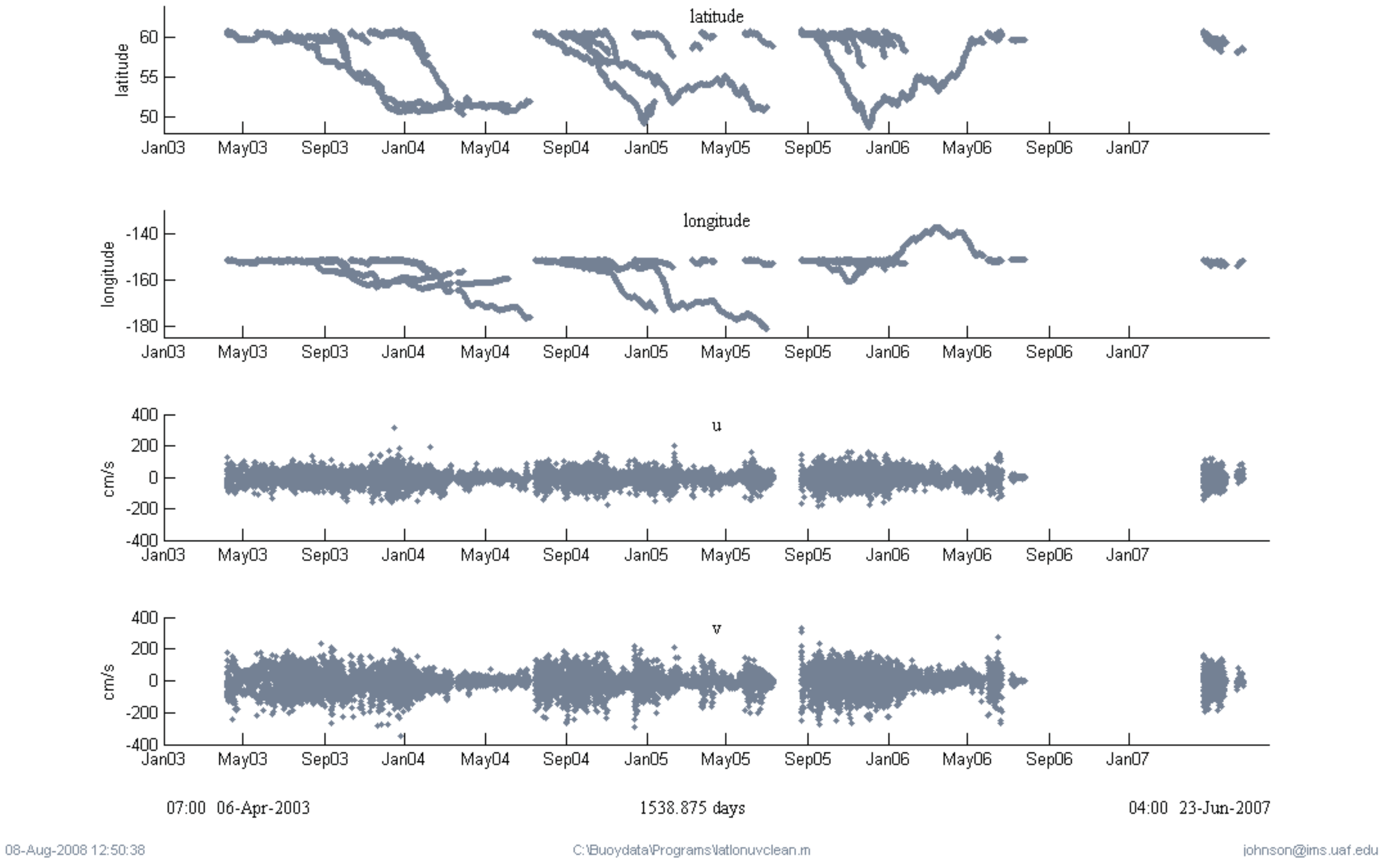

Figure 1.12. Position (latitude and longitude) and velocity (U and V) data over the duration of the program.

Results and Accomplishments

The tide rips are regions of high velocity, aligned primarily with bathymetric slope in the north-south direction. We computed the kinetic energy ($0.5*(U^2 + V^2)^{1/2}$) from all the buoy data and a histogram of the KE is shown in Figure 1.13. Contours of kinetic energy (Figure 1.14) reveal a narrow, north-south aligned high energy region along the sloping bathymetry aligned along the central Inlet. (See also close up in Figure 1.15.)

The currents converge at the surface of the tidal rips and accumulate surface debris, along with the drifters. Figure 1.16 shows the counts of hourly observations per unit area from the buoy positions. It is consistent with the placement of the rip from Figures 1.14 and 1.15.

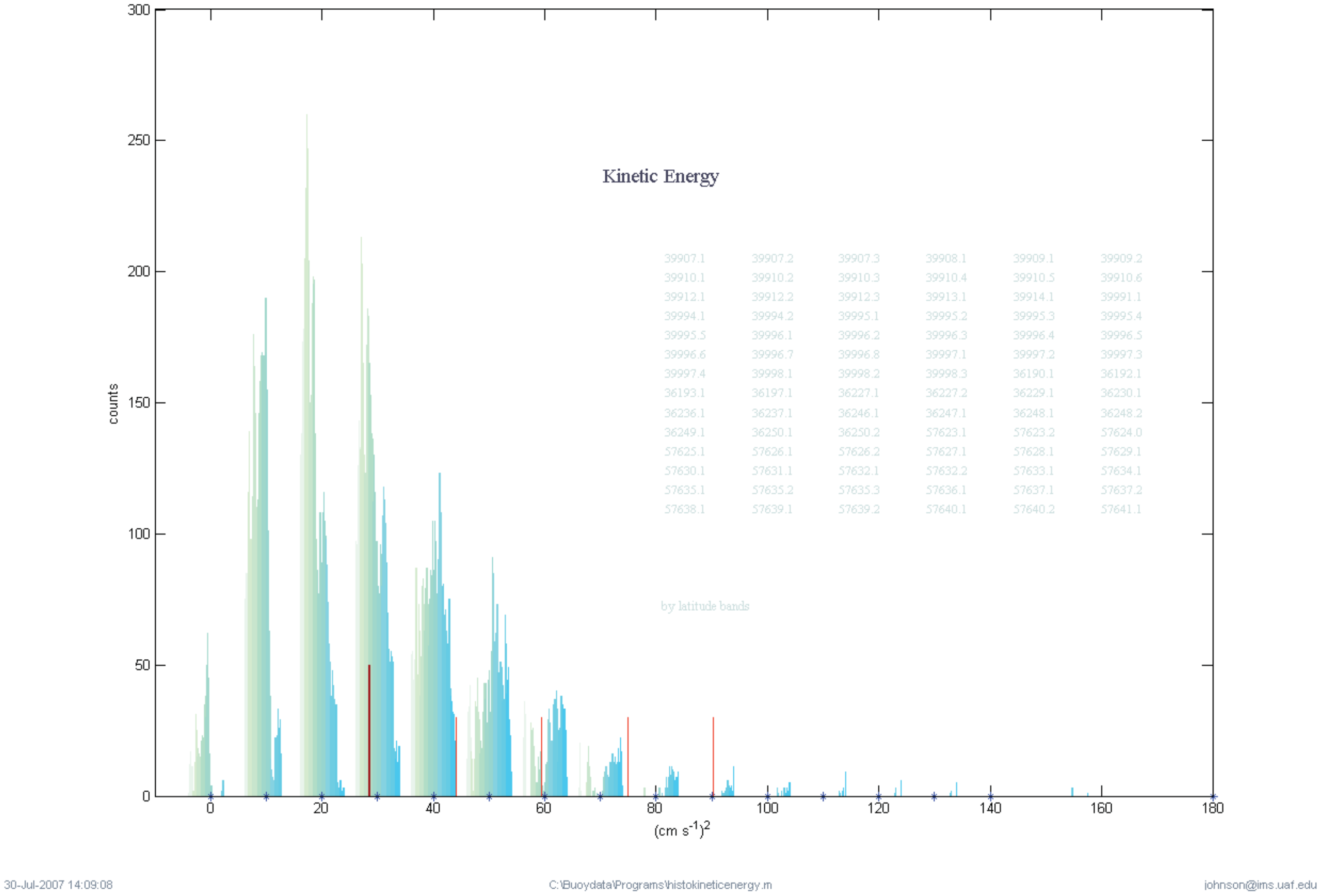

Figure 1.13. Histogram of the buoy kinetic energy. The mean falls at the heavy red line, about 29 $(\mathrm{cm/s})^2$, and the thinner red lines mark standard deviations (1, 2, 3 and 4) above the mean. The values above 100 $(\mathrm{cm/s})^2$ are from the regions generally associated with the tide rips and are contoured in Figures 1.14 and 1.15.

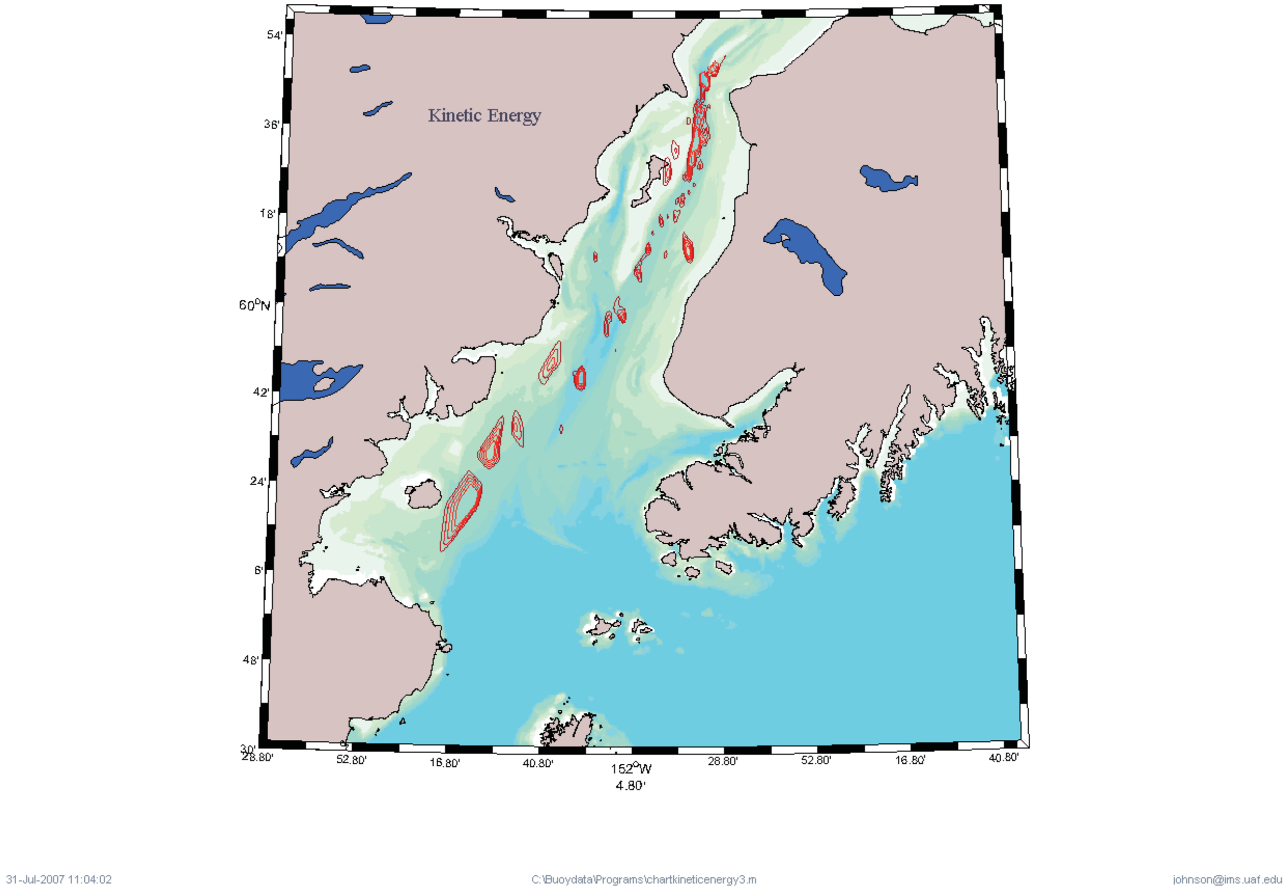

Figure 1.14. Kinetic energy contours. Data valued above 100 $(cm/s)^2$ have been contoured. The high values of KE align with the slope in the Cook Inlet bathymetry.

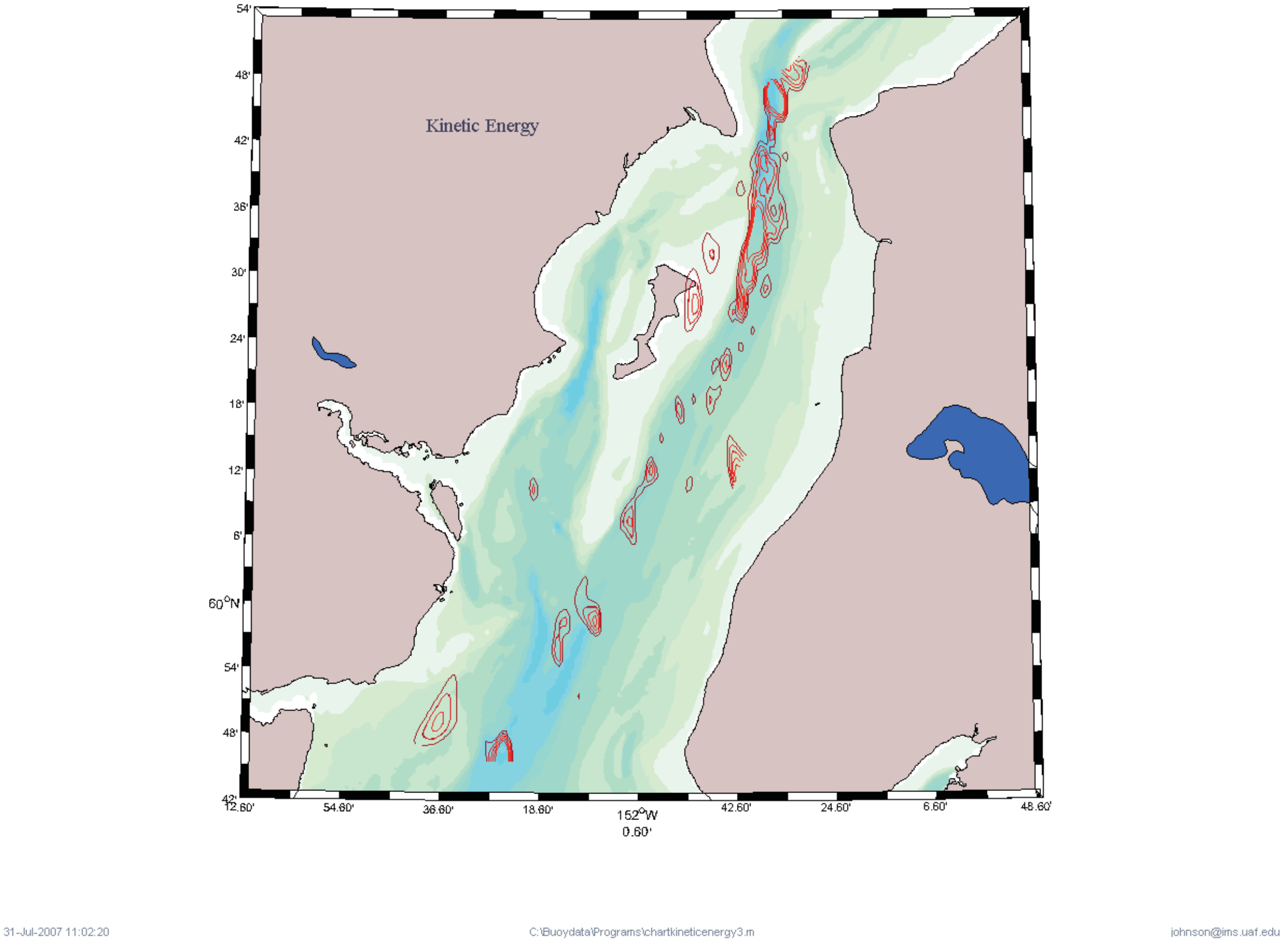

Figure 1.15. Kinetic energy as in Figure 1.13 showing close-up around Kalgin Island.

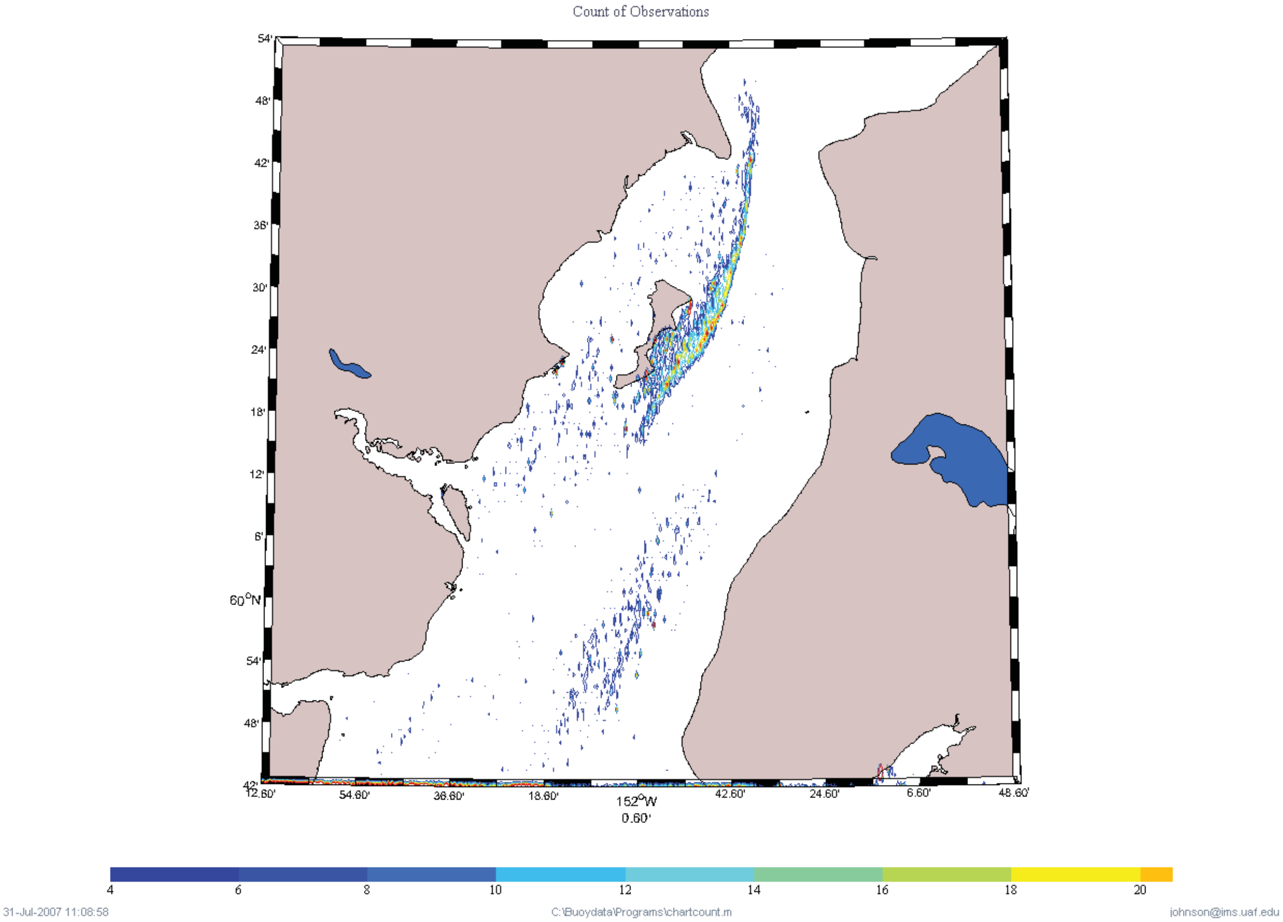

Figure 1.16. Counts of hourly position data showing regions of convergence. Note similarity between regions of convergence and regions of high kinetic energy.

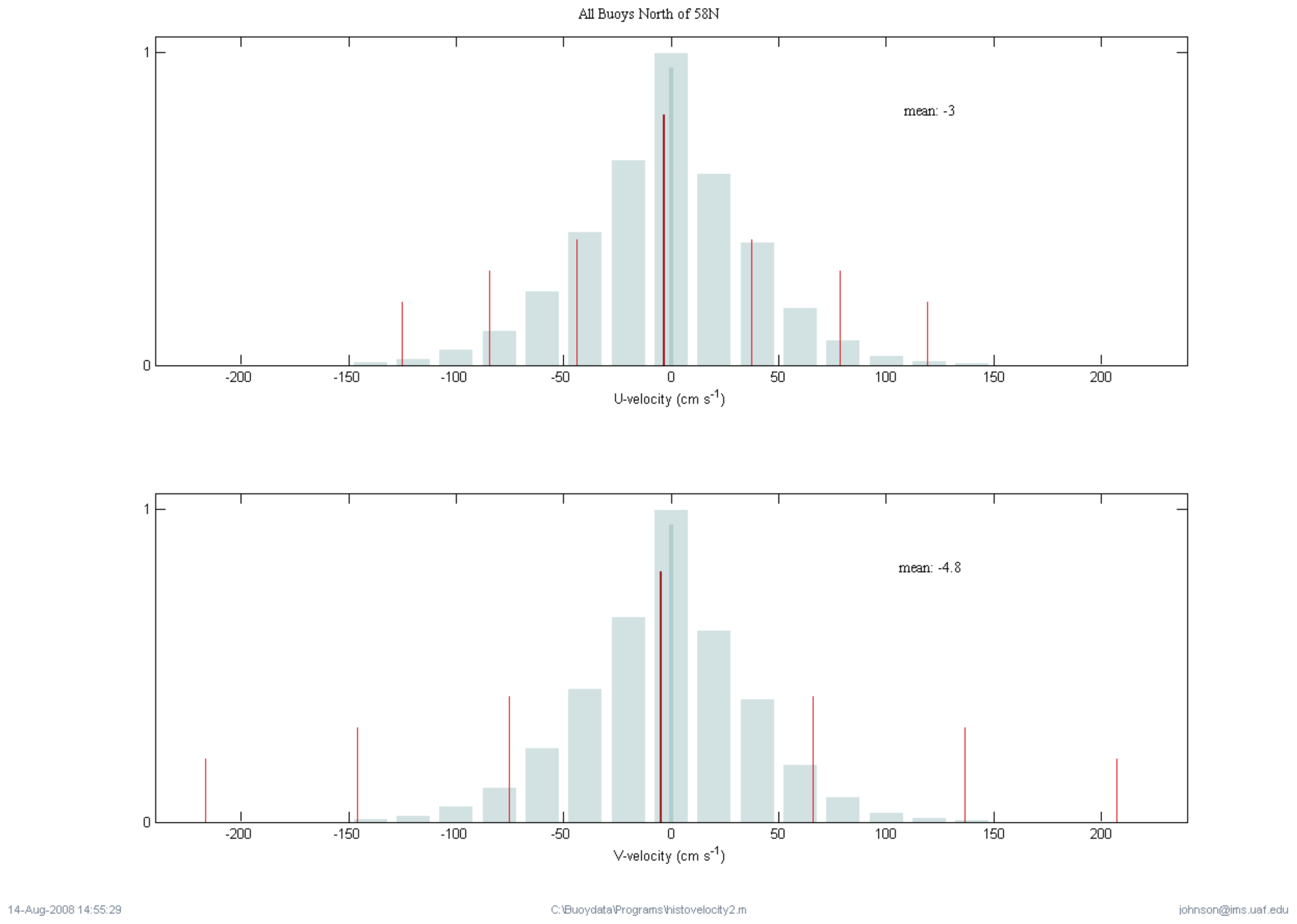

Figure 1.17. Mean (dark red line) west-east velocity (U) and mean north-south (V) velocity for all buoys north of 58N in Cook Inlet. Lighter red lines are standard deviation increments.

The histograms for the north-south (V) and the west-east (U) velocity for all buoy observations are shown in Figure 1.17. The mean north-south velocity is 4.7 cm/s to the south and the mean west-east velocity is 3 cm/s to the west. Figure 1.18 shows the mean west-east velocity for all buoys without drogues. There is not statistical difference between the velocities from drogued and undrogued buoys. The mean, rectified flow in Cook Inlet, north of 58N to the Forelands, is to the south-southwest, out of Cook Inlet.

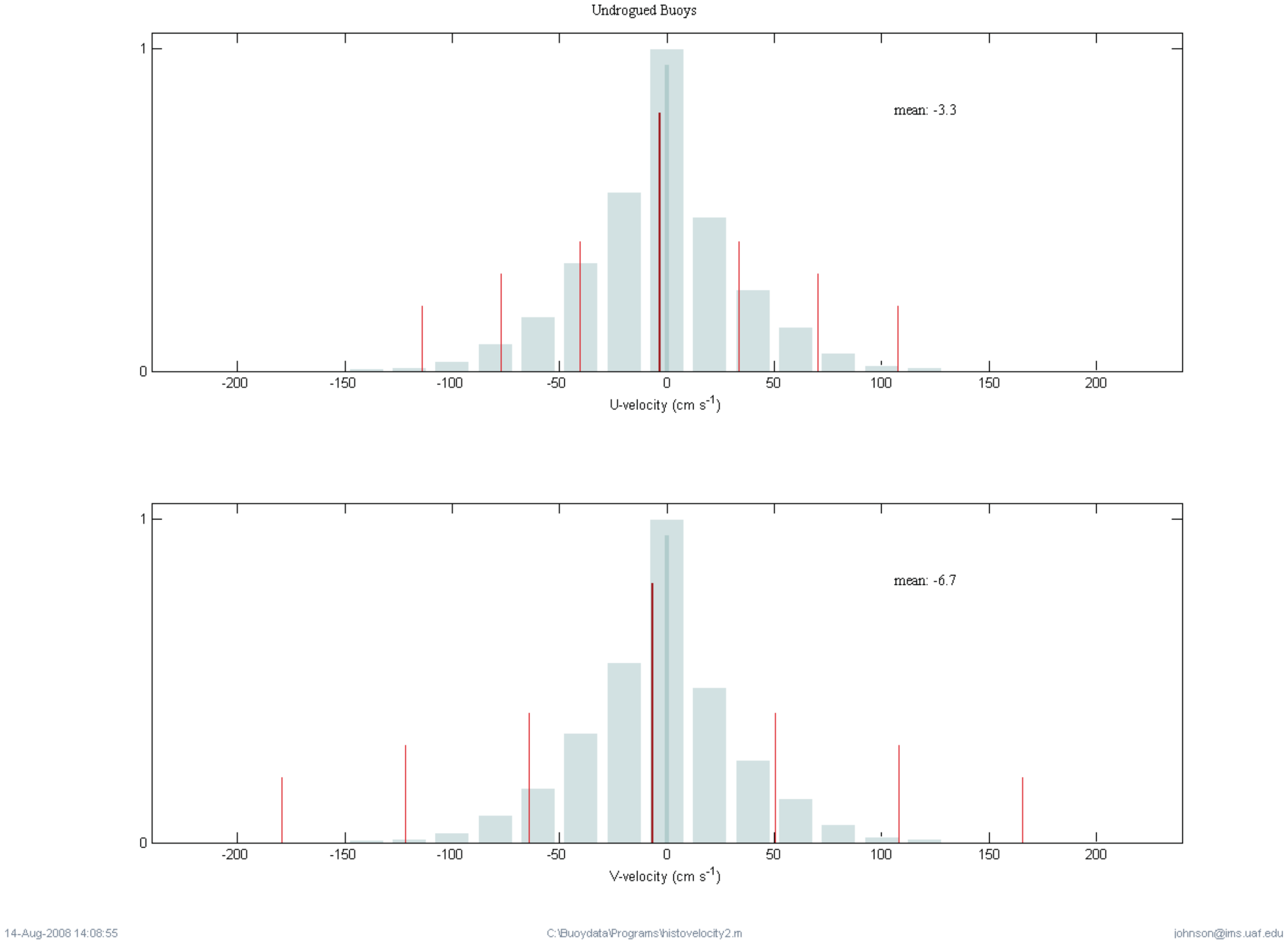

Figure 1.18. Mean (dark red line) west-east velocity (U) and mean north-south (V) velocity for all buoys without drogues. Lighter red lines are standard deviation increments. There is no statistical difference between the drogued and undrogued velocities.

The mean flow from the above histograms is consistent with the surface plot of direction from all the drifters (Figure 1.19). In general, the flow enters in the east and flows to the north and exits southward in the western Inlet.

Remarks and Recommendations

This program has clearly identified the high velocity, high energy, high convergence zone in central Cook Inlet that runs from the Forelands to Kalgin Island and south towards the east of St. Augustine Island. Tides dominate the flow in Cook Inlet, and a tide model could be maintained on-line to predict future tidal trajectories that would take minimal processing time, unlike a fully 3-D wind-forced tidal model. A tide-only model could be coupled to the knowledge of the location of the convergence zones shown in this report to identify potential targets to focus on recovery or containment of marine pollution.

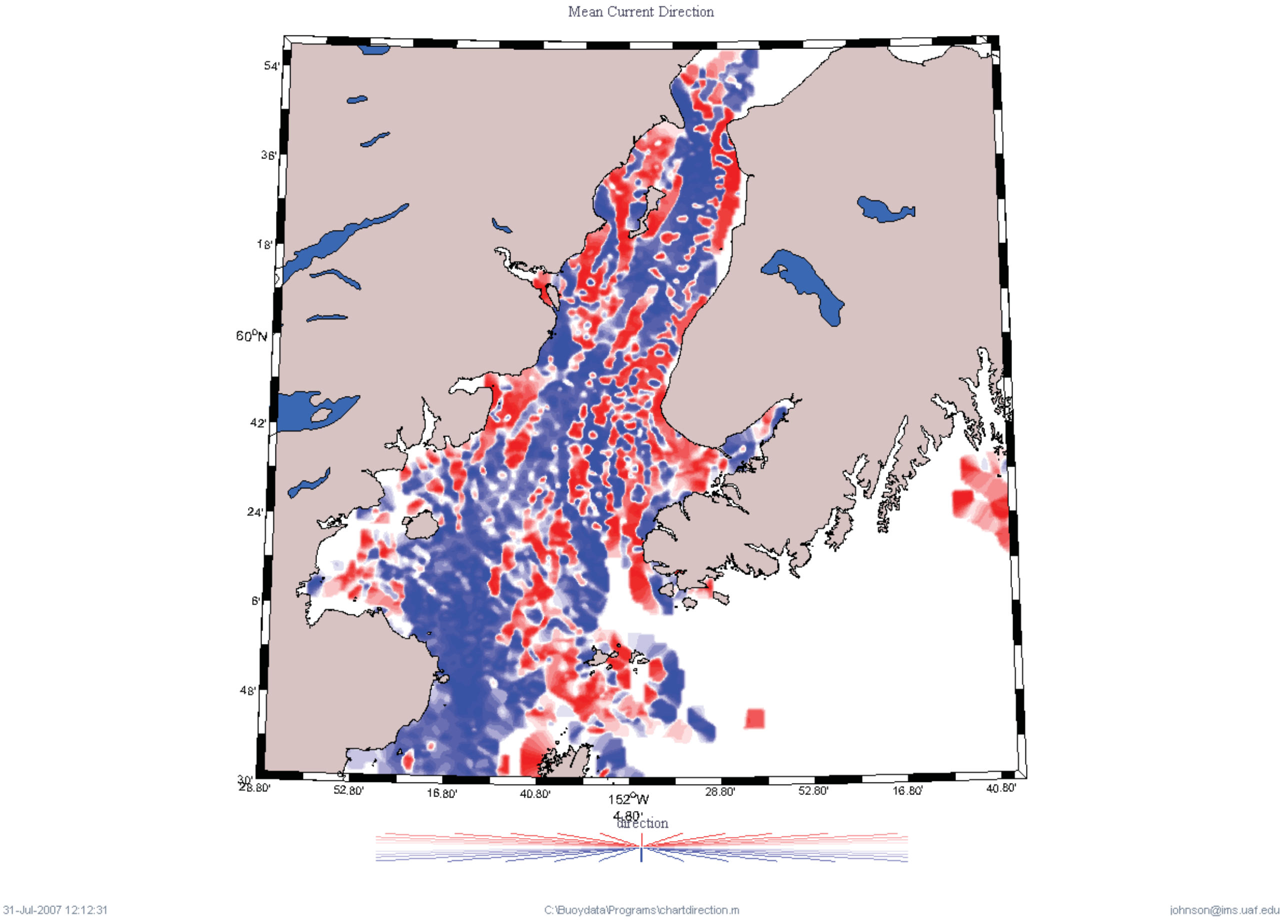

Figure 1.19. The time-averaged direction of the flow. Northward flow is shown in red and southward in blue. Most of the flow exits in the west of the Inlet, with most of the northward flow to the east. There is a mean southward flow along the central deep-channel in Cook Inlet.

Most buoys became grounded at some point in their lifecycle and then did not provide data on the flow characteristics. Several individuals (S.Okkonen, S.Pegau, C.Schoch. B.Foy) and three groups (CISPRI, CIRCAC, The Silver Salmon Creek Lodge) were helpful in recovering grounded buoys and redeploying them in Cook Inlet. The time and cost for buoy recovery was substantial, exceeding what was anticipated during the proposal stage of this program. A future program might seek additional funding to increase the buoy numbers and accept this loss to grounding, or fund an aggressive effort to recover and redeploy grounded buoys and increase the data return. This program acquired 34,700 hours of position and velocity data in Cook Inlet, and 65,375 hours of data overall.

The buoy trajectory paths covered much of lower Cook Inlet. Exiting Cook Inlet, buoys drifted west in Shelikoff Strait, with several advecting west along the Aleutian chain. Several buoys drifted south into the Gulf of Alaska after exiting Shelikoff Strait. One buoy completed nearly a full circuit in the northern Gulf of Alaska to return just east of Kennedy Entrance. This demonstrates a remarkably wide range of trajectories for objects in the upper ocean, given a starting location just south of The Forelands in Cook Inlet.

Table 1.1. Buoy number, drogue depth, and transmission record.

	Buoy	Drogue	First Transmission	Last Transmission
Year 1	39907	7.5m	14DEC03, 10:00UTC	04FEB04, 13:00UTC
	39908	7.5m	14DEC03, 10:00UTC	09SEP04, 02:00UTC
	39909	7.5m	14DEC03, 10:00UTC	07MAR04, 23:00UTC
	39910	7.5m	06APR03, 00:00UTC	28DEC03, 14:00UTC
	39911	7.5m	none	
	39912	7.5m	06APR03, 00:00UTC	08JUN04, 21:26UTC
	39913	7.5m	21MAY03, 06:00UTC	30DEC03, 12:19UTC
	39914	7.5m	06APR03, 03:00UTC	16DEC05, 22:00UTC
	39990	7.5m	Failed in ice	
	39991	7.5m	10SEP03, 16:00UTC	24SEP04, 02:00UTC
	39994	7.5m	05JUL03, 05:00UTC	29MAR04, 23:00UTC
	39995	7.5m	05JUL03, 05:00UTC	30MAR04, 01:00UTC
	39996	7.5m	17JUN03, 15:00UTC	10MAR04, 23:00UTC
	39997	7.5m	17JUN03, 15:00UTC	20JAN04, 11:00UTC
	39998	7.5m	10SEP03, 16:00UTC	06JUN04, 14:06UTC
Year 2	36190	5m	08SEP05, 06:04UTC	11JUN06, 01:11UTC
	36192	5m	22AUG05, 00:04UTC	24MAY06, 23:01UTC
	36193	5m	08SEP05, 06:04UTC	27DEC05, 06:00UTC
	36197	5m	22AUG05, 00:04UTC	25MAY06, 00:00
	36227	5m	15JUL04, 11:04UTC	12APR05, 20:02UTC
	36229	5m	15JUL04, 12:00UTC	20MAR05, 13:00UTC
	36230	5m	01SEP04, 15:04UTC	04JUN05, 15:00UTC
	36236	5m	01SEP04, 15:04UTC	11DEC04, 13:00UTC
	36237	5m	28SEP04, 22:00UTC	01JUL05, 16:00UTC
	36246	5m	29SEP04, 00:04UTC	01JUL05, 01:00UTC

	36247	5m	12DEC04, 15:04UTC	12MAR05, 01:00UTC
	36248	5m	12DEC04, 05:04UTC	28MAR05, 13:01UTC
	36249	80m	23MAR05, 22:04UTC	03MAY05, 23:00UTC
	36250	80m	23MAR05, 22:04UTC	24DEC05, 14:01UTC
	36251	80m	23MAR05, 22:02UTC	24DEC05, 15:02UTC
	36261	80m	none	
Year 3	57627	5m	28MAY05, 04:04UTC	05OCT05, 22:23UTC
	57628	5m	29NOV05, 00:00UTC	30JAN06, 19:00UTC
	57629	5m	11DEC05, 4:42UTC	30JAN06, 20:34UTC
	57630	5m	11DEC05, 01:03UTC	30JAN06, 20:52UTC
	57631	5m	11DEC05, 01:03UTC	30JAN06, 19:00UTC
	57632	5m	31MAY06, 16:04UTC	30MAY07, 23:20UTC
	57633	5m	11DEC05, 02:04UTC	28JAN06, 21:01UTC
	57634	5m	24DEC05, 14:04UTC	30JAN06, 19:00UTC
	57635	5m	31MAY06, 16:04UTC	30MAY07, 23:07UTC
	57636	5m	24DEC05, 14:02UTC	27JAN06, 17:00UTC
	57637	5m	28NOV05, 23:04UTC	17DEC05, 23:01UTC
	57638	5m	15SEP05, 21:04UTC	03NOV05, 18:00UTC
	57639	5m	25OCT05, 19:49UTC	05DEC05, 23:03UTC
	57640	5m	25OCT05, 19:42UTC	07DEC05, 23:17UTC
	57641	5m	15SEP05, 21:45UTC	04OCT05, 23:24UTC
	57623	surface	22APR07, 04:04UTC	24JUL07, 21:00UTC
	57624	surface	22APR07, 03:04UTC	21May07, 22:58UTC
	57625	surface	22APR07, 03:04UTC	24JUL07, 23:00UTC
	57626	surface	22APR07, 04:04UTC	20JUL07, 20:04UTC

Chapter 2: Modeling Experiments in Cook Inlet

Abstract

This report summarizes our accomplishments in 1) development and validation of an unstructured grid finite-volume coastal ocean model (FVCOM) in Cook Inlet; 2) process-oriented experiments with focus on tide- and wind-induced currents in homogenous and stratified conditions; and 3) model-data comparisons for a hindcast simulation in September-November 2005. The FVCOM was driven by the external forcing of a) tidal elevation at the open boundary, b) surface wind field obtained from the local meteorological forecast model and c) the surface heat flux constructed from the NCEP reanalysis data. The drift data used for the model-data comparison were the trajectory data of drifters deployed in fall of 2005. A monthly climatology of the water temperature and salinity fields was built by combining historical hydrographic data available in Cook Inlet and adjacent regions. The model results show that the Lagrangian velocity of near-surface drifters were guided dominantly by the tidal motion modulated with wind and heat fluxing, whereas the trajectory of surface drifters were very sensitive to front-featured background stratification and temporal/spatial variation of the surface wind stress. This study suggests that in order to simulate drifter trajectories, an effort needs to be made on improving the accuracy of the local meteorological model and on the long-term assimilation of the hydrographic field in Cook Inlet. It can be achieved by a long-term assimilation experiment with the satellite-derived SST and river discharges.

Executive Summary

Two major tasks have been completed: 1) simulating the climatic T-S driven circulation with and without river runoff and 2) conducting a set of wind-driven events for 1-2 months and comparing model results with observed buoy drifters. In addition to the required tasks, we a) constructed the monthly climatology of the water temperature and salinity fields, b) validated the local meteorological model, c) conducted a set of numerical experiments with tidal forcing only, tides plus wind forcing, tides plus wind forcing and surface heat flux. This project produces two databases: 1) a monthly hydrographic climatology and 2) model outputs of water currents, temperatures/salinity, Lagrangian drifter tracking data and program under a set of different initial condition and external forcing.

Objectives

The project examined 1) the seasonal variation of tide- and buoyancy (river discharge)-driven circulation in Cook Inlet and 2) impact of the temporal and spatial variability of the surface wind stress on the material transport process under homogeneous and stratified conditions. The objective of this study is to identify and qualify the relative importance of tidal oscillation, wind forcing and buoyancy fluxes (surface heating/cooling and river discharge) to dynamics and kinematics in Cook Inlet.

Methodology

Different coastal processes have inherent time and space scales that must be considered when determining the selection of model discretization and required grid resolution for accurate simulation of realistic dynamics. In Cook Inlet, the physical processes are characterized by strong tidal motion, buoyancy-induced density fronts and variable surface wind stress. An appropriate model system for this inlet requires (1) grid flexibility to resolve complex coastline and bathymetry, (2) accurate numerical methods that conserve mass, momentum, heat and salt, (3) proper parameterization of vertical and horizontal mixing; (4) modular design to facilitate selection of the essential model components needed in scientific or management applications and (5) the ability to use a wide variety of input data, especially as real-time atmospheric and coastal ocean measurements are becoming increasingly available for assimilation. This model should be robust, have a flexible user interface, and be an “open” community model, supported by an expanding base of users that continue to use and improve it.

We have made significant effort towards developing a model system that meets the above requirements and can be readily applied to Cook Inlet. A Cook Inlet model was developed by configuring an unstructured grid Finite-Volume Coastal Ocean Model (FVCOM) for realistic geometry of the inlet (Figure 2.1). The computational domain covers the entire inlet area with open boundaries over the continental shelf. Horizontal resolution varies from ~126 m near the coast and in rivers to ~13 km over the shelf close to the open boundary. Eleven uniform sigma levels are specified in the vertical, which respond to a vertical resolution of < 2.5 m near the coast and about 30 m in the deepest region of ~300 m.

This model was driven by tidal forcing at open boundaries, buoyancy input from river runoff, variable surface wind stress, and surface heat flux plus shortwave isolation. The model was first driven by tidal forcing consisted of five major constituents (three semi-diurnal: M_2; S_2; N_2 and two diurnal: O_1; K_1) at open boundaries and run continuously for 50 days. Then a least-squared harmonic analysis method was used to compute amplitudes and phases of tidal elevations at triangle nodes and tidal current ellipse parameters at triangle centers. The model-predicted tidal elevations were directly compared with the observations at tidal gauges. A well-calibrated tidal model database was established based on the model-predicted tidal constants for both the tidal elevation and currents. Foremen's harmonic analysis program was implemented into the model, which allows us to run the Cook Inlet FVCOM for the real-time (the true o'clock time) of selected months and years.

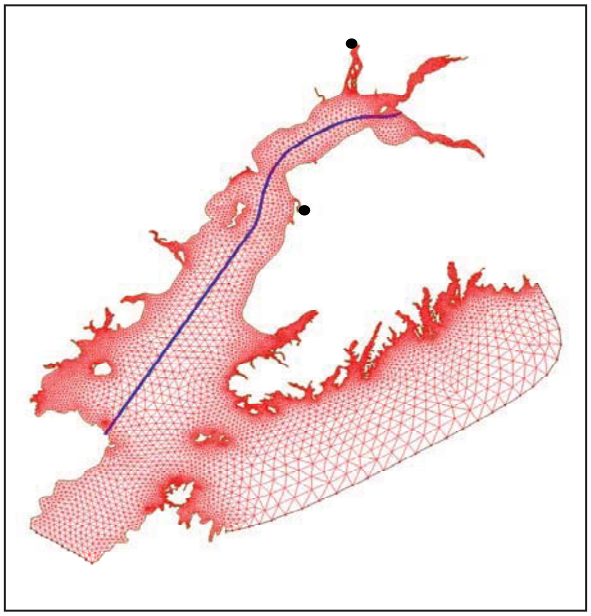

Figure 2.1. Unstructured triangular grid of the Cook Inlet FVCOM. Horizontal resolutions vary from 126 m near the coast and in rivers to 13 km over the shelf close to the open boundary. Dots: river runoff sites. Blue line: an along-inlet transect.

The year 2005 was selected to examine the temporal and spatial variation of tide-, river discharge-, wind- and heat flux-induced circulation in Cook Inlet and their impacts on the water transport. The model was first spun up for 17 days from August 15 to August 31, during which only tidal forcing was included. Monthly averaged climatologic hydrographic [temperature (T) and salinity (S)] fields, river discharge, surface wind stress and surface heat flux were then added, respectively for additional time integration from September 1 to November 30. A total of four experiments were made:

Case 1: Tides only: the model was driven only by five major tidal constituents (where T and S are constant everywhere);

Case 2: Tides + T/S + river discharge: the tidal forcing is the same as Case I. The August monthly averaged T/S and river discharge from two rivers were added on September 1 and then continuously integrated from September 1 to November 30.

Case 3: Tides + T/S + river discharge + wind: the tidal forcing, T/S and river discharges were the same as Case 2. The model-forecast hourly surface winds were added into the model on September 1 together with T/S and river discharges. The model ran prognostically from September 1 to November 30.

Case 4: Tide + T/S + river discharge + wind + surface heat flux: the model setup was the same as Case 3 except for including the surface heat flux.

The river discharge data were downloaded from the USGS website, which covered a period from 1948 to 1988. Five sites were selected (see Figure 2.1): two for the Kenai River and three for the Sustina River. Daily averaging was made on all the stream flow records available on these five stations, and results are shown in Figure 2.2. Because the stream flow measurements were made in different river branches, we add the data together to construct the river runoff values used for two rivers in the model. Although the river discharge varied significantly river from river, their seasonal patterns were very similar. The climatologic averaged data should represent the general feature of the river discharge in this region. The surface winds were prepared by Dr. Proshutinsky. The data were the 48 hour forecast wind fields that were downloaded from the Alaska Experimental Forecast Facility website. To reduce the forecast error, we only used the first 24 hour forecast data. A comparison of the predicted wind with the observation on buoys was made to validate the accuracy of the wind field predicted by RAMS.

No surface heat flux was provided in the RAMS. The surface heat flux used in our experiments was constructed from the NCEP reanalysis data with a 6-hour time interval. This data meets our needs for process studies with understanding that it might not be accurate enough for the real-time simulation.

A Lagrangian particle tracking experiment was made to examine the impact of the temporal and spatial variations of tidal currents, buoyancy- and wind-induced circulation on the water movement and thus the water transport in Cook Inlet. The experiment was made for four cases listed above during the periods where the near-surface drifters were deployed. By comparing with the observed drifter trajectory, we found that the water movement in Cook Inlet was driven by a complex physical process by both tides and winds. The model was robust enough to reproduce the water movement driven by tides, but not by winds. Although the tidal motion dominated the Lagrangian velocity of a particle, a particle trajectory was very sensitive to the wind perturbation, particularly in the density frontal zone. An effort must be made to improve the wind prediction in this region, because the wind field predicted by RAMs showed a significant bias from the observation on meteorological buoys. A brief description of our findings is summarized below.

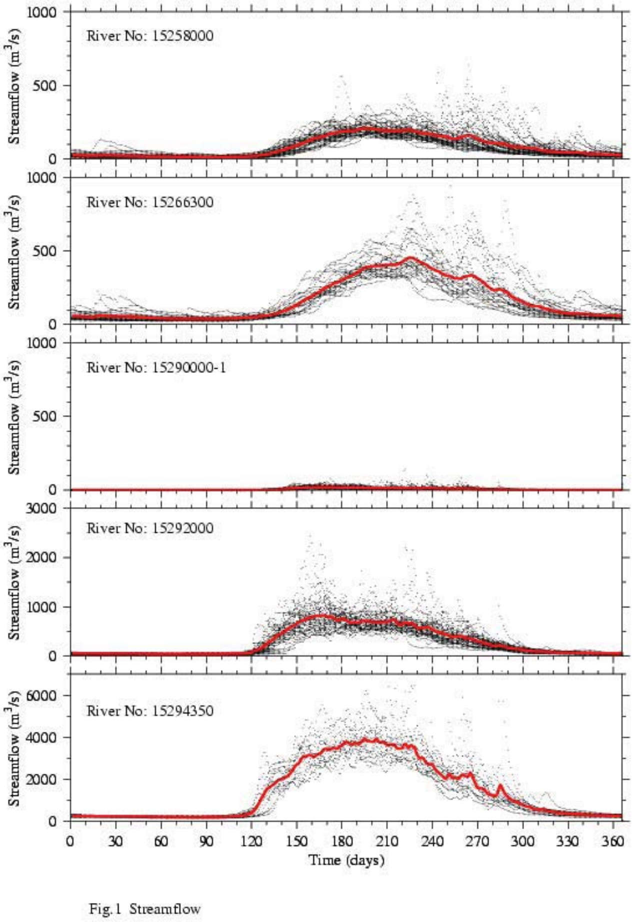

Figure. 2.2. Daily averaged river discharge rate at the Kenai River at Cooper Landing, AK (15258000) and Soldotna, AK (15266300), and the Susitna River at Palmer, AK (15290000), Gold Creek, AK (15292000), and Susitna station, AK (15294350). Red line: averaged; black lines: individual years. The data used for averaging cover a period from 1948 to 1988.

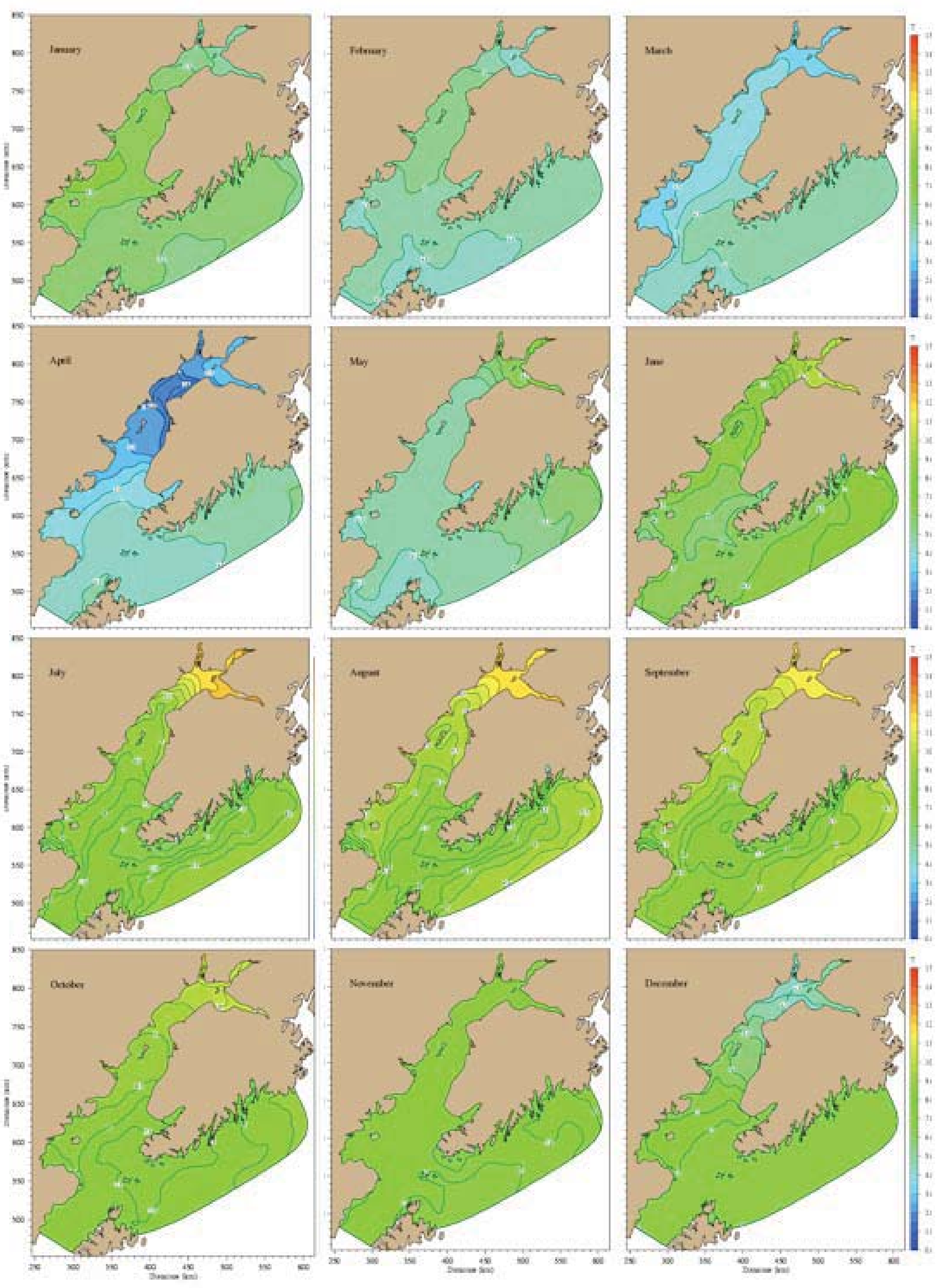

Figure 2.3. Distributions of the monthly averaged near-surface water temperature in Cook Inlet.

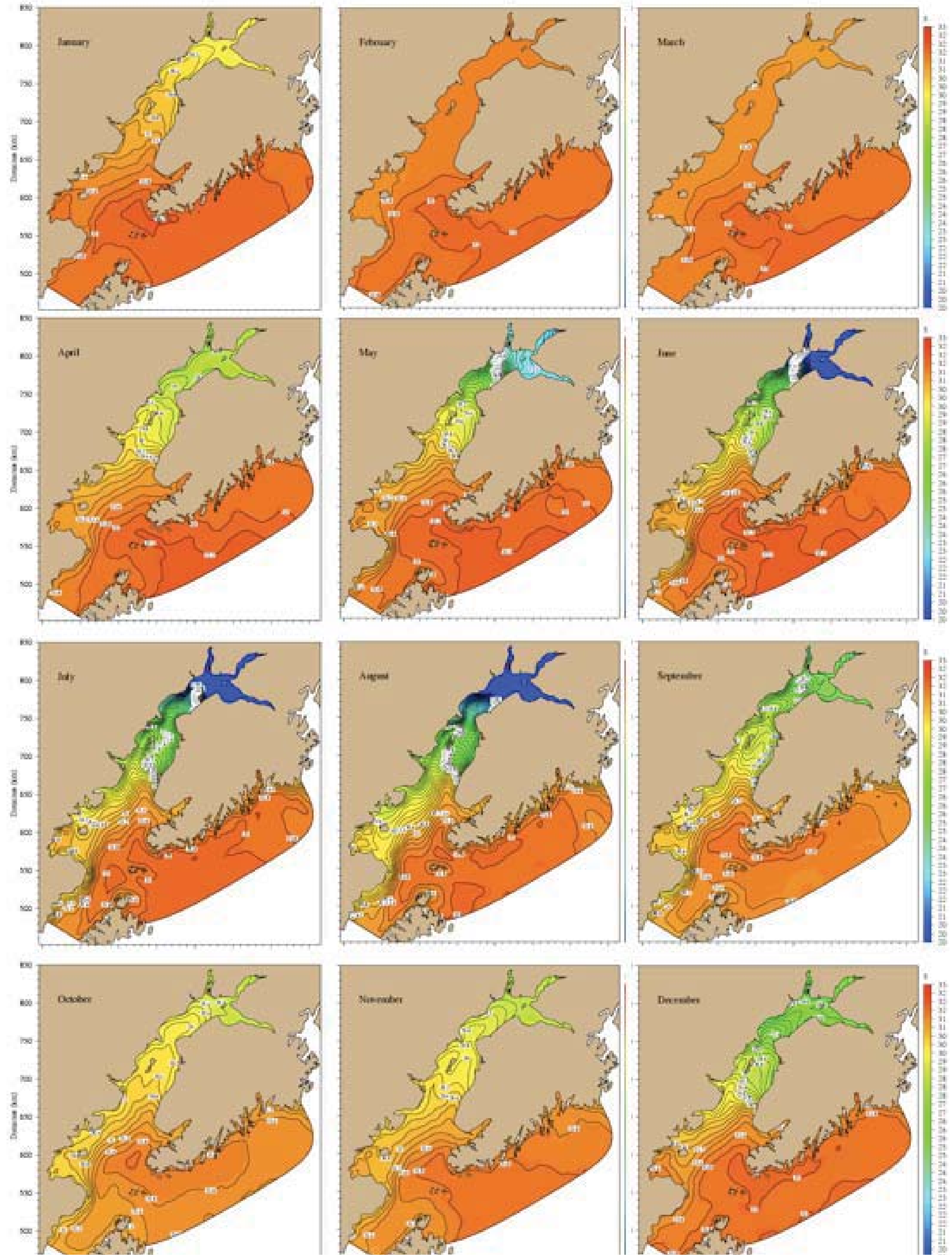

Figure 2.4. Distributions of the monthly averaged near-surface water salinity in Cook Inlet.

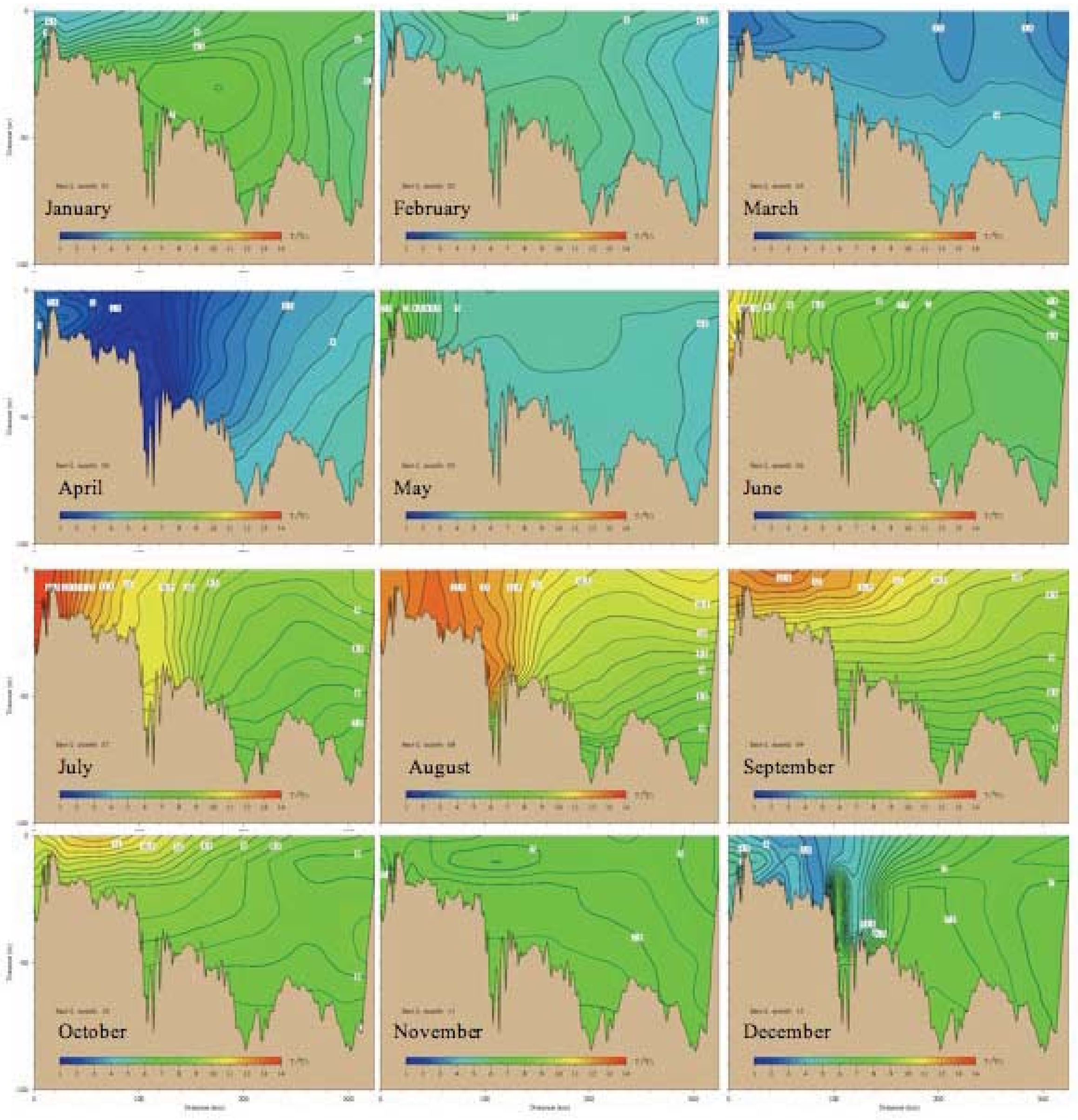

Figure 2.5. Distributions of the monthly climatologic water temperature on an along-inlet transect shown in Figure 2.1.

Accomplishments

Monthly climatologic temperature and salinity fields

One of the critical issues in simulating the circulation in Cook Inlet is the lack of initial conditions for water temperature and salinity. The hydrographic field in this region is characterized by strong density fronts that vary significantly with season and in space. We have collected hydrographic data available from various sources including the National Ocean Data Center (NODC) and World Ocean Atlas (WOA). The NODC data covers a time period from 1949 to 1999 and WOA is a high-resolution (0.25 degrees) temperature and salinity database (version 2) from the World's Oceans Analysis. The raw temperature or salinity records at every measurement site from

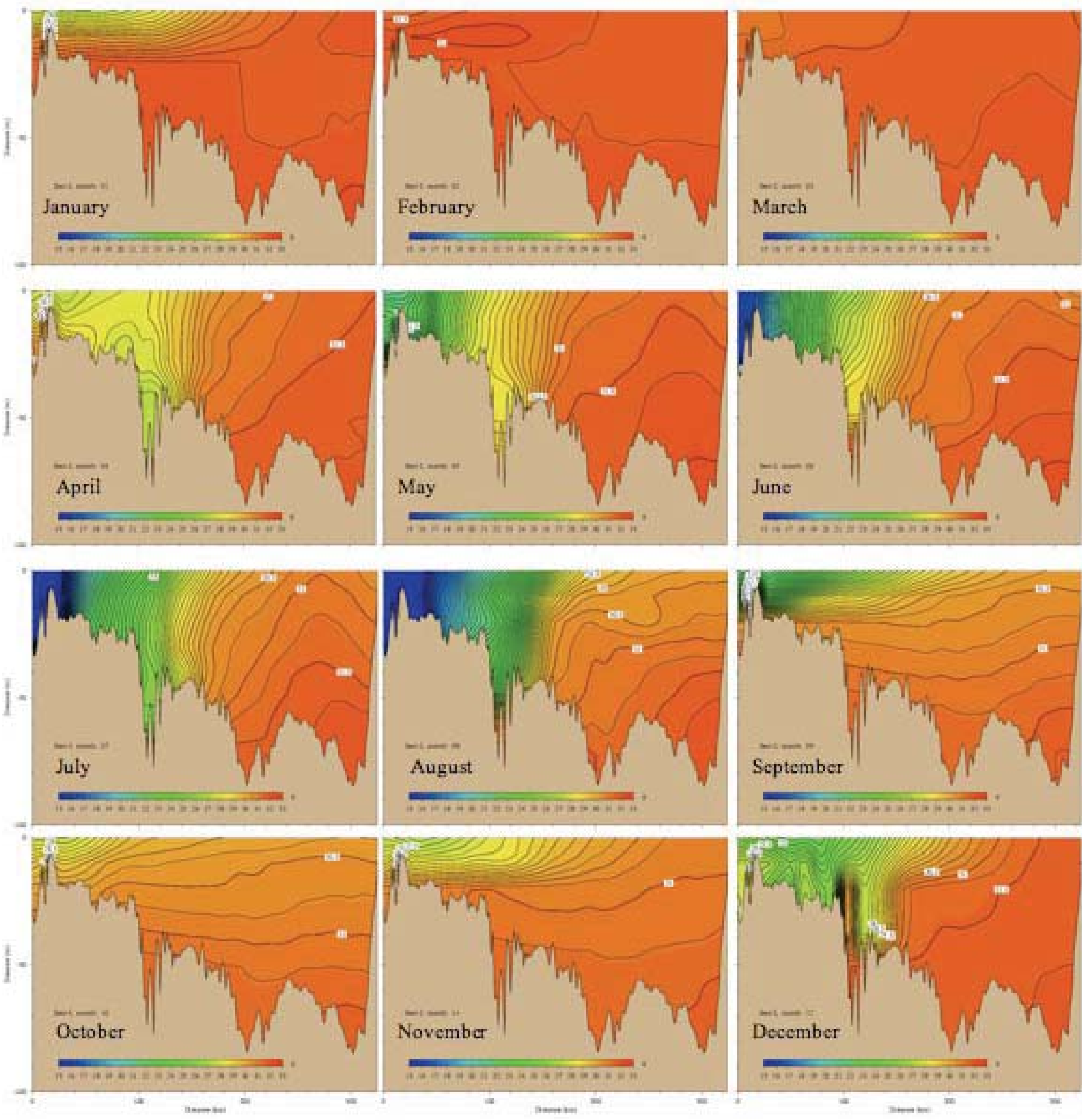

Figure 2.6. Distributions of the monthly climatologic water salinity on an along-inlet transect shown in Figure 2.1.

NODC was first calibrated by quality controls and then they combined with gridded WOA records to construct the monthly climatologic fields of the water temperature and salinity covering the entire computational domain of the Cook Inlet FVCOM. All monthly climatologic temperature and salinity profiles are built with the same format at 16 standard depth levels: 0, 10, 20, 30, 40, 50, 60, 75, 100, 125, 150, 175, 200, 225, 250 and 299 m.

Examples for the horizontal distributions of the surface water temperature and salinity in the computational domain were shown in Figures 2.3 and 2.4. A vertical section cut along the inlet was also selected to show the seasonal variability of the vertical stratification in Cook Inlet and results were shown in Figures 2.5 and 2.6.

It should be pointed out that in February and March there were a very few measurement sites available, so that the reliability of monthly climatologic T and S for these two months were relatively low. Caution should be paid when these data are used.

The monthly climatology of the water temperature and salinity clearly show that the water in Cook Inlet is strongly stratified in summer through fall. The water is less saline and cold in the upper region and saline and warm in the lower region. Since the contribution of water temperature and salinity to water density is always opposite each other in this region, the density gradient is much weaker than what was observed in either water temperature or salinity. Therefore, even though both water temperature and salinity exhibit strong surface-bottom fronts in spring through summer and surface-intensified fronts in fall through early winter, the density front remains weak through the year.

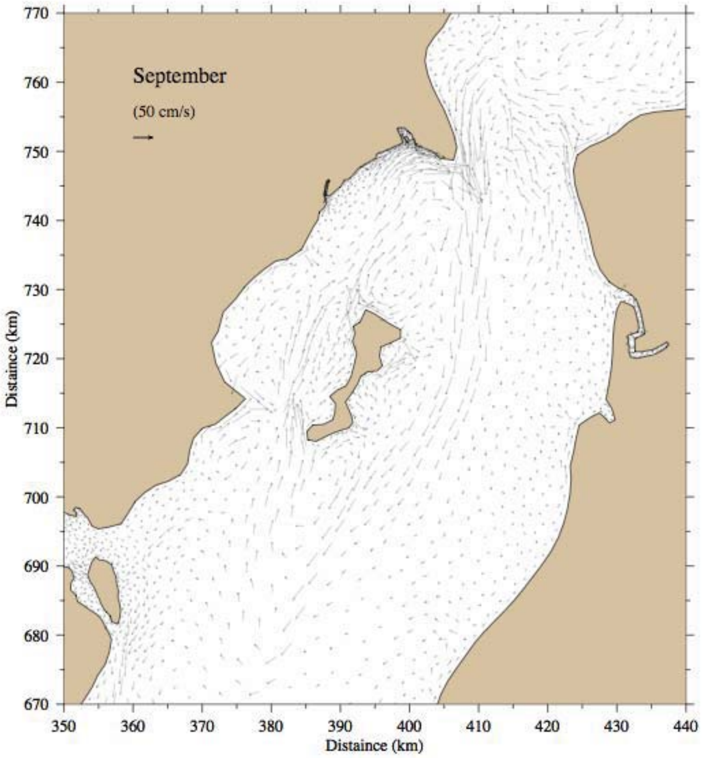

Figure 2.7. Distributions of the near-surface subtidal currents around Kalgin Island under the September monthly climatology field of the water temperature and salinity.

Monthly climatologic fields of subtidal currents

In our previous tidal experiments, we have shown that strong tidal motion characterizes Cook Inlet but the residual currents were driven dominantly by the nonlinear interaction of tidal currents over irregular bathymetry and coastal geometry. Although a strong seasonal variation was detected in the monthly climatology of the water temperature and salinity, the residual currents remained less changed throughout the year as a result of the thermal and salt cancellation in the density field in the inlet. This has been proven in our numerical experiments with the monthly climatology of the water temperature and salinity.

Initialized with the monthly climatology of the water temperature and salinity and driven by the tidal forcing, we ran the model to construct the monthly climatologic field of the subtidal current in Cook Inlet. In each experiment, the model ran for 50 days for each month with a 10 days' spin up. Subtidal currents were defined as the mean flow over the 40 days after tidal motion is filtered using the harmonic analysis. Monthly climatology fields of subtidal currents were constructed.

Without inclusion of wind forcing and surface heat flux as well as river discharges, the model-predicted monthly subtidal currents remain very similar throughout the year. Significant subtidal currents occur around the headland and islands, which result from the asymmetric tidal flushing around curved shape coastal geometry. For example, the field of September monthly averaged subtidal currents around Kalgin Island in the upper region of Cook Inlet is shown in Figure 2.7. Tidal flushing around the headland in the upper stream area north of Kalgin Island generates double cyclonic (northern side) and anti-cyclonic (southern side) eddies at the tip of the headland. These two eddies produce relatively strong southward subtidal currents flowing on the eastern side of the island and then return to north around the island. An anti-cyclonic eddy exists on the northern side of the island, forming a very complex current field in that region.

This current pattern remains unchanged throughout the year. The existence of multiple residual eddies makes the water exchange process in that area very complex. Driven by a periodic tidal motion, the Lagrangian particle movements can become chaotic. This means that the drifter trajectories deployed in that region are very sensitive to any external perturbation, and they might behave chaotically when they enter the "saddle" area between eddies. That was observed in our Lagrangian particle experiments described below.

Particle-tracking experiments

A Lagrangian particle tracking experiment was made to investigate the impact of tidal, buoyancy- and wind-driven motions on the water movement in Cook Inlet. The model was spun up under the realistic tidal forcing for 17 days from August 15 to August 31, 2005, and then ran under various forcing conditions with 1) only tidal forcing, 2) tides + August monthly T/S climatologic fields; 3) tides + August T/S climatologic fields + winds and 4) tides + August T/S climatologic fields + surface heat flux, respectively from September 1 to November 30, 2005. The model results for these four different cases were output at hourly time interval. The particle tracking experiment was carried out by using 3-D "offline" Lagrangian tracking program to trace particles in the offshore model databases. The particles were released at the same locations where the near-surface drifters were deployed in September and October, 2005, and a comparison between model-predicted and observed trajectories and Lagrangian velocities were made for all available drifters during that period.

The model-data comparisons were made for all available drifter trajectories and examples are given here. Figures 2.8 - 2.11 show the comparison between observed and model-predicted trajectories for drifter #36190 for four different periods from 11:00 September 8 to 01:00 September 21; from 05:00 September 21 to 14:00 October 9; from 20:00 October 9 to 19:00 October 26 and from 10:00 October 31 to 17:00 November 7, 2006, respectively. The model particle was released at the same location as drifter #36190 and traced at a fix depth of 4 m below the surface.

For the first deployment period, in the homogeneous case with the only tidal forcing, the model-predicted particle trajectory followed a general path of the observed drifter trajectory but showed a significant disparity a few days after it was released. Although the model failed to reproduce accurately the drifter's path, the Lagrangian velocity predicted by the model matched well with the observation. This suggests that the tidal motion was the dominant process to control the water movement in Cook Inlet. Since the model was very accurate in tidal simulation, it implies that the disparity found between model-predicted and observed trajectories of that drifter was probably due to the fluctuation of water stratification, winds and surface heat flux.

No hydrographic survey data were available during the drifter deployment period. There were the wind fields produced by the Alaska regional weather forecast system (RAMS) but those data were not accurate (see the discussion later). No surface heat flux was provided by RAMS, and only available heat flux data were NCEP reanalysis data that were sampled at a time interval of 6 hours and at a horizontal resolution of 0.5 degree, which were too coarse to resolve the local temporal and spatial variability of the surface heat flux. Due to the lack of the realistic T/S field for the initial condition of the model and inaccurate wind and surface heat flux, we did not expect that the model could accurately reproduce the observed trajectory of the drifter. Instead of it, we traced the particle under the condition with the August monthly T/S climatology, forecast winds and NCEP heat flux, respectively to examine how sensitive the model-predicted particle trajectory to these forcing conditions.

The model did show that the movement of the particle was sensitive to the water stratification. In the case with addition of the August T/S climatology field, the particle only followed the observed drifter in the first tidal cycle and then moved around the island. A small perturbation in the Lagrangian velocity caused the particle to significantly shift away from observations. Adding the wind forcing enhanced the fluctuation in the north-south direction, which improved the simulation in the first few days and caused a much larger bias in the later days. Inputting the surface heat flux also made the particle trajectory significantly different from those predicted by the only tidal forcing, tides plus T/S and tides plus T/S and winds.

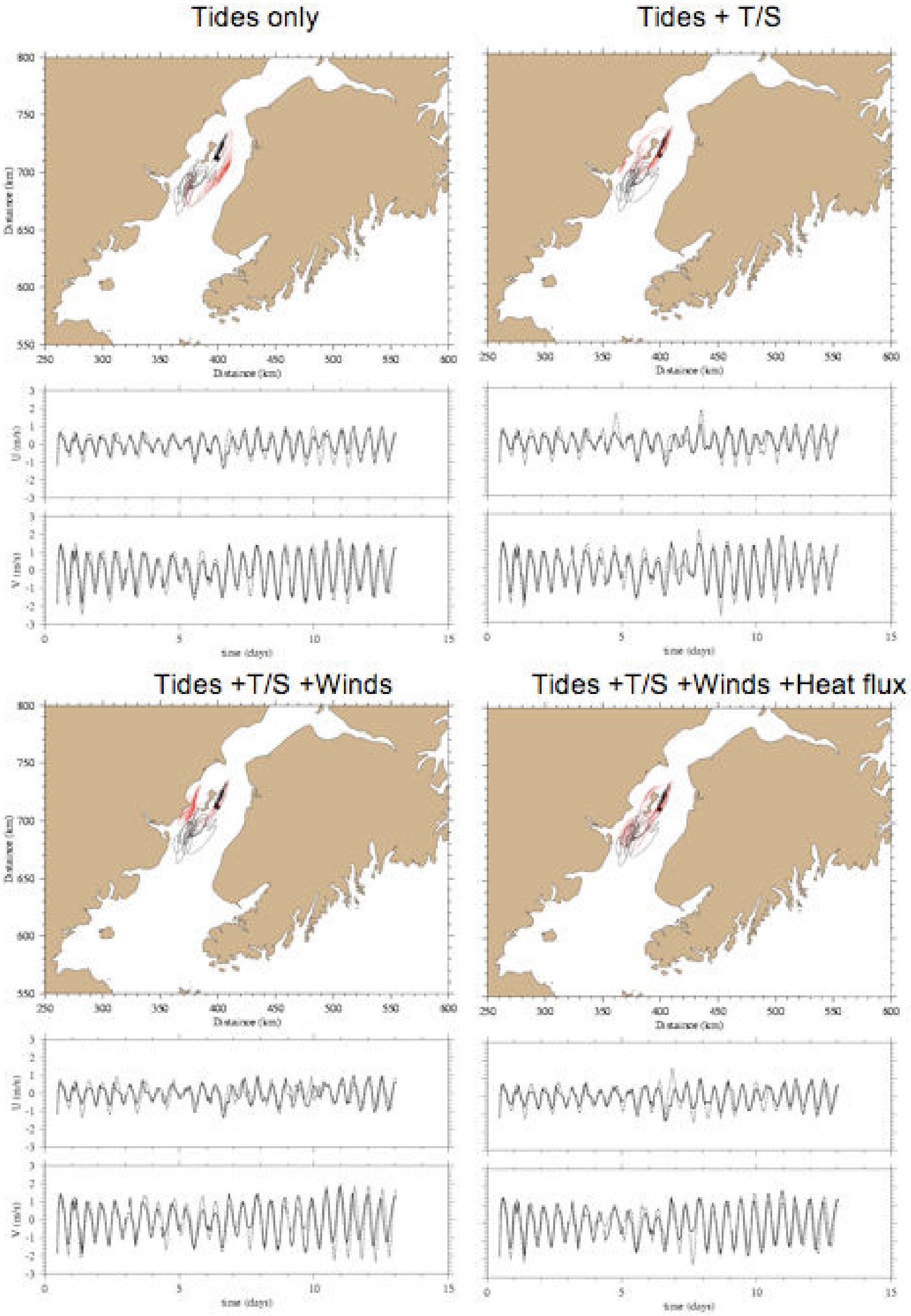

Figure 2.8. Comparison between model-predicted and observed trajectories and Lagrangian velocities of drifter # 36190a for a time period from 11 o'clock September 8 to 01 o'clock September 21, 2005. The model particles were released at a depth of 4 m below the surface. Red: model-predicted; black: observed.

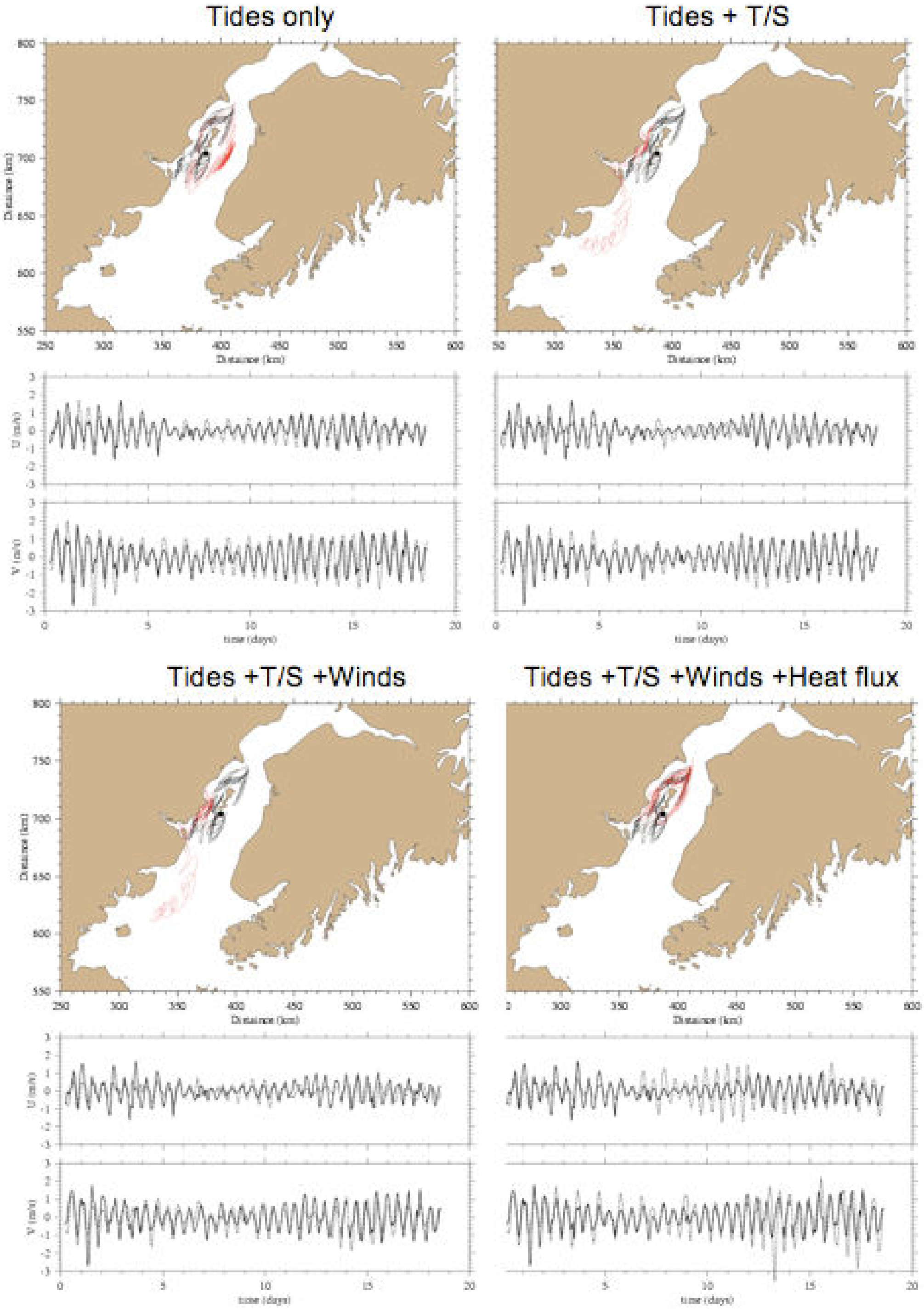

Figure 2.9. Comparison between model-predicted and observed trajectories and Lagrangian velocities of drifter # 36190b for a time period from 05 o'clock September 21 to 14 o'clock October 9, 2005. The model particles were released at a depth of 4 m below the surface. Red: model-predicted; black: observed.

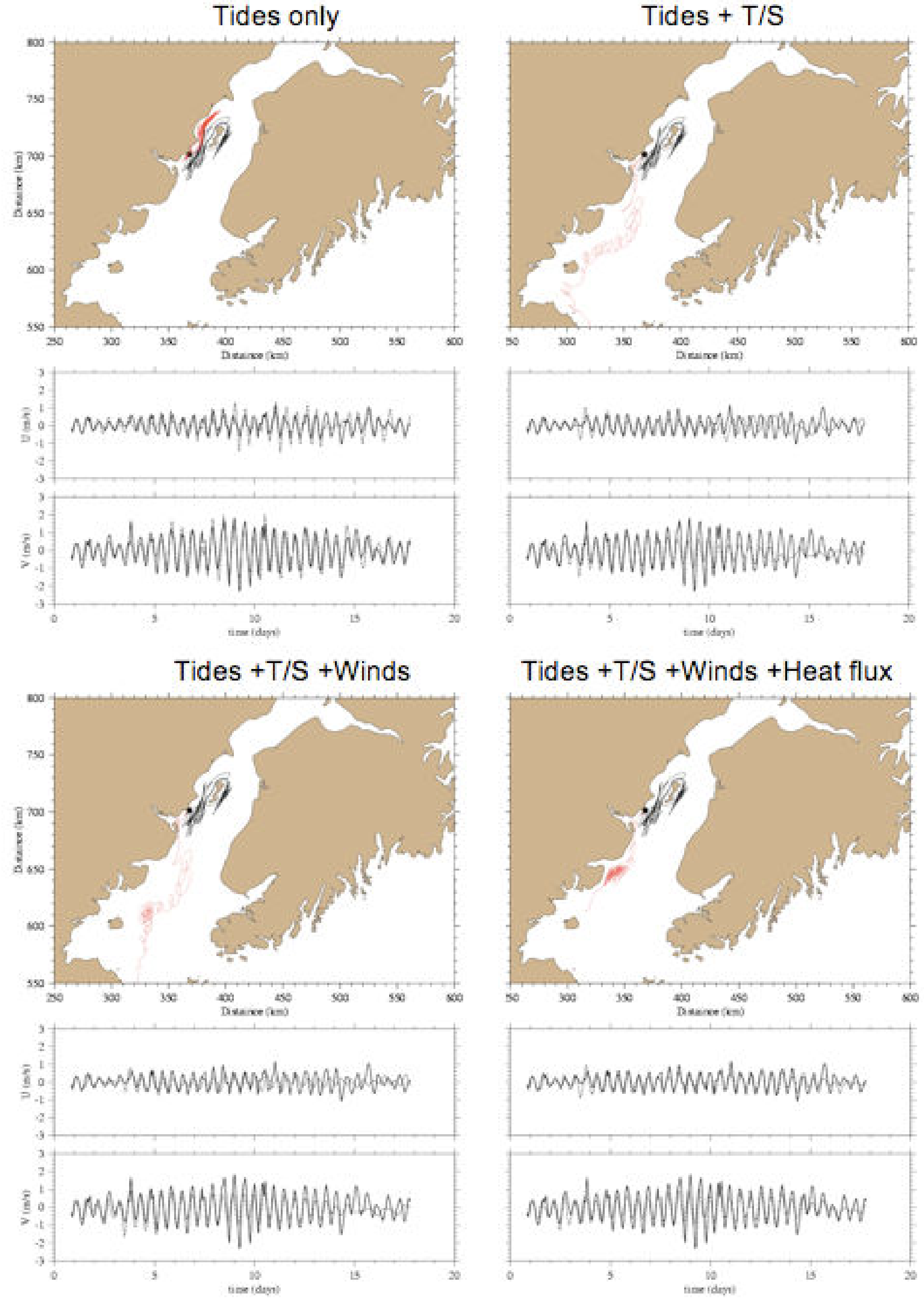

Figure 2.10. Comparison between model-predicted and observed trajectories and Lagrangian velocities of drifter # 36190c for a time period from 20 o'clock October 09 to 19 o'clock October 26, 2005. The model particles were released at a depth of 4 m below the surface. Red: model-predicted; black: observed.

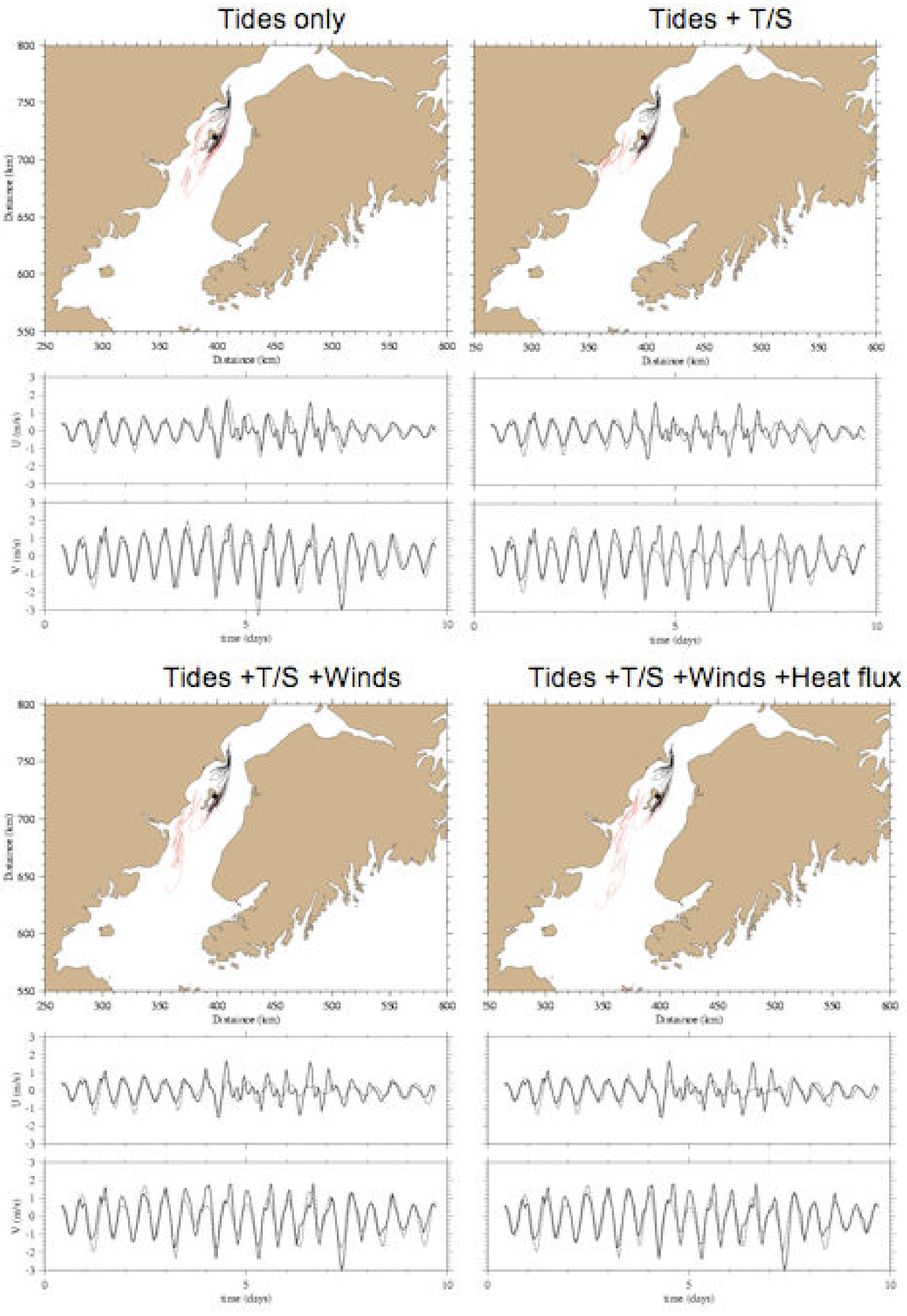

Figure 2.11. Comparison between model-predicted and observed trajectories and Lagrangian velocities of drifter # 36190d for a time period from 10 o'clock October 31 to 17 o'clock November 9, 2005. The model particles were released at a depth of 4 m below the surface. Red: model-predicted; black: observed.

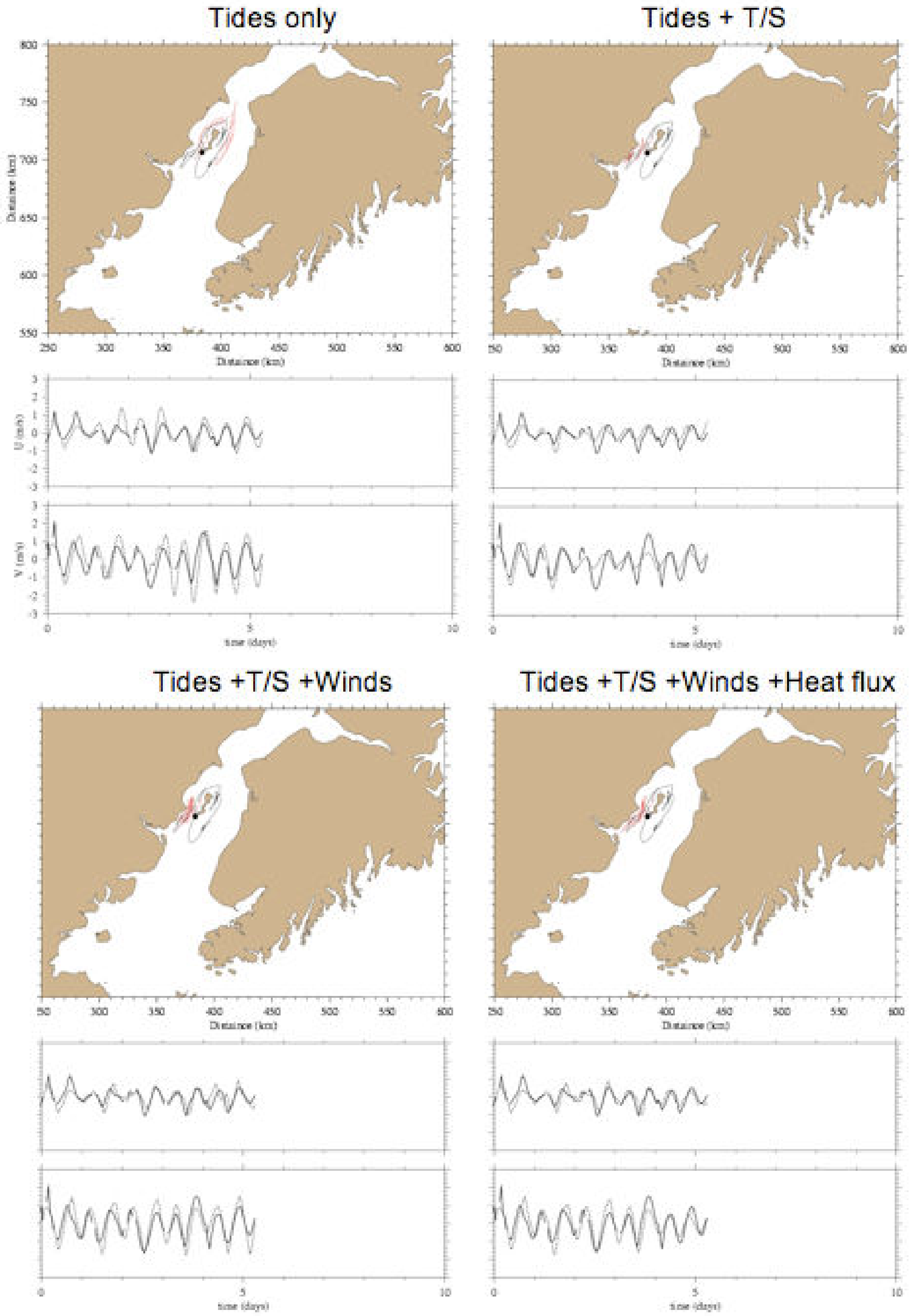
Tides only

Tides + T/S

Tides +T/S +Winds

Tides +T/S +Winds +Heat flux

Figure 2.12. Comparison between model-predicted and observed trajectories and Lagrangian velocities of drifter # 36193a for a time period from 23 o'clock September 10 to 07 o'clock September 16, 2005. The model particles were released at a depth of 4 m below the surface. Red: model-predicted; black: observed.

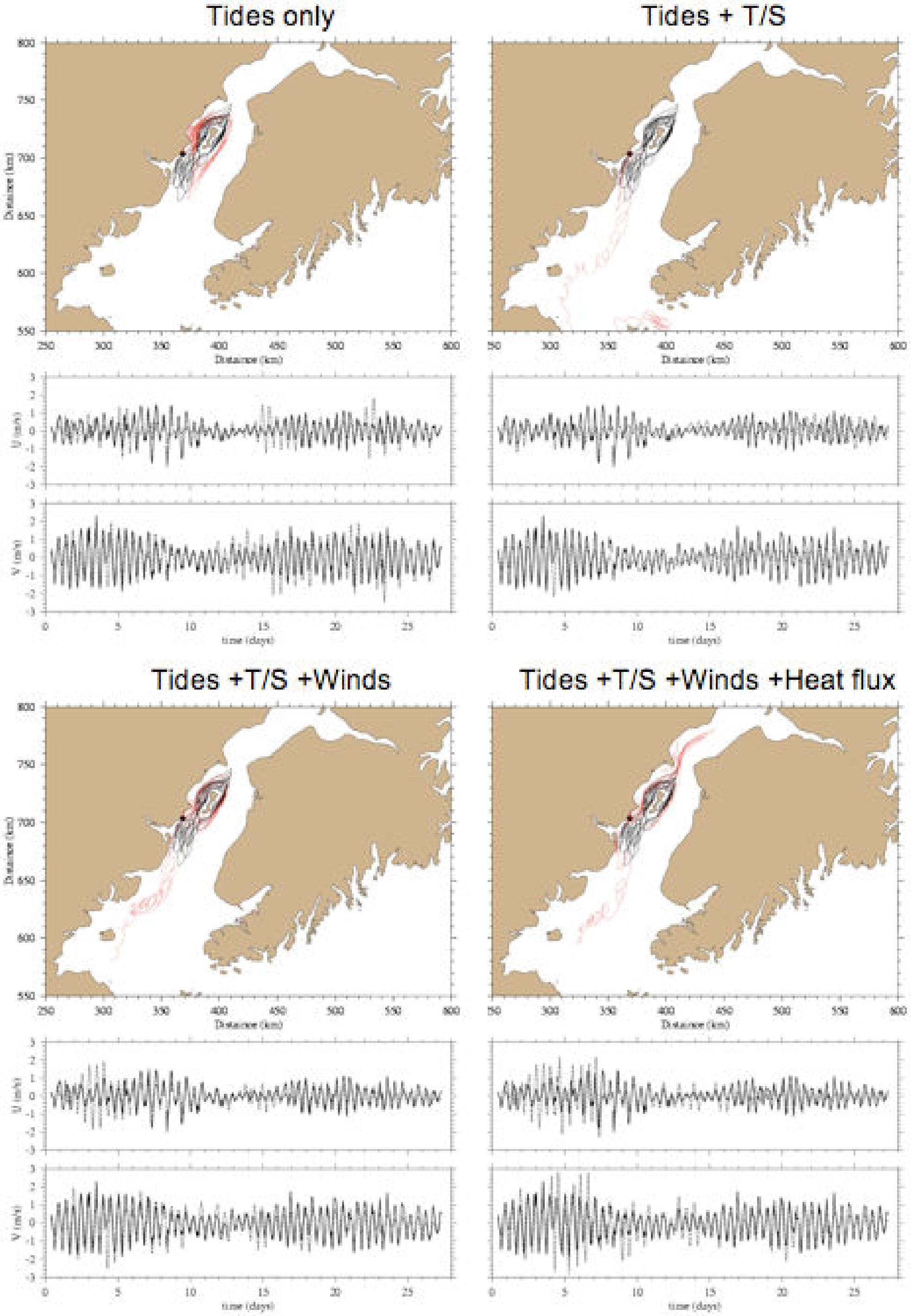

Figure 2.13. Comparison between model-predicted and observed trajectories and Lagrangian velocities of drifter # 36193b for a time period from 09 o'clock September 16 to 07 o'clock October 13, 2005. The model particles were released at a depth of 4 m below the surface. Red: model-predicted; black: observed.

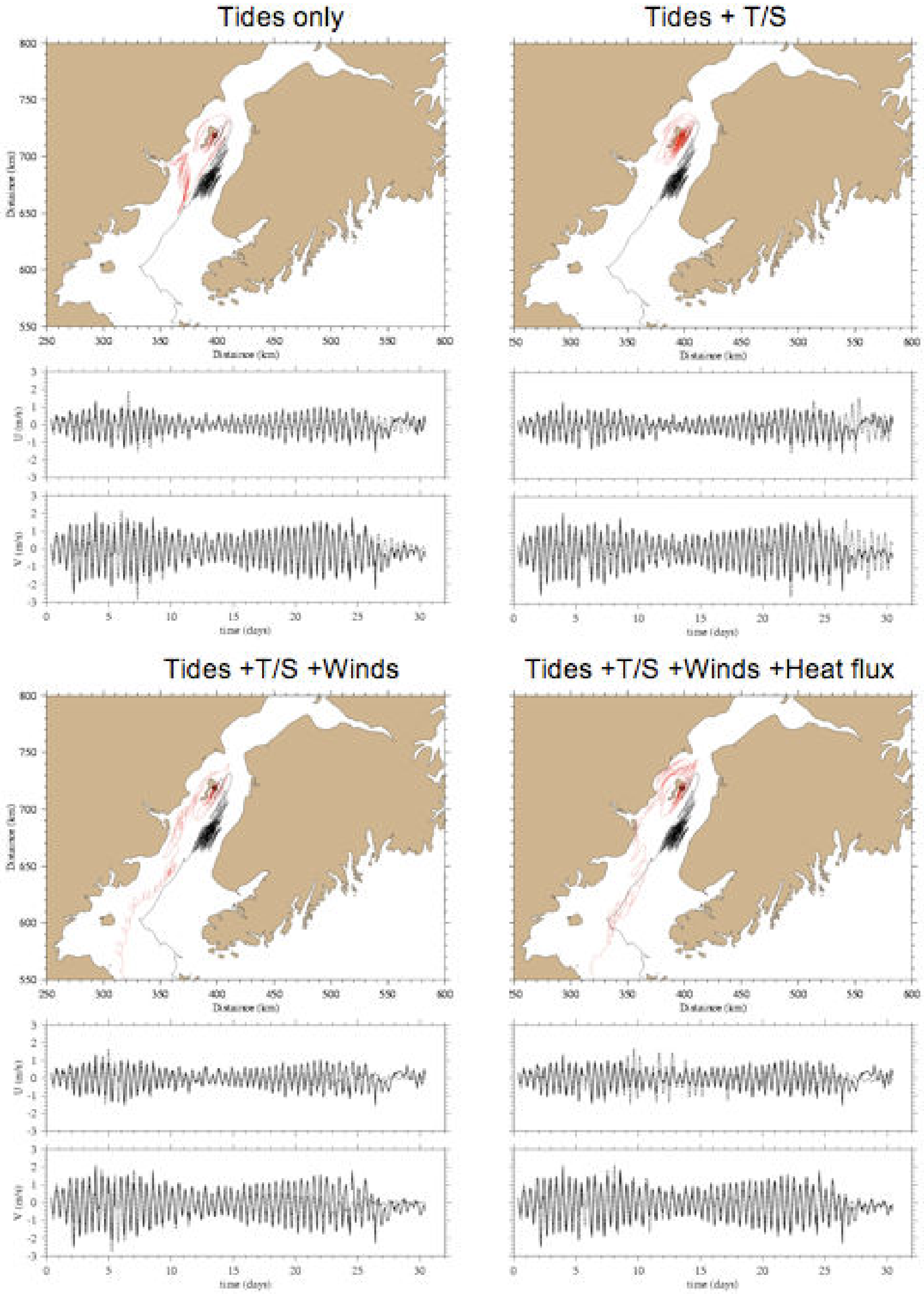

Figure 2.14. Comparison between model-predicted and observed trajectories and Lagrangian velocities of drifter # 36193c for a time period from 09 o'clock October 13 to 10 o'clock November 12, 2005. The model particles were released at a depth of 4 m below the surface. Red: model-predicted; black: observed.

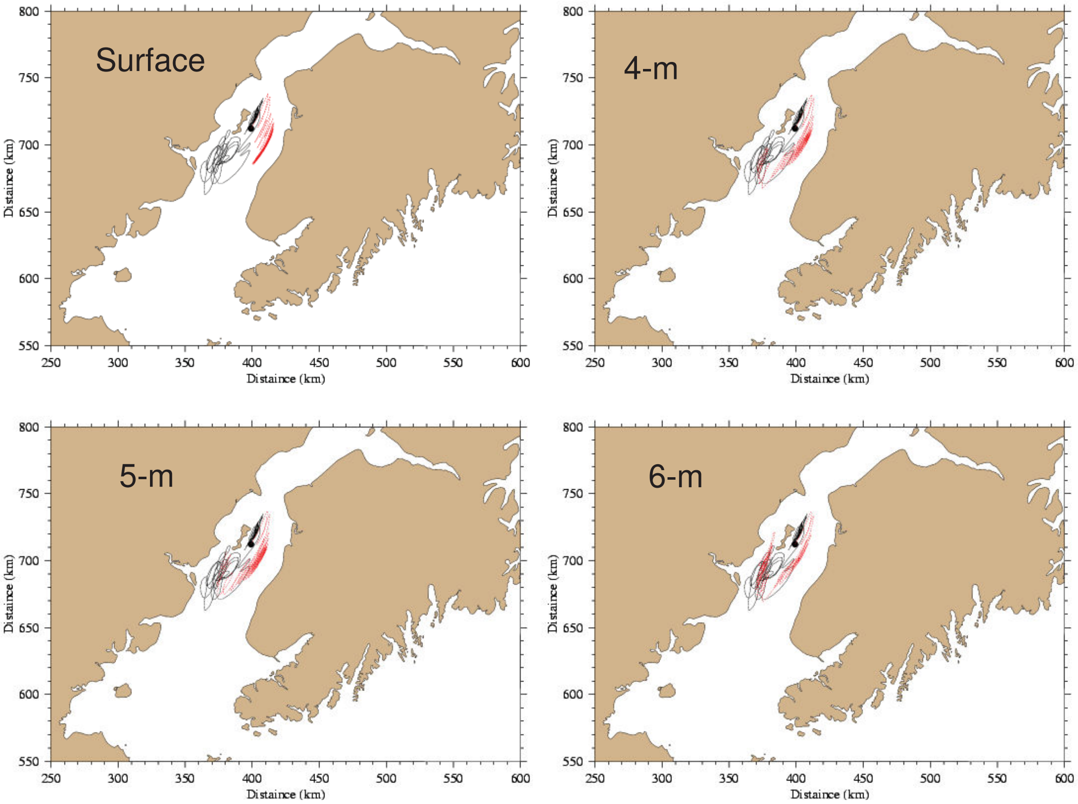

Figure 2.15. Comparison between model-predicted and observed trajectories of particles (#36190a) released at surface, 4-m, 5-m and 6-m respectively for a time period from 11 o'clock September 8 to 01 o'clock September 21, 2005. Red: model-predicted; black: observed. This is the case with the only tidal forcing.

Similar results were found in the 2nd, 3rd, and 4th deployments. In the 2nd deployment, adding the T/S caused the particle to move far south. The winds during that period did not efficiently reduce the southward movement of that particle. Inputting the surface heat stopped the southward drifting but it caused the particle northward movement that was significantly biased from the observation. The same features were observed in 3rd and 4th deployments.

Figures 2.12 – 2.14 show the comparison between observed and model-predicted trajectories for drifter #36193 for three different periods from 23:00 September 10 to 07:00 September 16; from 09:00 September 16 to 07:00 October 13; from 09:00 October 13 to 10:00 November 12, 2006, respectively. The model particle was released at the same location as drifter #36193 and traced at a fixed depth of 4 m below the surface. The model-data comparison results for these three deployments were very similar to the drifter #36190. During the 3rd deployments, the observed drifter moved quickly southward and then left the inlet. This was a typical wind event during the spring tidal period, because it was not resolved in either the tidal only forcing case or tides plus T/S case (Figure 2.14). Adding the wind caused the particle to move southward as the observed drifter. The model-predicted trajectory tended to merge the observation after the surface heat flux was included. Since no strong wind was observed in early November 2005, it implies that the nonlinear interaction between wind and spring tidal currents seemed to drive the fast southward movement of the drifter during that period.

The model also showed that due to the large tidal range in the inlet the trajectory of a particle was also sensitive to the tracking depth. Examples were shown

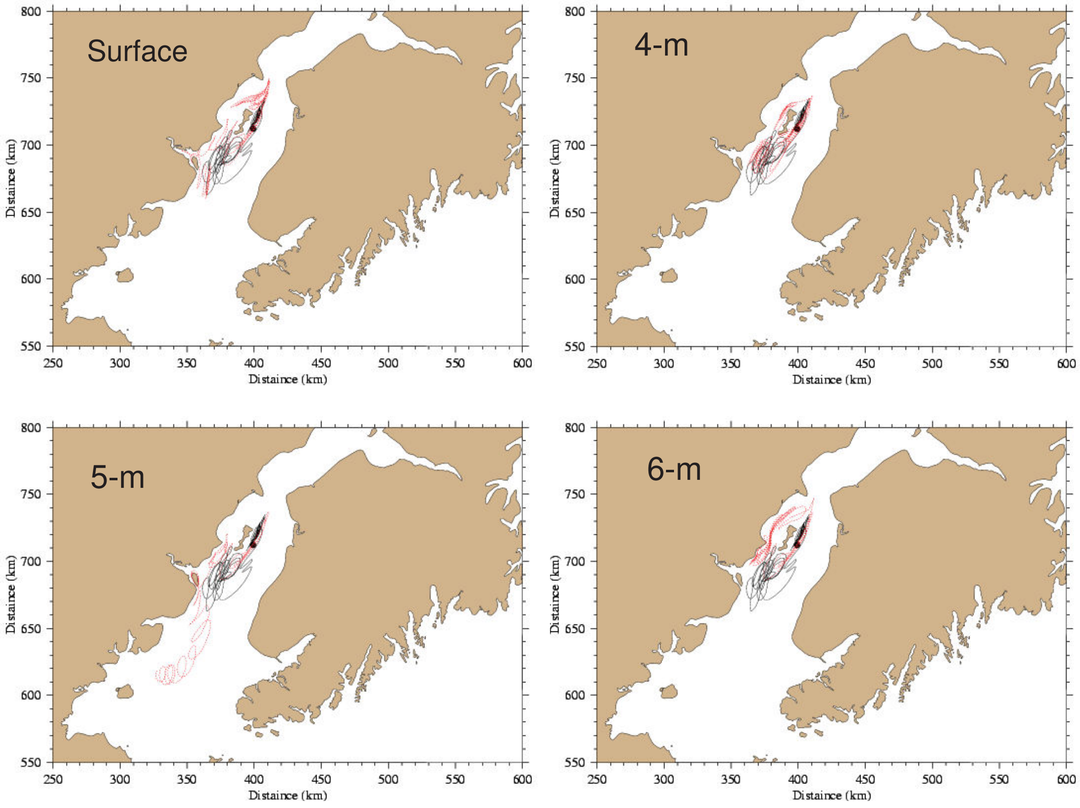

Figure 2.16. Comparison between model-predicted and observed trajectories of particles (#36190a) released at surface, 4-m, 5-m and 6-m respectively for a time period from 11:00 September 8 to 01:00 September 21, 2005. Red: model-predicted; black: observed. This is the case with tides+T/S+wind+heat flux.

in Figure 2.15 for the homogeneous case with the only tidal forcing. This figure showed that the trajectories of particles, which were released at the same location but at different water depths, moved in significantly different paths. The particle released at the surface stayed on the eastern side of the island all the time. Although the particles released at 4 m, 5 m and 6 m below the surface had similar paths, their trajectories considerably differed from each other.

In the case with inclusion of either T/S or wind or surface heat flux, the difference became much larger. An example was shown in Figure 2.16 for the same particle as that shown in Figure 2.15 but driven under the conditions with tides, T/S, winds and surface heat flux. This figure clearly showed different particle trajectories for particles released at surface, 4 m, 5 m and 6 m below the surface.

The particle released at 4 m had a close trajectory like the observed drifter, while the particle at 5 m moved quickly southward and left the area where the observed drifter stayed.

An additional example is shown in Figure 2.17 for a particle that was released as the same location of drifter #36193 but at different depth. Particles released at surface, 4 m, 5 m and 6 m all eventually moved to the south as the observed drifter, but their trajectories significantly differed each other. The particle released at the surface first rotated around the island and then moved quickly southward, while the particle at 4 m showed similar paths in the first few tidal cycles as the surface particle and then moved southeastward to be

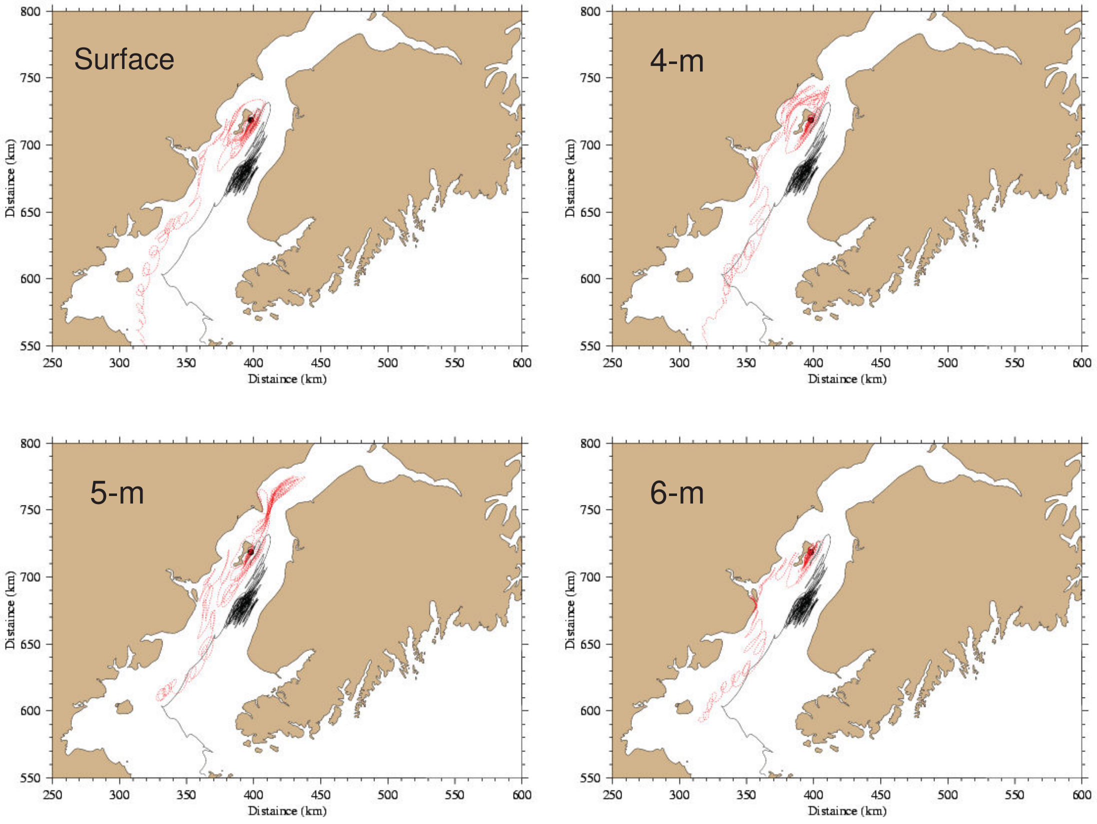

Figure 2.17. Comparison between model-predicted and observed trajectories of particles (#36193c) released at surface, 4-m, 5-m and 6-m respectively for a time period from 09:00 October 13 to 10:00 November 12, 2005. Red: model-predicted; black: observed. This is the case with tides+T/S+wind+heat flux.

close to the observed drifter. Particle at 5 m showed a significant northward shift first and then returned south to merge to the path of the observed drifter. Particle at 6 m first moved to the southern side of the island, drifted southward along the coast and then merged to the path of the observed drifter later.

These evidences suggest that in order to simulate accurately the trajectory of observed drifters, one must resolve the meso-scale temporal and spatial variability of the water stratification and mixing due to surface wind and heat fluctuation.

A simple statistical analysis was conducted to estimate the averaged absolute difference and standard deviation between model-predicted and observed Lagrangian velocities for drifters #36190 and #36193 experiments, and results were summarized in Table 2.1. The averaged model-data absolute difference for 4 deployments of drifter #36190 was 30 cm/s for u (east-west component) and 42 cm/s for v (north-south component) for the case with the only tidal force. This difference increased by about 2-3 cm/s when the T/S, winds, and surface heat flux were included. The standard deviation value was about 10 cm/s larger than the absolute difference values. Similar results were also shown for drifter #36193. This error is much smaller than the maximum value of tidal current velocity in the inlet but was in the same order of magnitude as wind- and buoyancy-driven subtidal currents, suggesting that it is critical to resolve accurately the subtidal currents in Cook Inlet in order to provide the realistic water transport process in this region.

Table 2.1. Averaged absolute differences and standard deviations between model-predicted and observed Lagrangian velocities. $|\Delta u|$ and $|\Delta v|$ are the x and y components of the averaged absolute difference and σ_u and σ_v are the standard deviation for u and v. Case 1: tides only; Case 2: tides plus T/S; Case 3: tides plus T/S and winds; Case 4: tides plus T/S, winds and surface heat flux.

	Drifter #36190				Drifter #36193			
	$|\Delta u|$ m/s	$|\Delta v|$ m/s	σ_u m/s	σ_v m/s	$|\Delta u|$ m/s	$|\Delta v|$ m/s	σ_u m/s	σ_v m/s
Case 1	0.30	0.42	0.38	0.54	0.33	0.42	0.43	0.55
Case 2	0.34	0.42	0.44	0.56	0.37	0.45	0.49	0.57
Case 3	0.34	0.42	0.44	0.54	0.33	0.43	0.42	0.55
Case 4	0.32	0.44	0.43	0.59	0.36	0.42	0.48	0.56

Comparison between the RAMS predicted and measured winds

We used the Alaska regional RAMS 48 hours forecast wind fields to drive our model in the Lagrangian particle tracking experiments. To ensure the reliability of the wind field, we selected only the first 24 hour forecast data. We questioned the accuracy of these wind data after the failure to improve the simulation results of the particle trajectories through comparisons with observed drifters. To investigate this problem, we made a direct comparison of the RAMS predicted wind velocity to the measurement winds at NDBC-C-MAN stations in Cook Inlet. Both predicted and measurement winds were converted to a height of 10 m above the sea level.

Figure 2.18 shows the locations of the meteorological buoy sites in Cook Inlet and adjacent regions. Two buoys were selected for this study. One is buoy labeled “NDFA2” which is located at the coast west of Kalgin Island and the other is buoy labeled “AUGA2” which is located near an island in the southern region of the inlet.

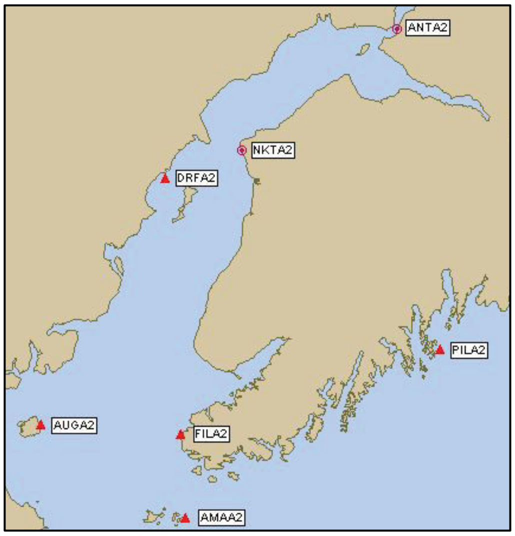

Figure 2.18. Locations of coastal meteorological measurement buoy sites around Cook Inlet. Red filled triangles indicate the NDBC C-MAN stations.

Figure 2.19 presents the comparison between the RAMS predicted and measurement wind velocities at a height of 10 m at NSFA2 and AUGA 2 for a time period during which our experiment was conducted. The results clearly show that RAMS failed to predict the relatively large wind event even for a short time period of 24 hours. In addition to the wind speed, the model also seemed to have trouble capturing the right direction during air-frontal passages. For example, in late September, the wind measurement shows a strong southward wind velocity of ~15 m/s at both NSFA2

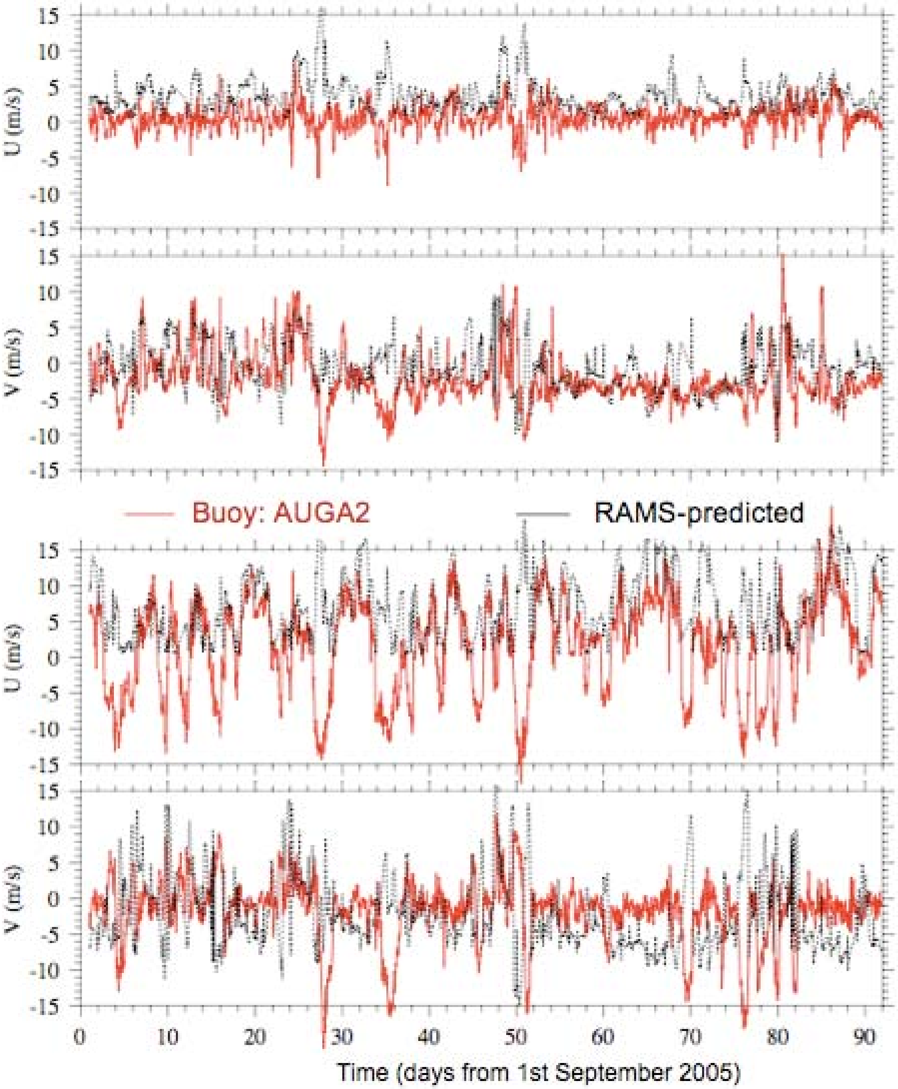

Figure 2.19. Comparison between the observed and Alaska RAMS forecast wind velocity at the10-m height above the sea surface.

and AUGA2, but RAMS predicted that the maximum wind velocity was directed eastward. The same evidence occurred in late October and November. In November, the phase of the model-predicted wind seemed to have a shift from the observed wind.

This comparison suggests that the Alaska regional RAMS needs to be improved in order to make it more useful to drive the ocean model. A better meso-scale meteorological model system with data assimilation should be developed to provide a reliable and accurate wind field in Cook Inlet for the hindcast application and also ocean model simulation. Our Lagrangian particle tracking experiment clearly shows that the buoyancy- and wind-driven circulations play a critical role for particle trajectories and water transport in Cook Inlet. Without improvement in the meteorological forcing fields, it is impossible to simulate accurately the trajectories of drifters deployed in this region.

Remarks and Suggestions

Our modeling experiments demonstrate that due to strong tidal flushing around headlands and islands the residual flow field in Cook Inlet is characterized with multiple eddy fields. Driven by strong periodic tidal motions, the particle movement might become chaotic in this system, especially in the upper region near Kalgin Island.

The Lagrangian particle tracking experiment clearly shows that the Lagrangian velocity is dominated by tidal motion, but the particle trajectories were sensitive to water stratification, wind fluctuation and temporal variation of the surface heat flux. In order to reproduce accurately the drifter trajectories, an effort must be made to improve the accuracy of the meteorological forcing in Cook Inlet.

According to our experience in this project, we suggest:

1) Creating an improved meso-scale meteorological weather hindcast system for both wind and surface heat flux fields through the assimilation with existing meteorological buoys and improved surface heat algorithms.

2) Deploying current meter moorings around Kalgin Island to measure both tidal and subtidal currents and then configure Cook Inlet FVCOM into a hindcast model system. Using the more accurate hindcast wind and surface heat flux, re-run this model to better capture the temporal and spatial variability of the water currents and stratification at mooring sites and thus entire Cook Inlet.

Chapter 3: 2-D Numerical Modeling

Introduction

This chapter summarizes the development and validation of the 2-D barotropic numerical model and shows simulated results of Cook Inlet dynamics of tidal, wind-driven and river runoff origin.

Summary

In order to simulate tidal, wind-driven and river runoff forced currents and sea level elevations in Cook Inlet we have employed a 2-D coupled ice-ocean model developed by A. Proshutinsky (1993)for investigation of storm surges and tides in the Arctic Ocean. This model was modified and implemented for the specific conditions of Cook Inlet. The 2-D model captures significant variability of Cook Inlet circulation and sea level variability. In general, the direction of the predicted currents coincides with observations very well, although the simulated current velocities are larger than observed. The simulated tidal elevations are larger than observed (except Anchorage) but the phase of wave propagation is in good agreement with observations. Our tidal modeling experiments and comparison of simulated buoy trajectories with observed trajectories allow us to conclude that tidal dynamics dominate all other motions in the vicinity of Kalgin Island and to some degree in Upper Cook Inlet region. In the other regions, the wind driven motion significantly influences dynamics of Cook Inlet waters and can dominate when wind is strong enough.

Objectives

The first objective of this project was to complete a suite of initial modeling experiments using a 2-D model to identify how well this 2-D approach works for tidal, wind, and river runoff forcing. The second objective was to investigate the predictive capabilities of this approach and to develop a cheap and effective method for predictions of currents and sea levels in the Cook Inlet region.

Methodology

Our analyses of Cook Inlet dynamics obtained from historical and this project's observations show that, in many instances, the vertical structure of Cook Inlet currents is uniform and could be described by a 2-D model, consistent with earlier results (Johnson and Okkonen, 2000). Therefore, in order to simulate tidal, wind-driven and river runoff related currents in Cook Inlet as a first order approximation, we employed a 2-D coupled ice-ocean model developed by A. Proshutinsky (1993) for investigation of storm surges and tides in the Arctic Ocean. This model was modified and implemented for the specific conditions of Cook Inlet. Model description is available in Proshutinsky (1993), and in Proshutinsky et al. (2003). Precise bathymetry and particularly information about flooding/wetting areas or "mud flats" was needed in order to develop the 2-D model. The local boundary in the existing digital bathymetry data archives is represented by 0 meter depth. Creating detailed "new" bathymetry was not trivial because, to the best of our knowledge, this information did not exist in digital form. Thus, we have digitized satellite images from CRREL report 76-25 (CRREL 1976) in order to improve our model bathymetry and geometry.

A set of numerical experiments was designed to investigate the dynamics of Cook Inlet and has included several major activities:

- Simulation of tidal dynamics for separate tidal waves with dominating amplitudes in the region. These wave amplitudes were estimated based on harmonic constituents for Anchorage. Five semidiurnal waves (M2, S2, N2, 2N2, and K2) with largest sea level magnitudes (3.5 m, 1.0 m, 0.6 m, 0.14 m, and 0.27 m) and three diurnal waves (K1, O1, and Q1) with largest sea level magnitudes (0.69 m, 0.39 m, and 0.14 m) where selected for simulations. These waves describe approximately 75% of tidal dynamics in the region. In this project we could not add other waves because no data exist for them at the open boundaries of the region and we could not model them;

- Simulation of tidal dynamics of all eight tidal waves together to assess the role of non-linear effects due to tidal wave interactions. These interactions result in the generation of shallow waves of short periods (M4, M6, S4, S6, etc) inside the region and can improve the simulation results adding up to 10% in additional tidal elevation.

- Simulation of residual tidal currents due to nonlinear effects (nonlinear bottom friction and momentum advection) which can be represented by meso-scale eddies, local gyres and increased velocities in addition to the conventional tidal currents predicted based on tidal harmonic constituents. (See Figure 3.1, right, showing locations of observed rip currents in the region. These currents could originate from non-linear interactions of tidal waves when their velocities reach maximum);

- Simulation of water dynamics associated with river runoff. River runoff results in an additional residual element to the Cook Inlet circulation and, in general, provides a permanent outflow of the Cook Inlet waters (see Figure 3.1, left) We have also collected river runoff data (major and small river locations, river discharge and its seasonal variability). This information was used to simulate circulation of Cook Inlet driven by river runoff;

- Simulation of wind-driven effects in sea level changes and water dynamics.

A substantial amount of time was dedicated to the collection of data for validation of our simulated tidal sea level and current constituents. Approximately 100 moorings deployed by NOAA during 1973-1975 circulatory survey of Cook Inlet were analyzed, digitized and used for model validation and calibration purposes. Drifting buoy data were transferred in model coordinates in order to be compared with model results and used for model validation and calibration.

Model experiments and model validation results

Tidal dynamics

Simulation and validation

The 2-D tidal model of Cook Inlet has a spatial resolution of 1 km and was used to simulate 8 major tidal constituents (M2, S2, N2, 2N2, K2, K1, O1, and Q1). We obtained boundary conditions from satellite-based archives of tidal constituents for the Gulf of Alaska and Northern Pacific Ocean. For this purpose we have used the FES95.1/2 models which stem from the earlier pure hydrodynamic finite element solution FES94.1. An improved version of the FES94.1 solution was derived by assimilating into the hydrodynamic model of Grenoble the earlier empirical T/P CSR2.0 tidal solution using a representer method as developed by Egbert et al. [1994]. The CSR2.0 solutions were computed at the end of 1994 by the University of Texas from two years of TOPEX/POSEIDON data and with JGM-3 orbits. The assimilation was performed over five basins: North Atlantic, South Atlantic, Indian Ocean, North Pacific Ocean and South Pacific Ocean.

First, each tidal wave was simulated separately for at least 20 tidal cycles and amplitudes and phases for sea level elevations and velocity components were estimated after reaching a dynamic steady state when amplitudes and phases of tidal wave parameters (elevations and velocities stopped changing from cycle to cycle). The model results include tidal elevations and tidal velocity amplitudes and phases for eight major waves. Results are shown for four of them (data for other parameters could be found in CD tidal directory) in Figures 3.2 -3.13. The simulated tidal elevation amplitudes (see Figures 3.2, 3.5, 3.8, and 3.11; Tables 3.1 and 3.2) are larger than observed (except Anchorage) but the phases of wave propagation are in good agreement with observations. Figures 3.3, 3.4, 3.6, 3.7, 3.9, 3.10, 3.12 and 3.13 show the differences between observed and simulated tidal currents. Tables 1, 2, 3 and 4 in the Appendix show model validation results for tidal ellipses and their major characteristics (major and minor axis parameters, azimuth of the major ellipse axis and sense of the tidal vector rotation for four major tidal waves). In general, the direction of the predicted currents coincides very well with observations but the simulated current velocities are larger than observed.

In order to verify tidal currents in the entire region of Cook Inlet we used results of buoy drifts from our field work described in the previous section. Verification results are shown in Table 3.3 and in Figures 3.14 – 3.22. Figures showing all model verification results are presented in CD. Note that real buoys drift under at least four natural forcing components: tides, winds, thermohaline circulation, and river runoff. In this experiment, we compared buoy drift with only tidal component simulated by tidal model because all other components (winds, thermohaline, and river runoff are very uncertain but later we will show results of their modeling as well).

There are very good correlations (averaged among all buoy data) between observed and simulated U and V velocities. These correlation coefficients are 0.81 and 0.87, respectively for U and V observed and simulated components. Mean error (MER), mean absolute error (MAE), and root mean square errors (RMSE) for the U components are –3.6 cm/s, 19.1 cm/s, and 25.4 cm/s, respectively. For V components these errors are –8.5 cm/s, 29.6 cm/s, and 38.6 cm/s, respectively. These results allow us to conclude that indeed tidal dynamics dominate all other motions in the region. Figures 3.15 – 3.21 demonstrate that the observed and simulated velocities are in very good agreement in the vicinity of Kalgin Island (where rip currents are frequently observed) and also in the region located south east from Kalgin Island. In lower Cook Inlet (see Figure 3.22) when buoys leave regions with maximal tidal currents and where other driving forces prevail, the correlation between observed and simulated water velocities decreases and the buoy drift trajectories show less tidal looping and more straightforward drift out of Cook Inlet .

Interestingly, there are permanent and stable errors in U (–3.6 cm/s) and V (–8.5 cm/s) components suggesting that possibly there is a permanent current in the region which is not taken into account by our model. Existence of this current is confirmed by buoy trajectories shown in Figure 3.14. The “current” direction is 203° and speed is 9.2 cm/s and is probably driven by river runoff and prevailing winds (see Table 3.4 showing climatic winds). These components of the Cook Inlet water dynamics are discussed in the following sections: Residual tidal circulation, River runoff forced circulation, and Wind-driven circulation.

Residual tidal circulation

There is another possible cause of permanent currents associated with tidal dynamics – the so called residual currents generated by non-linear advection and non-linear bottom friction in the governing model equations. Together with oscillatory tidal currents, a residual tidal motion occurs due to nonlinear terms. This relatively weak (up to 10% of tidal flow) water motion may influence water properties, ice concentration, suspended sediments or oil spill behavior, and is also a frequent source of eddies. The residual tidal currents were obtained by averaging the tidal currents of each tidal wave over its tidal period. Figure 3.23 (left) depicts the residual water circulation due to M2 wave dynamics. Interestingly, all waves generate practically identical patterns of the residual tidal water circulation but velocities are different. Summing of residual tidal velocity components for three major diurnal and five major semidiurnal waves were obtained (Figure 3.23 right) showing “permanent” currents generated by eight tidal waves. The maximum tidal velocity associated with this dynamic is 76 cm/s. Eddies which are similar to eddies shown in Figure 3.23 (left) are also observed in Figure 3.23 (right). It would be interesting and important to verify their existence in this region. The 2-D model calculation results are in good agreement with the 3-D modeling results of “sub-tidal” currents shown in Figure 4.7 of section 4. For convenience we repeat this figure here as Figure 3.23 (right). The fact that these two results coincide (2-D and 3-D model results) confirms that simulations are correct and that the residual tidal dynamics dominates over thermohaline forcing in this region. We can also expect that the climatic salinity and temperature fields in this region are significantly influenced by tidal dynamics and have to reflect residual tidal circulation structure.

River runoff forced circulation

The river discharge data were downloaded from the USGS website, which covered a period from 1948 to 1988. Five sites were selected (see Figure 2.1 in 3-D modeling section): two for the Kenai River and three for the Susitna River. Daily averaging was made on all the stream flow records available on these five stations, and results are shown in Figure 2.2 in 3-D modeling section. For 2-D modeling purposes we calculate annual mean river discharges and simulated circulation in Cook Inlet under river runoff forcing only. In addition to the “observed” river runoff we also added a small “distributed” flux of water in all major bays imitating numerous discharges associated with small streams of small rivers and creeks. This is so called contribution of “un-gauged” flows. For this case, at the open boundaries of Cook Inlet we prescribed radiation boundary conditions allowing free exchange between Cook Inlet and ocean and, respectively free flow of river waters out of Cook Inlet. Figure 3.25 shows this circulation forced by river volume fluxes only. The most interesting feature of this circulation is that it resembles the schematics of Cook Inlet circulation shown in Figure 3.1 with its southward flow along the western coast and northward flow along the eastern coast. Comparing Figure 3.25 with Figure 3.1 (left) allows us to conclude that the river runoff is responsible for a general outflow of Cook Inlet waters to the Pacific Ocean. The northward flow along eastern coast is associated with fundamentals of fluid mechanics and flow follows f/H contour (where f – Coriolis parameter and H – depth). In the Cook Inlet case, river waters discharging along the eastern coast have to turn right to satisfy this rule. Later these waters turn left and flow south with the major outflow along western coast of the region. The velocities of simulated currents are relatively small and do not exceed 2-3 cm/s but their direction especially along the western coast is in agreement with the direction of current identified above as "permanent". The problem with this simulated velocity could be easily fixed increasing river runoff. For this case shown in Figure 3.25 we have used annual mean river discharge but in the real world this discharge can be much higher in summer months. Another parameter which can be responsible for "permanent" currents in the region is wind stress (discussed below).

Wind-driven circulation

Seasonal variability of Cook Inlet climatic characteristics in Anchorage including direction and speed of wind are shown in Table 3.4. There are two prevailing wind directions for this region: in winter northern winds with speeds of 7-10 m/s prevail and in summer SSE winds with practically the same speed as in winter dominate. Figures 3.26 and 3.27 show vertical mean vectors of Cook Inlet circulation under northern (winter regime) and southern (summer regime) climatic winds. These winds force opposite circulation regimes for these two wind directions with two major features. In general, in the relatively shallow regions of Cook Inlet with depths less than 15 m, the direction of wind-driven flow more or less coincides with the wind direction, or deviates a bit from it, under influence of coastline or depth contours. In deeper regions there is flow against the wind, compensating inflow to support the steady state circulation. Approximately 60 hours of wind action is needed to establish a relatively steady circulation. But because wind direction and speed change more frequently we expect that the steady state regime can not be reached and the wind-driven current variability is large. Figures 3.28, 3.29, 3.30 and 3.31 show wind-driven vertical mean currents generated by wind of 10 m/s for north, south, east and west directions, respectively. The duration of wind action was limited by 12 hours and the circulations shown are not at steady state regime. The major idea of showing these figures is to demonstrate that wind-driven water flows have a large range of variability. In these conditions their interaction with tides also changes and the observed current or buoy drift depends significantly on the combination of different forcing. On the other hand, in the vicinity of Kalgin Island the tidal currents prevail.

Accomplishments

A 2-D model was used to simulate the tidal phases and amplitudes, wind-driven circulation and water flows associated with river runoff. We digitized satellite images in order to improve our model bathymetry and geometry, collected river runoff data (major and small river locations, river discharge and its seasonal variability), collected data for validation of our simulated tidal sea level and current constituents from 54 moorings deployed by NOAA during 1973-1975 circulatory survey of Cook Inlet (see Tables 1-4 in the Appendix). These data were used to validate tidal model results. In addition, the information from 34 buoys was used to validate tidal velocities. Three tide gauges in Anchorage, Nikiski, and Seldovia were available for validation of tidal elevations. The major project accomplishment with the 2-D modeling is that the tidal constituents (amplitudes and phases) for eight major tidal waves (both for sea level elevations and velocity U and V components) were calculated for the Cook Inlet domain with the horizontal resolution of 1000 m and validated against observations. The results of model validation have shown that, in general, the simulated currents are higher than observed but the phases of the observed and simulated currents are in good agreement. In average, the errors of simulated current amplitudes do not exceed 15% of the observed amplitudes and the errors of simulated tidal phases are less than 20 degrees.

We have also assessed the roles of river runoff and wind forcing in the water dynamics of Cook Inlet. It was shown that river runoff is responsible for the general outflow of water from Cook Inlet with the intensification in summer and significant slowdown in winter. In contrast, the climatologic wind forcing results in the intensification of water outflow from the region in winter (when north winds prevail) and inflow in summer (with southern winds acting against intensified southward flow associated with river runoff). These results can be used for development of an inexpensive and relatively accurate method of prediction of sea level elevations and currents in the Cook Inlet region because tidal currents and elevation in every point of Cook Inlet is easy to calculate and predict at any time and for a long period in advance using our simulated tidal harmonic constituents. Then these predicted currents and sea levels can be corrected for wind and river runoff action adding wind-driven currents and currents associated with river runoff pre-calculated in advance for different wind speeds, directions and durations. Based on resultant currents it would be possible to predict water parcel trajectories having predicted wind parameters (speed, direction, and duration) without initiating and running models.

Remarks and Recommendations

The 2-D model results agree with observations well enough for practical purposes and the simulated sea level elevations and currents could be used for predictions as the first order approach. We conclude that model errors could be significantly reduced if better bathymetry data in the upper Cook Inlet and especially in Turnagain Arm is acquired. Wetting and drying mechanisms improve model results and should be incorporated in the models in order to achieve better agreement between observational and simulated data. In addition, in order to improve model results we recommend measuring sea surface heights at the open boundary of Cook Inlet during at least one month with sampling interval of one hour with 10-15 tides gauges.

We recommend deploying a set of bottom pressure gauges at least at coordinates of stations 25, 5, 4, 3, 6, 9, and 10 shown in Figure 3.32. Climatologic fields of water temperature and salinity are needed for the entire Cook Inlet to improve calculations of currents associated with the Cook Inlet thermohaline circulation that changes during the tidal cycle and seasonally.

In order to improve the model by introducing wetting and drying mechanisms, an up-to-date survey of the coastal region needs to be completed. This could be in the form of an airborne survey using digital photography, or through satellite data with digital extraction of the wet and dry coastlines. As there are errors in the geo-referencing in satellite imagery, this approach should be verified with known data from on-site validation.

In 1973-1975, NOAA carried out a circulation survey of Cook Inlet (Patchen et al., 1981). It would be important to repeat such a survey in the nearest future at least at the key locations important for navigation and especially in the regions of observed rip currents. It is important to compare tidal water current constituents measured 30 years ago with the recent data to quantify changes. We expect that the Cook Inlet tidal dynamics is determined by resonance conditions which depend on specifics of bathymetry and coastline configuration. Under influence of coastal erosion and significant sediment transport these characteristics could have changed during the past 30 years and therefore tidal parameters of Cook Inlet could probably experience change as well.

References

Table 3.1. Observed/simulated amplitude and phase for semidiurnal constituents M2, S2, N2 and K2.

Station	M2 tidal wave		S2 tidal wave		N2 tidal wave		K2 tidal wave	
	Amplitude cm	Phase degree	Amplitude cm	Phase degree	Amplitude cm	Phase degree	Amplitude cm	Phase degree
Nikiski	251/292	030/039	087/105	062/072	049/050	359/017	025/017	054/076
Seldovia	223/265	324/339	082/088	359/007	047/042	297/304	023/019	353/349
Anchorage	353/287	108/109	100/148	150/150	060/098	082/085	027/048	142/151

Chen, C. et al. 2003. An unstructured grid, finite-volume, three dimensional, primitive equation ocean model: application to coastal ocean and estuaries. J. Atmospheric & Oceanic Tech. 20, 159-186.

CRREL. 1976. Baseline data on the oceanography of Cook Inlet, Alaska. CRREL, Hanover, New Hampshire. 83 p.

Johnson, M.A. and S. Okkonen. 2000. Proceedings Cook Inlet Oceanography Workshop, OCS Study MMS 2000-043 Final Report. 118pp.

Le Provost et al. 1995. Ocean tides fro and from TOPEX/POSEIDON. Science 267, 639-642.

Kowalik Z. and A. Proshutinsky. 1993 Diurnal tides in the Arctic Ocean. J. Geophys. Res., 98(C9), 16449-16448.

Patchen, R.C. et al. 1981. Cook Inlet Circulatory Survey: 1973-1975. NOS Oceanographic Circulatory Survey Report No 4, NOAA, June 1981.

Proshutinsky, A. 1993. Arctic Ocean Level Oscillations. Gidrometeoizdat, St. Petersburg. 216 p.

Proshutinsky, A. M. Johnson, T. Proshutinsky and J. Maslanik. 2003. Beaufort and Chukchi Sea seasonal variability in two Arctic climate states, University of Alaska Coastal Marine Institute, OCS Study MMS 2003-024 Final Report. 198 p.

Table 3.2. Observed/simulated amplitude and phase for diurnal constituents.

Station	O1 tidal wave		K1 tidal wave		Q1 tidal wave	
	Amplitude cm	Phase degree	Amplitude cm	Phase degree	Amplitude cm	Phase degree
Nikiski	069/089	307/291	039/039	291/255	006/009	290/249
Seldovia	056/065	279/270	034/028	263/246	006/007	258/242
Anchorage	069/112	341/299	039/047	322/268	006/010	331/257

Table 3.3. Statistics of differences between observed velocities of buoy drift and simulated tidal velocities at buoy locations. COR – correlation coefficient between buoy and simulated velocities, MER – mean error (cm/s), MAR – mean absolute error (cm/s), RMSE – root mean square error (cm/s) for U (parallel) and V (meridian) components of buoy drifts (see also Figures 3.14-3.20).

Buoy number	U - velocity component				V - velocity component			
	COR	MER	MAR	RMSE	COR	MER	MAR	RMSE
36193-1	0.86	-6.9	18.5	23.8	0.82	1.6	30.6	42.8
36193-2	0.81	-4.6	24.8	31.5	0.79	0.6	41.6	55.8
36193-3	0.91	-4.1	16.7	22.2	0.92	-11.7	28.9	37.3
36197-1	0.74	-5.4	23.3	23.5	0.84	-10.3	35.6	46.1
36229-1	0.79	-5.8	26.5	34.1	0.86	-2.0	38.4	49.3
36229-2	0.68	-0.3	19.2	24.8	0.89	-7.7	22.1	30.8
36229-3	0.68	-8.4	16.5	22.6	0.91	-8.7	17.9	22.5
36230-1	0.86	-5.3	17.9	24.3	0.91	-12.9	29.7	40.6
36236-1	0.79	-9.3	24.4	31.3	0.82	-11.6	42.6	62.3
36236-2	0.77	-3.7	15.9	22.0	0.86	-9.8	23.2	32.2
36237-1	0.75	-1.5	22.5	28.9	0.66	5.0	39.3	50.2
36237-2	0.80	-2.2	28.2	36.3	0.86	-19.1	45.0	61.1
36246-1	0.80	-3.8	14.7	20.1	0.87	-7.8	17.8	26.5
36247-1	0.84	-6.3	23.8	31.8	0.91	-11.6	47.8	63.6
36248-1	0.88	-4.8	17.7	24.4	0.92	-7.5	30.5	40.1
36248-2	0.89	-0.9	13.9	18.5	0.88	2.8	26.0	33.9
36248-3	0.82	-7.5	19.5	24.8	0.85	-5.7	37.2	47.6
36248-4	0.55	-4.5	15.3	37.2	0.61	-18.9	22.5	46.2
36250-1	0.88	-3.9	20.3	26.5	0.92	-3.9	39.5	48.6
39907-1	0.82	-2.3	23.9	30.5	0.88	-9.3	32.1	42.8
39907-2	0.77	-3.5	14.3	22.4	0.92	-8.3	17.4	23.6
39908-1	0.79	-8.9	22.0	32.3	0.88	-10.7	27.6	36.9
39908-2	0.86	-2.2	11.4	15.6	0.89	-15.0	19.1	25.9
39909-1	0.75	5.1	32.3	47.9	0.82	-16.4	39.5	59.3
39909-2	0.80	1.9	17.5	23.5	0.77	-2.7	37.1	51.3
39909-3	0.89	-6.3	13.4	17.6	0.90	-15.4	21.4	29.2
39910-1	0.90	-0.8	12.5	17.1	0.95	-3.3	21.4	28.0
39910-2	0.81	4.0	29.3	39.2	0.86	-8.9	36.3	48.4
39912-1	0.87	-2.4	17.7	25.3	0.86	-2.7	27.7	39.1
39912-2	0.91	1.5	8.8	11.6	0.97	0.8	10.6	14.9
39913-1	0.84	-3.4	19.7	26.2	0.91	-7.2	32.3	40.2
39914-1	0.66	-4.4	20.8	27.2	0.84	-3.2	25.7	34.5
39991-1	0.77	-3.0	29.5	36.8	0.86	-14.8	39.8	53.7
39994-2	0.76	-3.6	12.6	17.9	0.92	-5.0	20.5	28.1
39995-1	0.74	-3.4	13.8	18.8	0.93	-4.0	15.0	20.1
39995-2	0.80	-8.6	22.7	29.1	0.69	-5.3	19.5	26.9
39995-1	0.90	0.1	9.3	12.2	0.97	1.5	13.4	18.7
39995-2	0.83	-0.6	20.7	25.6	0.95	-1.9	25.1	30.8
39996-1	0.90	0.1	9.3	12.1	0.97	1.5	13.4	17.8
39997-1	0.90	1.8	9.2	12.2	0.97	1.5	14.0	18.6
39998-1	0.50	-5.1	16.9	26.2	0.88	-5.9	37.2	47.8
39998-2	0.69	-7.9	24.5	30.3	0.84	-29.9	39.1	51.2
57627-1	0.88	-2.7	22.2	28.8	0.88	-7.3	31.2	42.6
57627-2	0.86	-4.1	12.1	20.3	0.92	-7.4	15.2	21.6
57628-1	0.83	-4.8	22.1	30.6	0.83	-15.5	34.6	53.0
57629-1	0.87	-1.7	12.9	16.9	0.87	5.0	36.8	46.4
57629-1	0.69	-7.5	19.3	24.9	0.73	-20.4	36.1	49.3
57630-1	0.85	-6.4	12.1	15.9	0.95	-8.7	18.6	23.2
57632-1	0.84	-3.7	15.4	22.8	0.93	-8.8	25.3	33.1
57634-1	0.90	-10.7	17.4	23.6	0.93	-19.3	27.3	35.2
57635-1	0.84	-2.1	22.5	28.8	0.88	-7.2	30.6	37.1
57636-1	0.86	-4.2	18.0	24.1	0.88	-14.1	28.0	37.4
57637-1	0.78	-8.0	23.1	37.1	0.81	-17.6	37.3	55.1
57638-1	0.88	-3.8	17.3	25.5	0.91	-12.3	29.7	40.6
57641-1	0.69	2.4	43.2	18.1	0.83	-30.6	73.4	89.3
Mean	0.81	-3.6	19.1	25.4	0.87	-8.5	29.6	38.6

Table 3.4. Climate characteristics of Cook Inlet from Anchorage climate report.

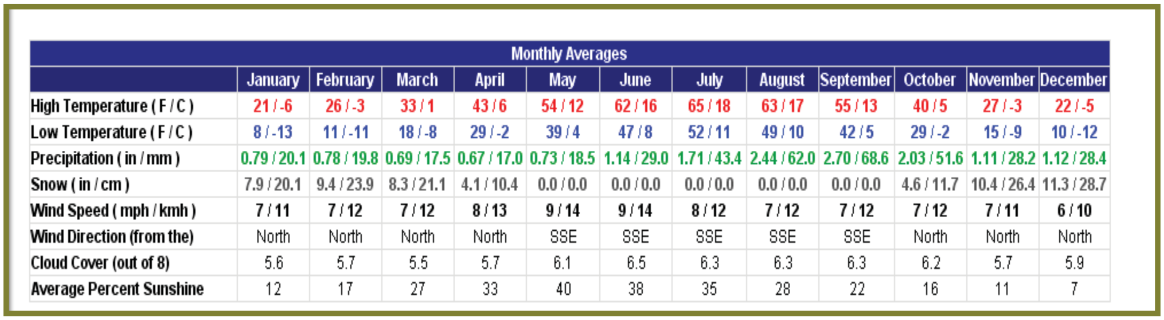

Monthly Averages

	January	February	March	April	May	June	July	August	September	October	November	December
High Temperature (F / C)	21 / -6	26 / -3	33 / 1	43 / 6	54 / 12	62 / 16	65 / 18	63 / 17	55 / 13	40 / 5	27 / -3	22 / -5
Low Temperature (F / C)	8 / -13	11 / -11	18 / -8	29 / -2	39 / 4	47 / 8	52 / 11	49 / 10	42 / 5	29 / -2	15 / -9	10 / -12
Precipitation (in / mm)	0.79 / 20.1	0.78 / 19.8	0.69 / 17.5	0.67 / 17.0	0.73 / 18.5	1.14 / 29.0	1.71 / 43.4	2.44 / 62.0	2.70 / 68.6	2.03 / 51.6	1.11 / 28.2	1.12 / 28.4
Snow (in / cm)	7.9 / 20.1	9.4 / 23.9	8.3 / 21.1	4.1 / 10.4	0.0 / 0.0	0.0 / 0.0	0.0 / 0.0	0.0 / 0.0	0.0 / 0.0	4.6 / 11.7	10.4 / 26.4	11.3 / 28.7
Wind Speed (mph / kmh)	7 / 11	7 / 12	7 / 12	8 / 13	9 / 14	9 / 14	8 / 12	7 / 12	7 / 12	7 / 12	7 / 11	6 / 10
Wind Direction (from the)	North	North	North	North	SSE	SSE	SSE	SSE	SSE	North	North	North
Cloud Cover (out of 8)	5.6	5.7	5.5	5.7	6.1	6.5	6.3	6.3	6.3	6.2	5.7	5.9
Average Percent Sunshine	12	17	27	33	40	38	35	28	22	16	11	7

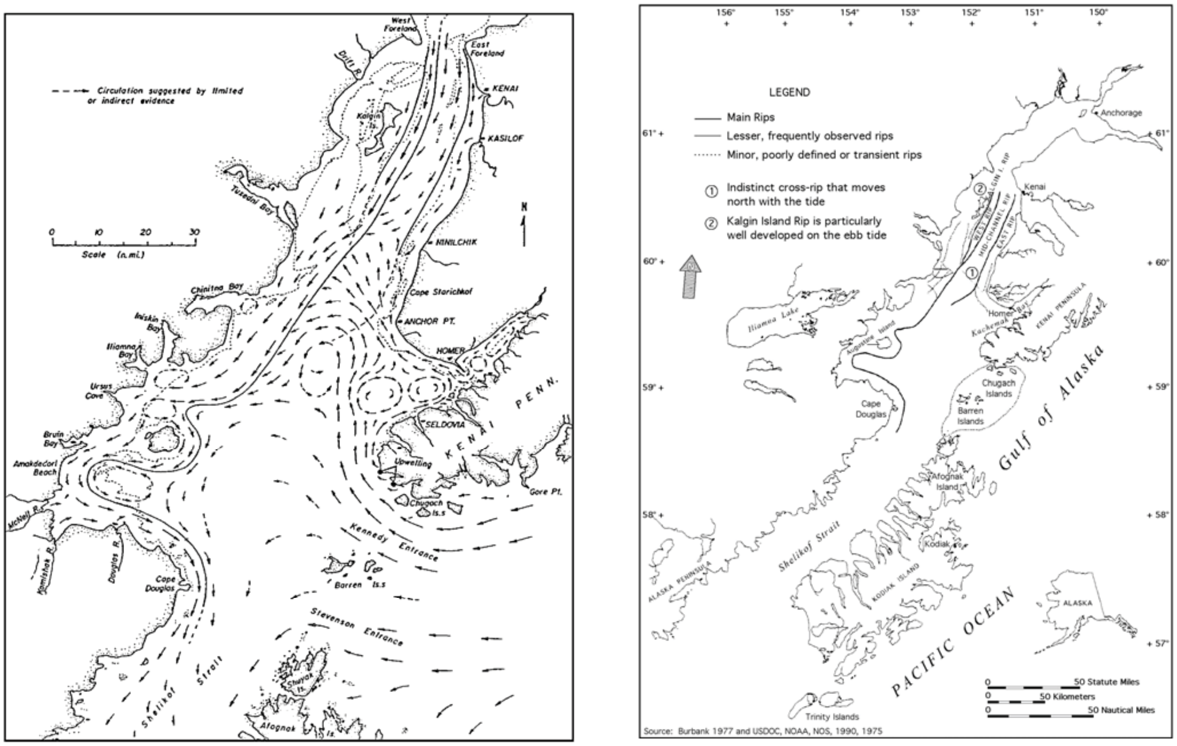

Source: Burbank 1977 and USDOC, NOAA, NOS, 1990, 1975

Figure 3.1. Left: Schematics of Cook Inlet circulation (Burbank, 1977). Note outflow in Upper Cook Inlet probably associated with river runoff. Right: Patterns of Cook Inlet Rip currents (Burbanks, 1977; USDOC, NOAA, NOS, 1975, 1990). Rip currents are observed in the vicinity of Kalgin Island where tidal dynamics is maximal and where "permanent" outflow velocities are maximal as well.

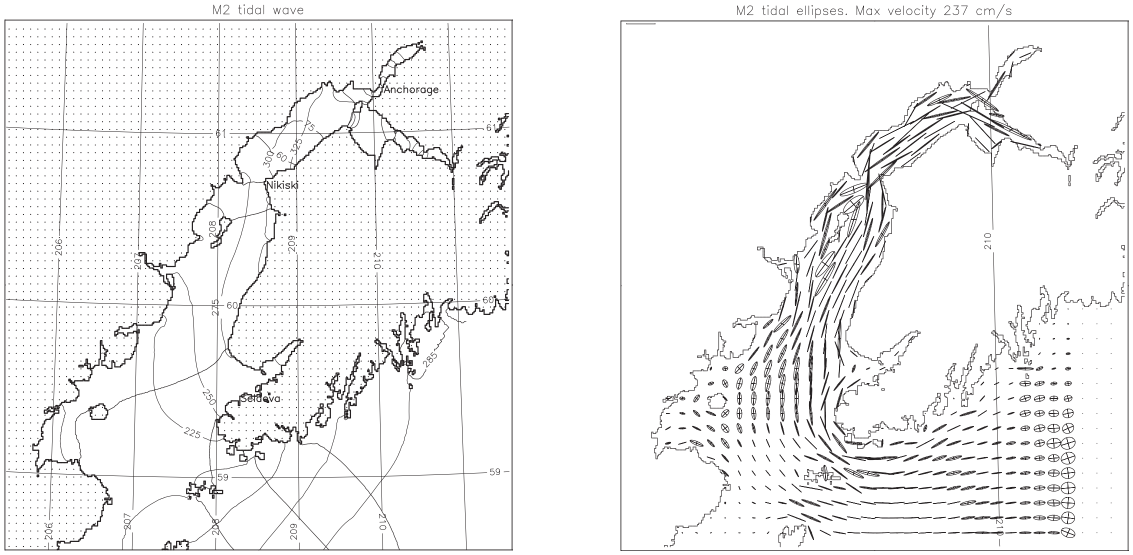

Figure 3.2. Left: Computed amplitude (in centimeters, thin line) and phase (in degrees, thick line) of surface elevation for the semidiurnal constituent M2. Right: Computed ellipses of the M2 tidal wave.

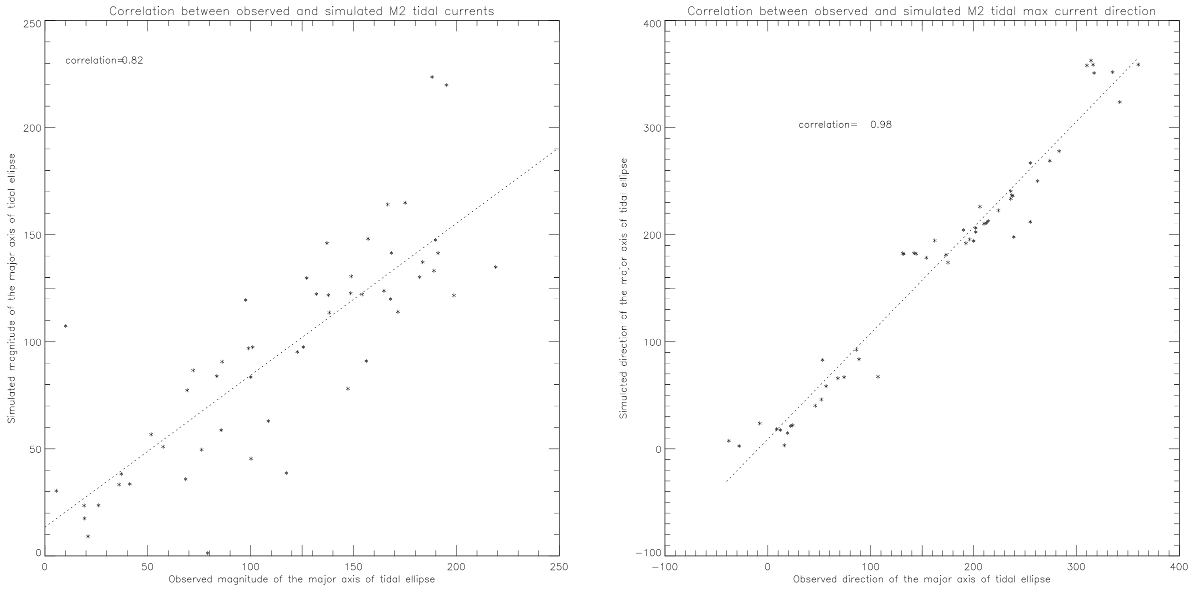

Figure 3.3. Left: Correlation between observed and computed M2 tidal velocities representing major axis of tidal ellipse (cm/s). Right: Correlation between observed and computed directions (degrees) of major axis of M2 tidal ellipses.

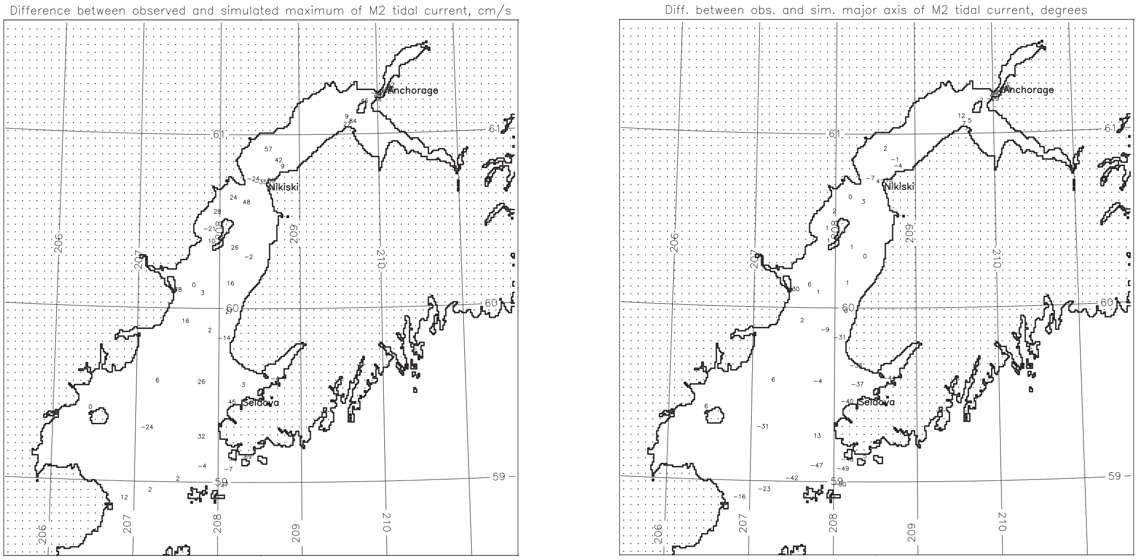

Figure 3.4. Left: Difference (cm/s) between observed and simulated M2 tidal velocities representing major axis of tidal ellipses. Right: Difference (degrees) between observed and simulated directions of major M2 tidal ellipses.

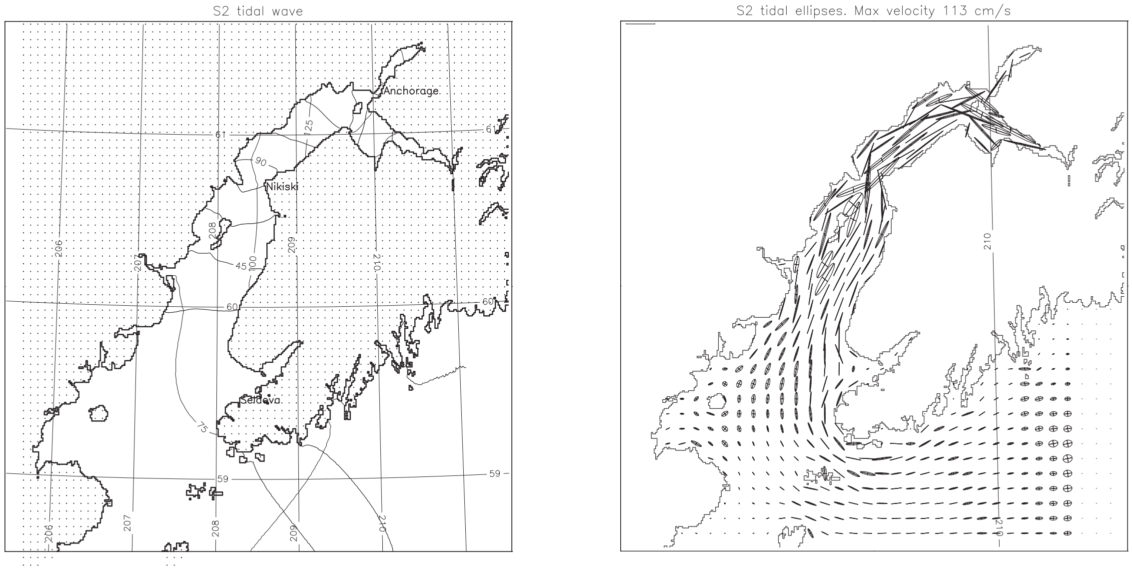

Figure 3.5. Left: Computed amplitude (in centimeters, thin line) and phase (in degrees, thick line) of surface elevation for the semidiurnal constituent S2. Right: Computed ellipses of the S2 tidal wave.

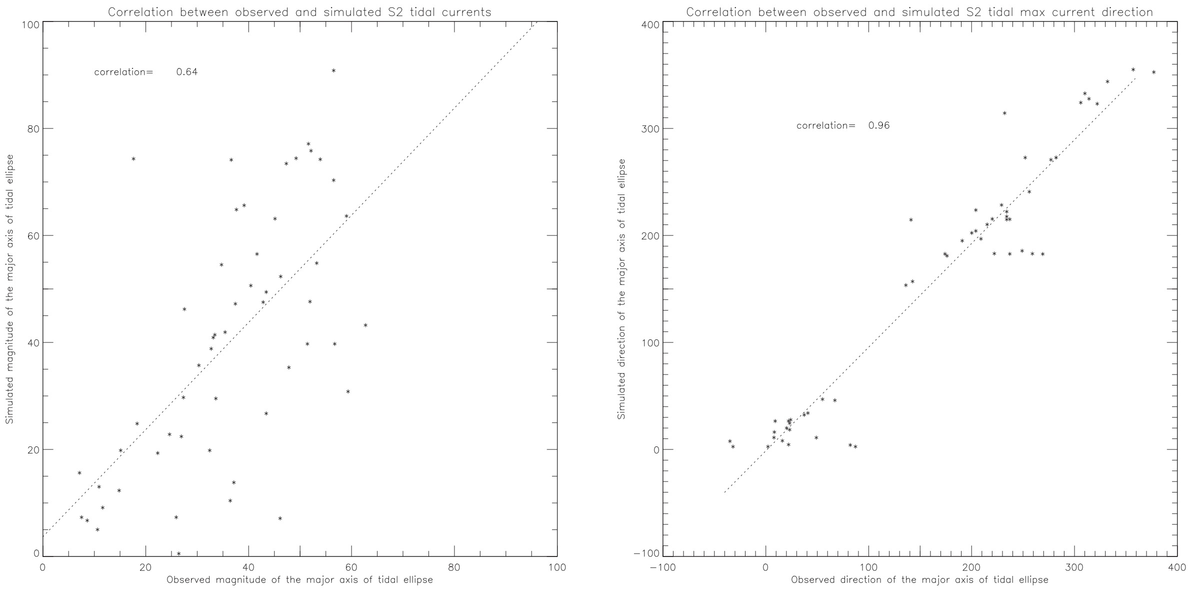

Figure 3.6. Left: Correlation between observed and computed S2 tidal velocities representing major axis of tidal ellipse (cm/s). Right: Correlation between observed and computed directions (degrees) of major axis of S2 tidal ellipses.

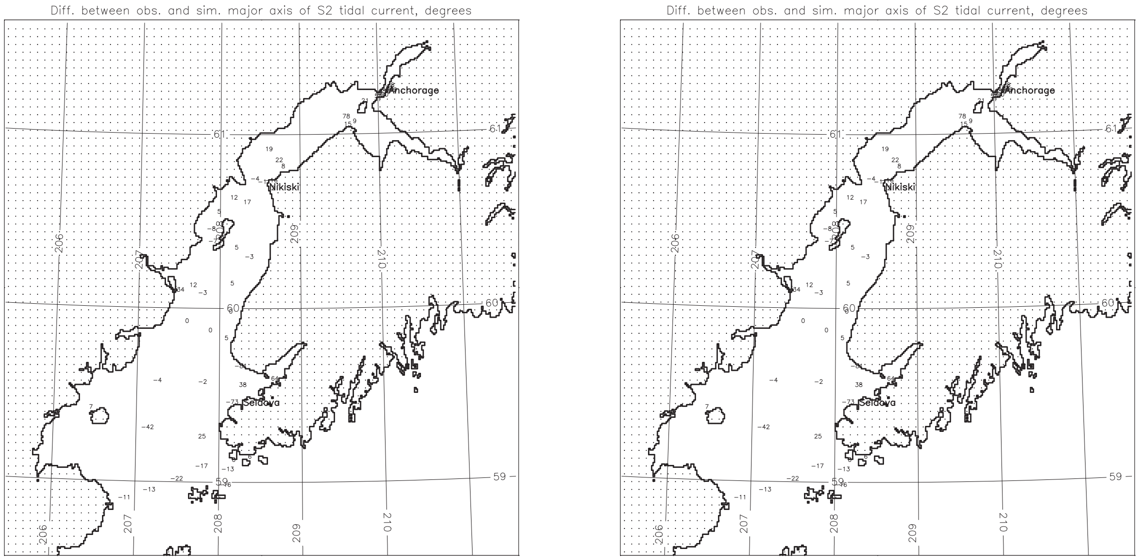

Figure 3.7. Left: Difference (cm/s) between observed and simulated S2 tidal velocities representing major axis of tidal ellipses. Right: Difference (degrees) between observed and simulated directions of major S2 tidal ellipses.

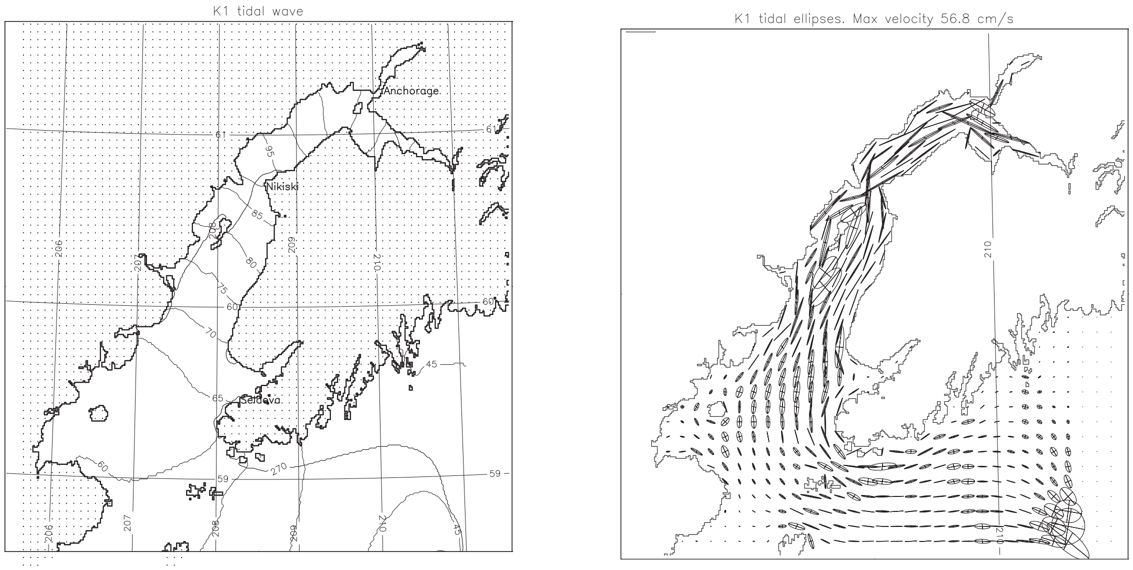

Figure 3.8. Left: Computed amplitude (in centimeters, thin line) and phase (in degrees, thick line) of surface elevation for the semidiurnal constituent K1. Right: Computed ellipses of the K1 tidal wave.

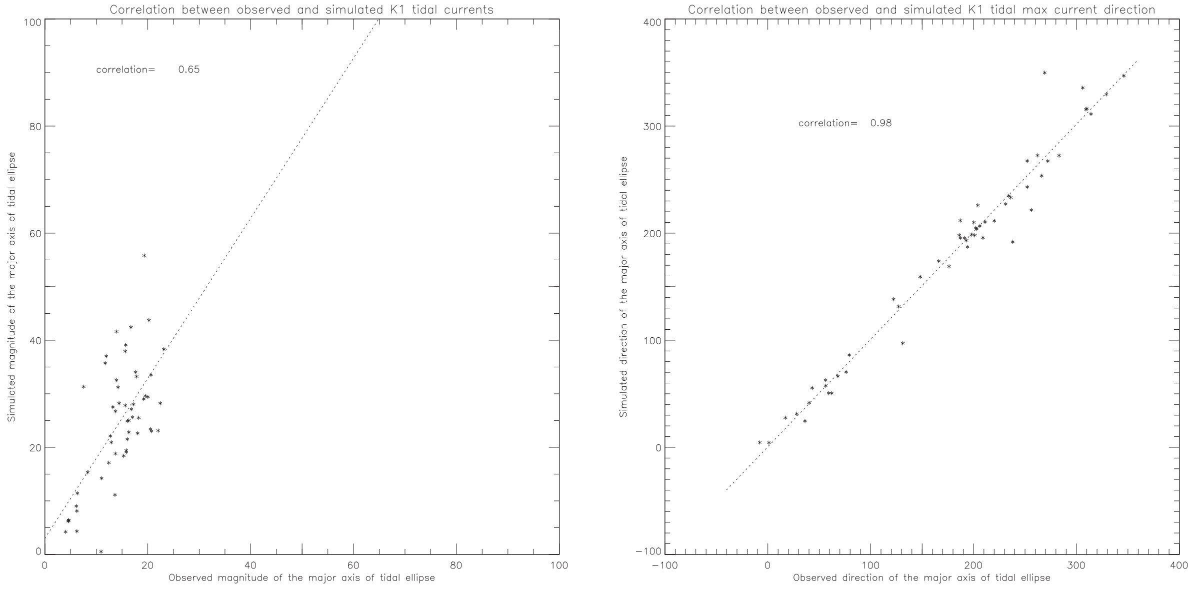

Figure 3.9. Left: Correlation between observed and computed K1 tidal velocities representing major axis of tidal ellipse (cm/s). Right: Correlation between observed and computed directions (degrees) of major axis of K1 tidal ellipses.

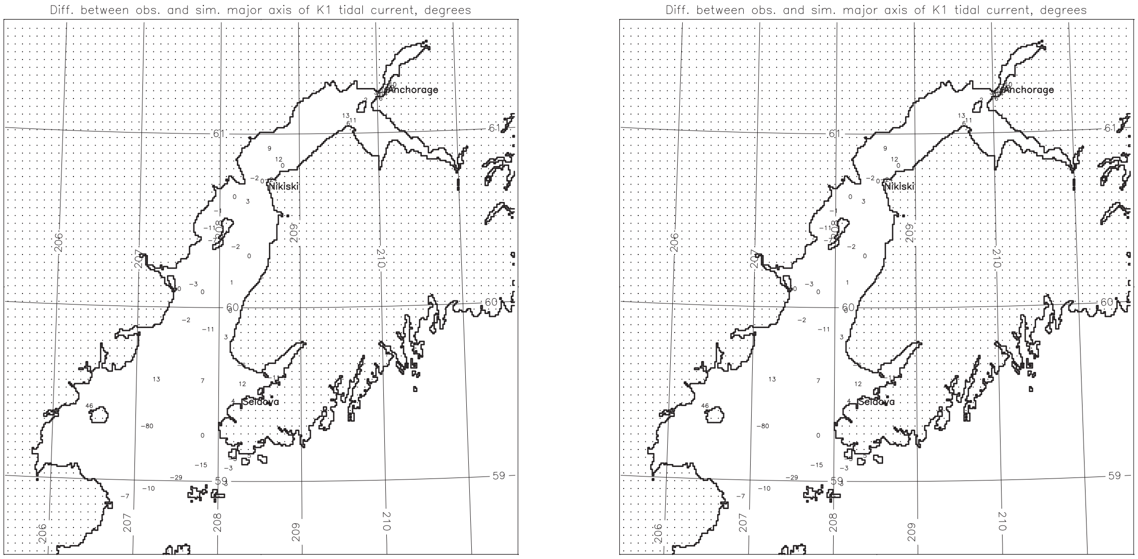

Figure 3.10. Left: Difference (cm/s) between observed and simulated K1 tidal velocities representing major axis of tidal ellipses. Right: Difference (degrees) between observed and simulated directions of major K1 tidal ellipses.

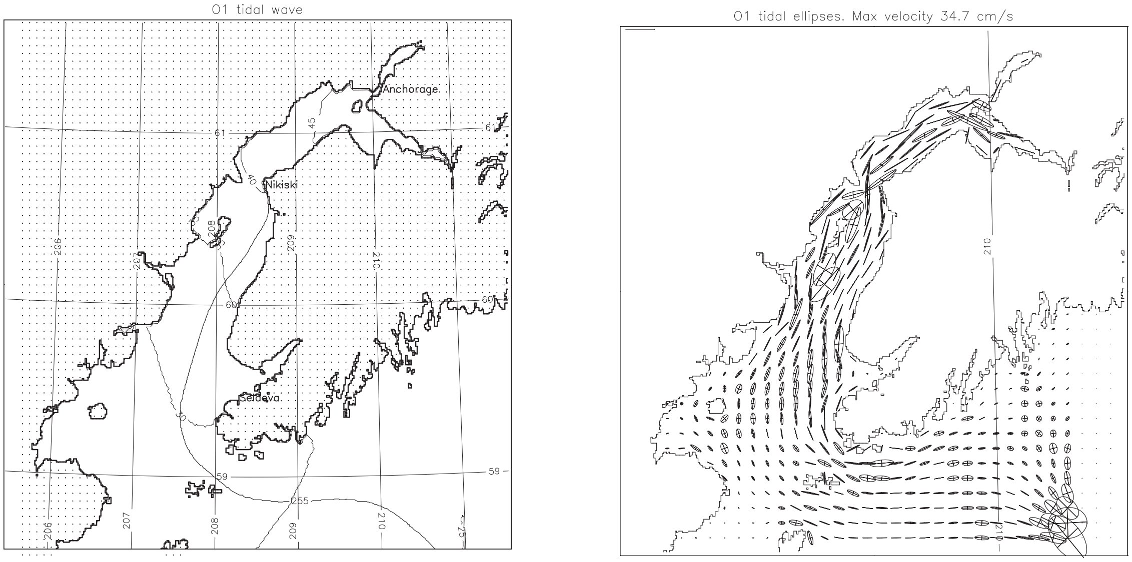

Figure 3.11. Computed amplitude (in centimeters, thin line) and phase (in degrees, thick line) of surface elevation for the diurnal constituent O1.

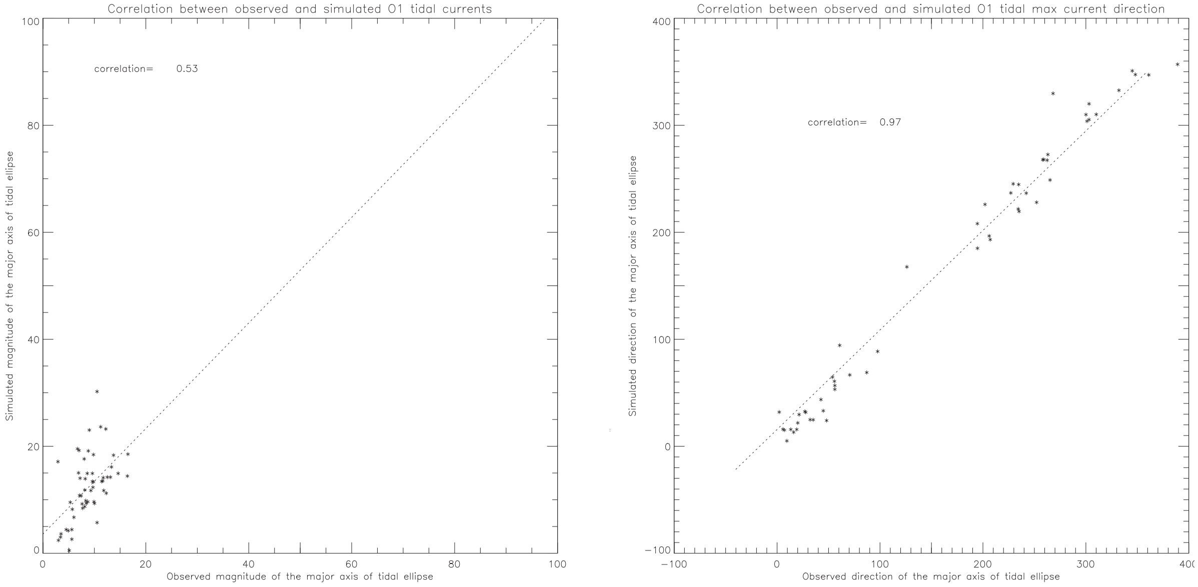

Figure 3.12. Left: Correlation between observed and computed O1 tidal velocities representing major axis of tidal ellipse (cm/s). Right: Correlation between observed and computed directions (degrees) of major axis of O1 tidal ellipses.

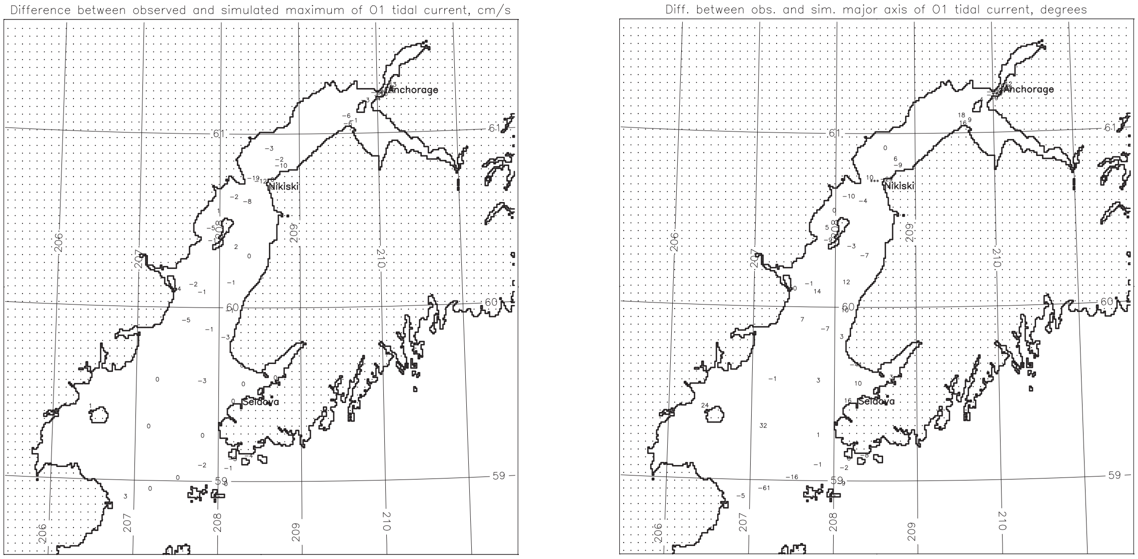

Figure 3.13. Left: Difference (cm/s) between observed and simulated O1 tidal velocities representing major axis of tidal ellipses. Right: Difference (degrees) between observed and simulated directions of major O1 tidal ellipses.

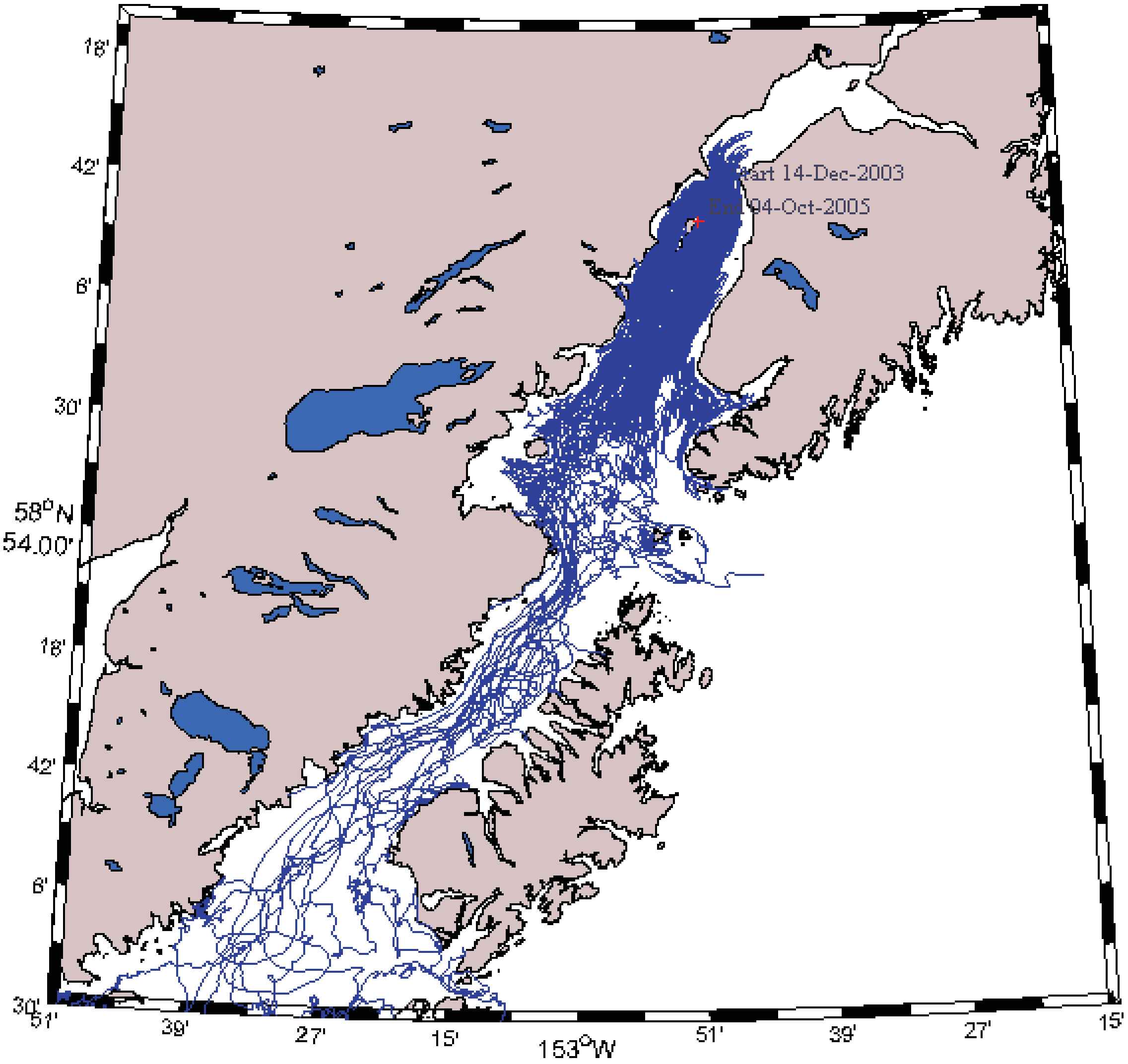

Figure 3.14. Trajectories of 45 drifting buoys deployed in 2003-2005. Note that most of buoys tend to leave Cook Inlet suggesting existence of permanent surface water outflow associated with river runoff and possibly wind regime.

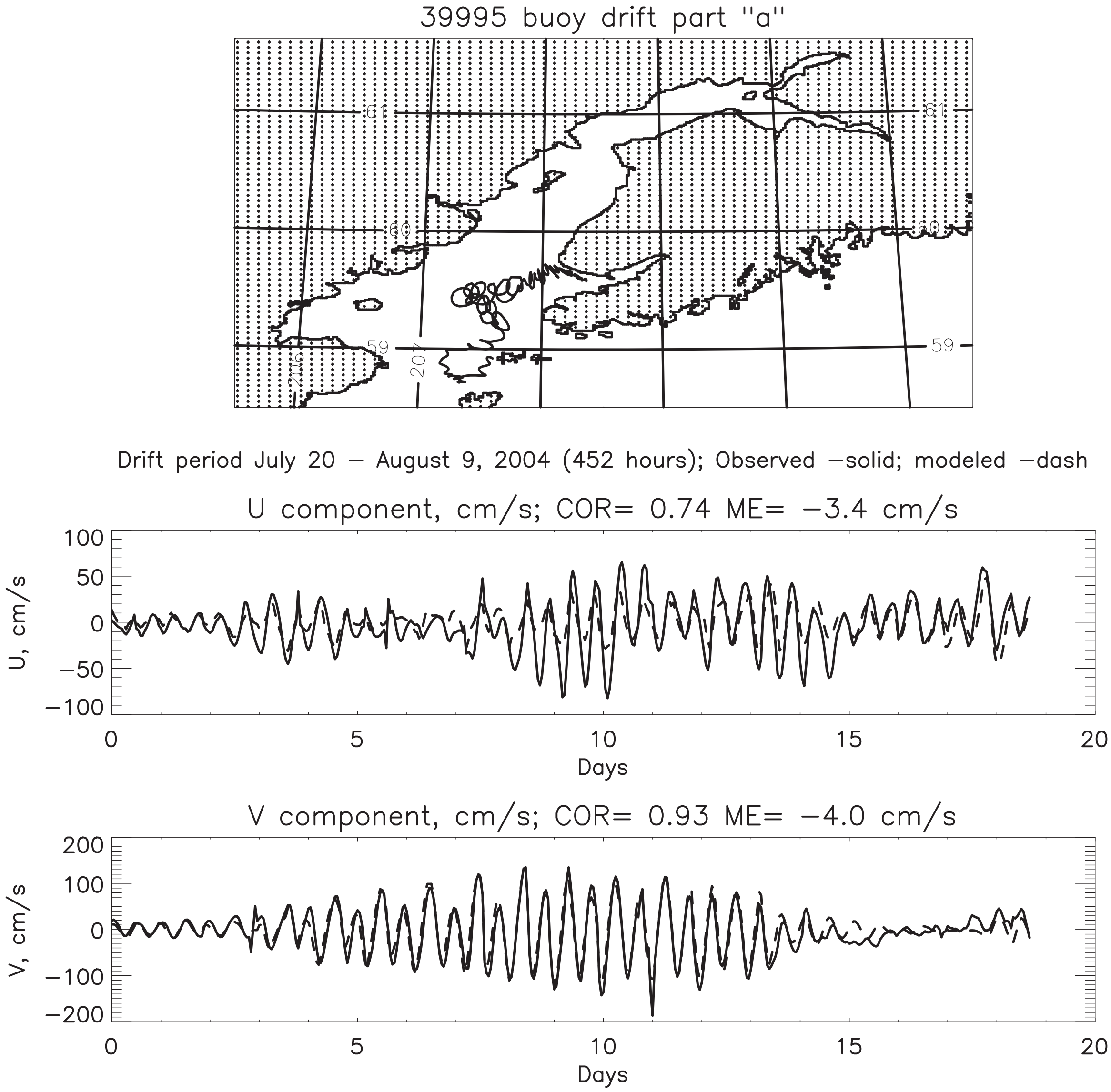

Figure 3.15. Upper panel shows buoy #39995 trajectories. Bottom graphs show validation for simulated tidal velocities (U – zonal and V – meridian components) against observed U and V components of buoy drift. COR – correlation coefficient between observed and simulated velocities; ME – mean error.

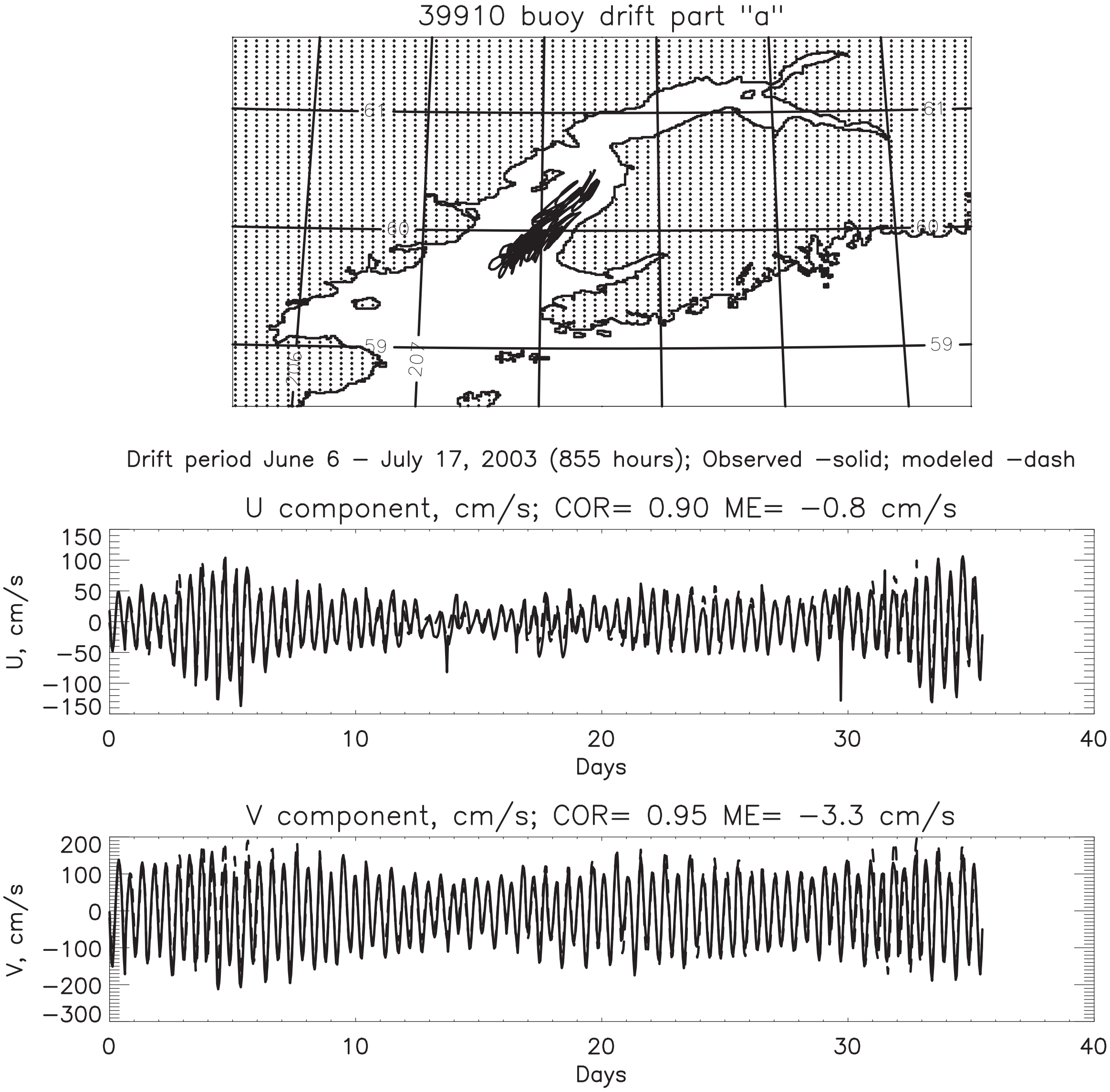

Figure 3.16. Upper panel shows buoy #39910 trajectories. Bottom graphs show validation for simulated tidal velocities (U – zonal and V – meridian components) against observed U and V components of buoy drift. COR – correlation coefficient between observed and simulated velocities; ME – mean error.

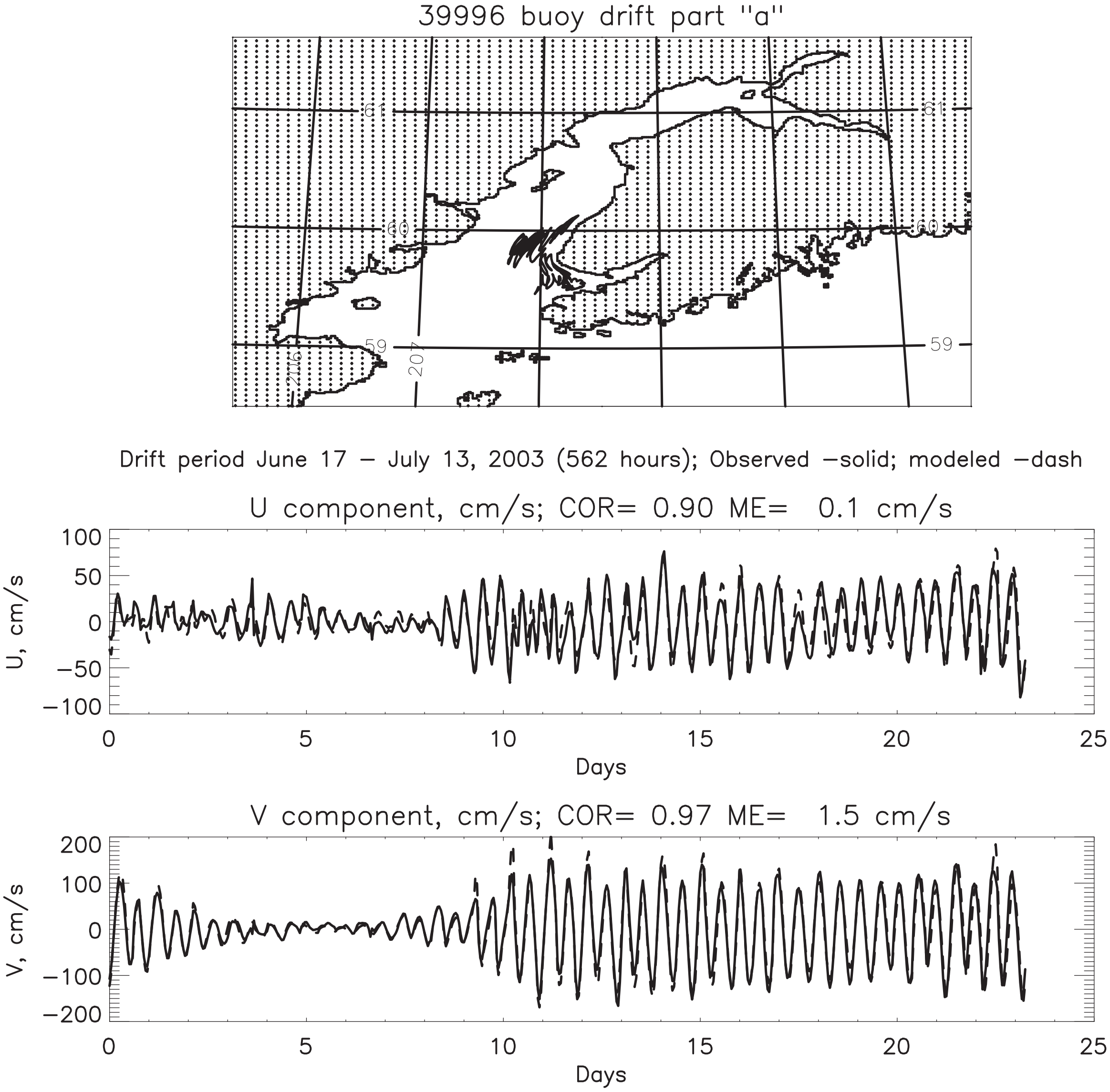

Figure 3.17. Upper panel shows buoy #39996 trajectories. Bottom graphs show validation for simulated tidal velocities (U – zonal and V – meridian components) against observed U and V components of buoy drift. COR – correlation coefficient between observed and simulated velocities; ME – mean error.

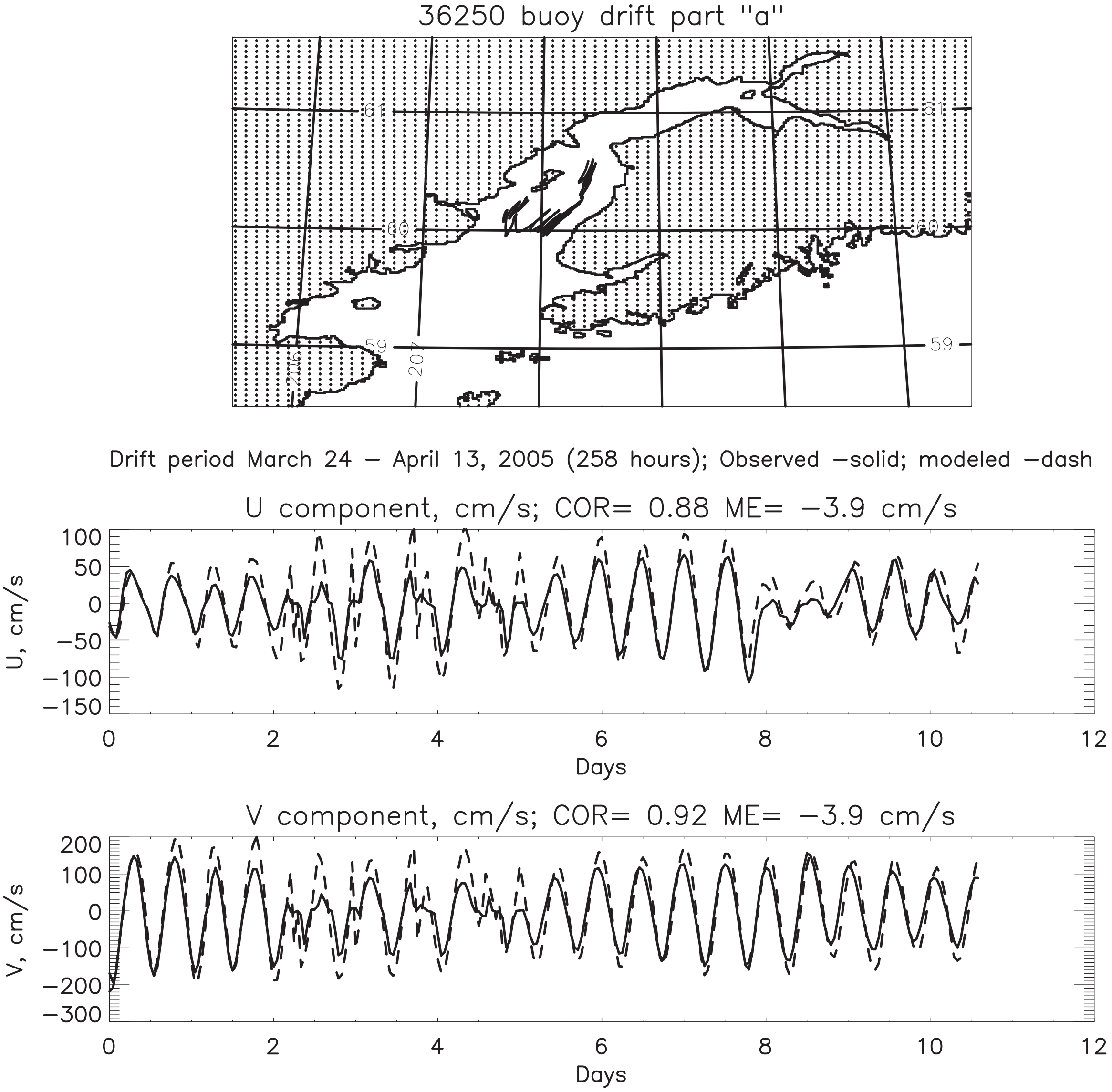

Figure 3.18. Upper panel shows buoy #39910 trajectories. Bottom graphs show validation for simulated tidal velocities (U – zonal and V – meridian components) against observed U and V components of buoy drift. COR – correlation coefficient between observed and simulated velocities; ME – mean error.

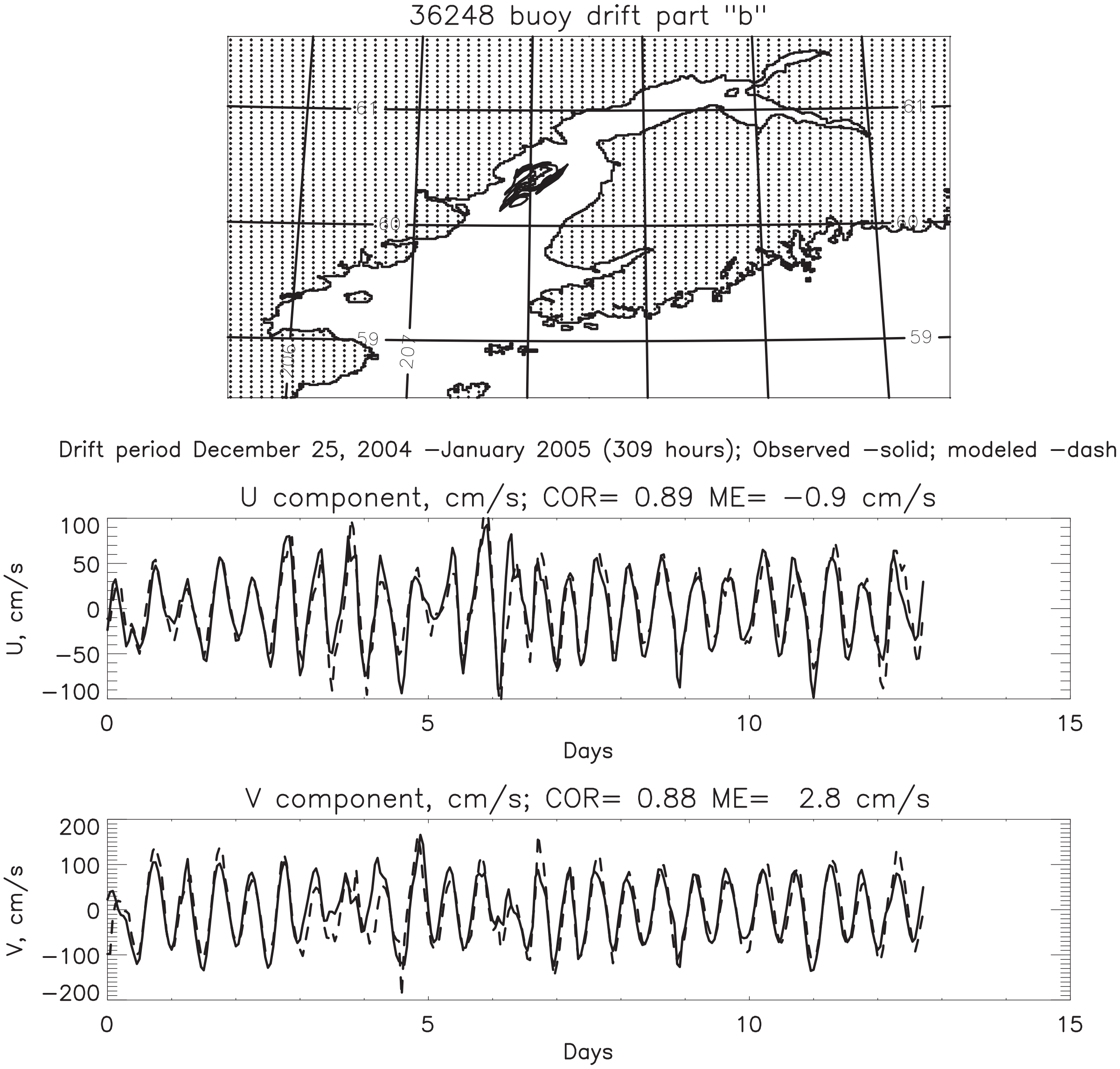

Figure 3.19. Upper panel shows buoy #36248 trajectories. Bottom graphs show validation for simulated tidal velocities (U – zonal and V – meridian components) against observed U and V components of buoy drift. COR – correlation coefficient between observed and simulated velocities; ME – mean error.

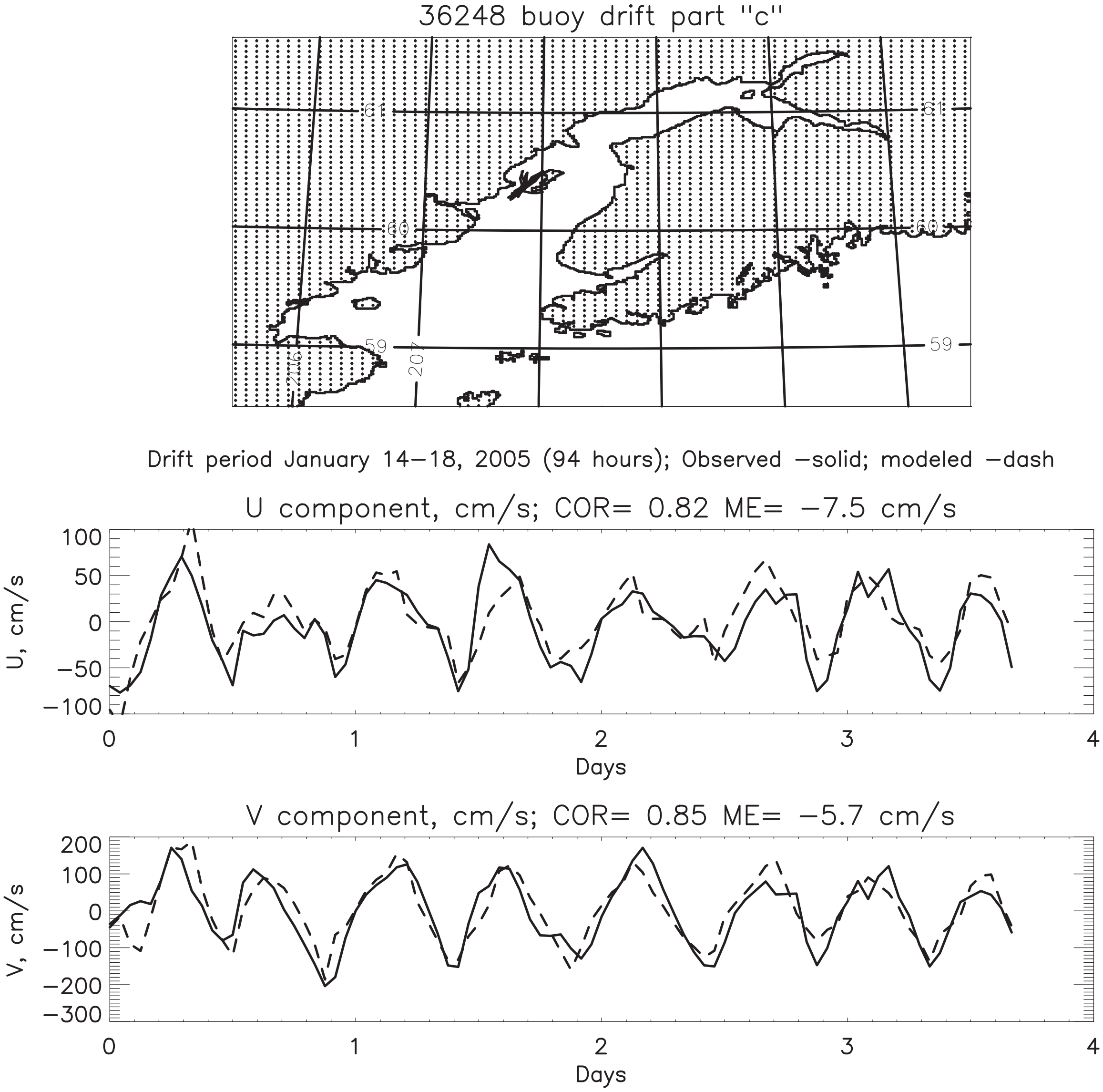

Figure 3.20. Upper panel shows buoy #36248 (part 2) trajectories. Bottom graphs show validation for simulated tidal velocities (U – zonal and V – meridian components) against observed U and V components of buoy drift. COR – correlation coefficient between observed and simulated velocities; ME – mean error.

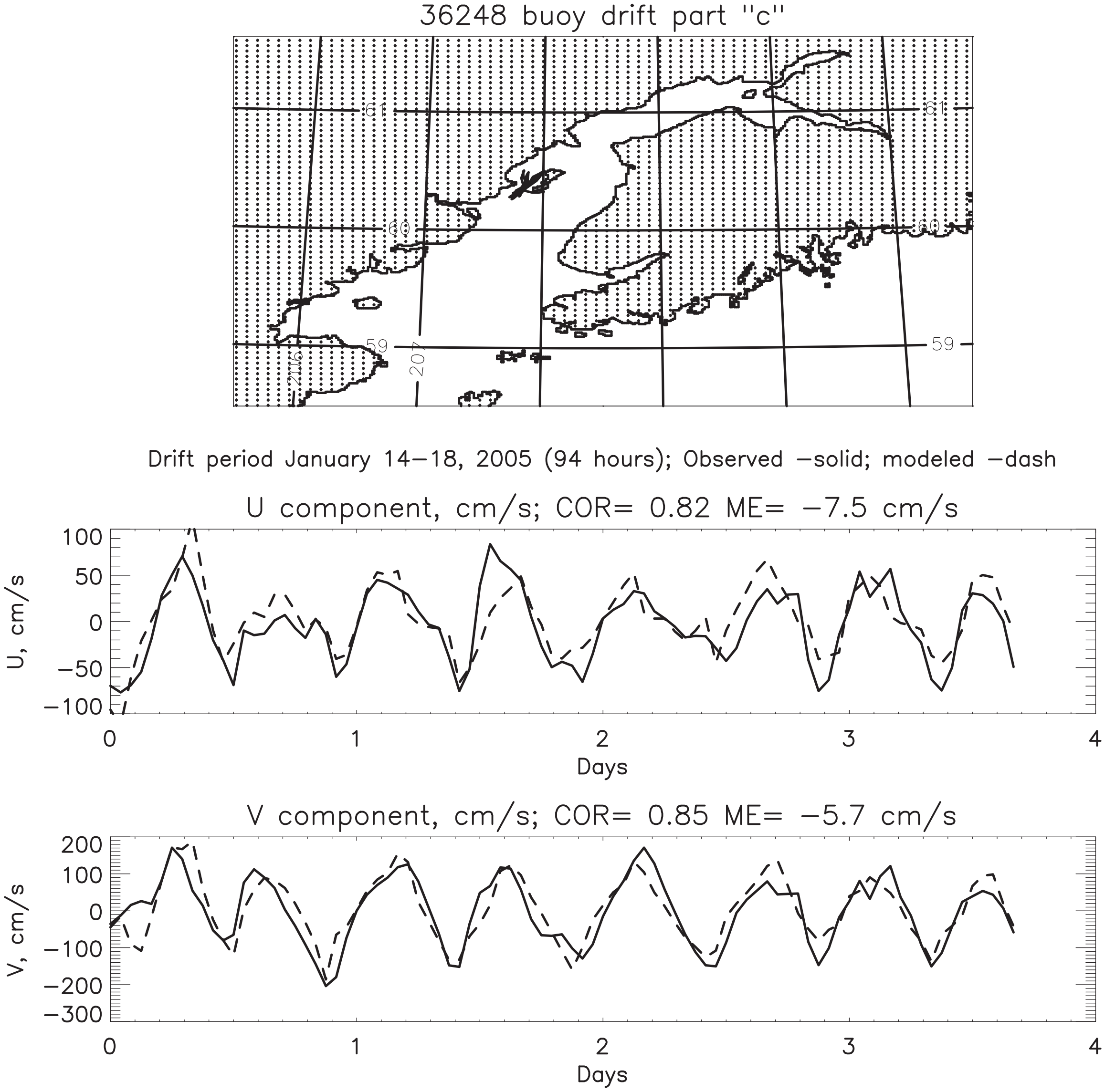

Figure 3.21. Upper panel shows buoy #39909 trajectories. Bottom graphs show validation for simulated tidal velocities (U – zonal and V – meridian components) against observed U and V components of buoy drift. COR – correlation coefficient between observed and simulated velocities; ME – mean error.

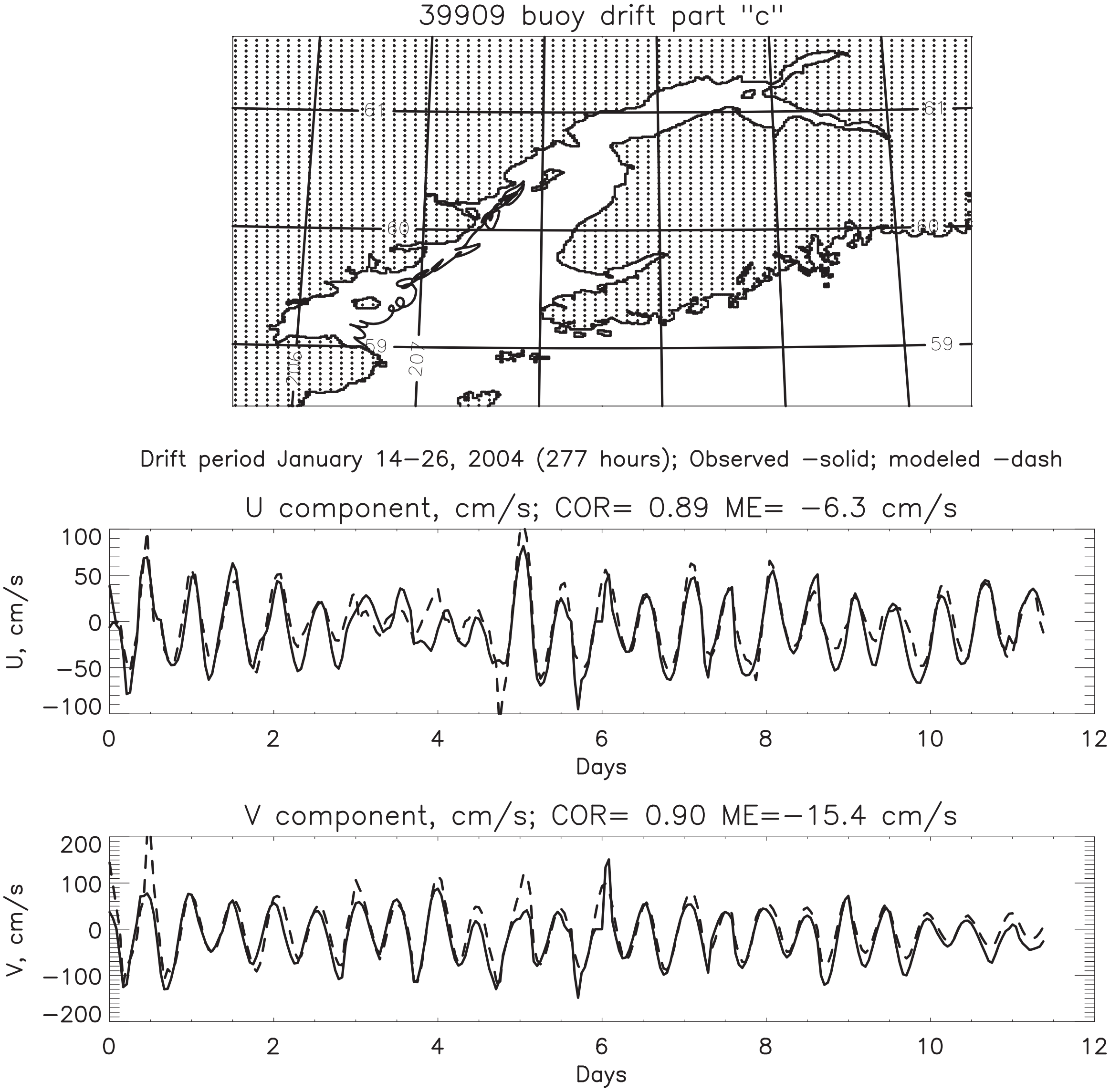

39909 buoy drift part "c"

Drift period January 14–26, 2004 (277 hours); Observed –solid; modeled –dash

U component, cm/s; COR= 0.89 ME= –6.3 cm/s

V component, cm/s; COR= 0.90 ME=–15.4 cm/s

Figure 3.22. Upper panel shows buoy #39909 trajectories. Bottom graphs show validation for simulated tidal velocities (U – zonal and V – meridian components) against observed U and V components of buoy drift. COR – correlation coefficient between observed and simulated velocities; ME – mean error.

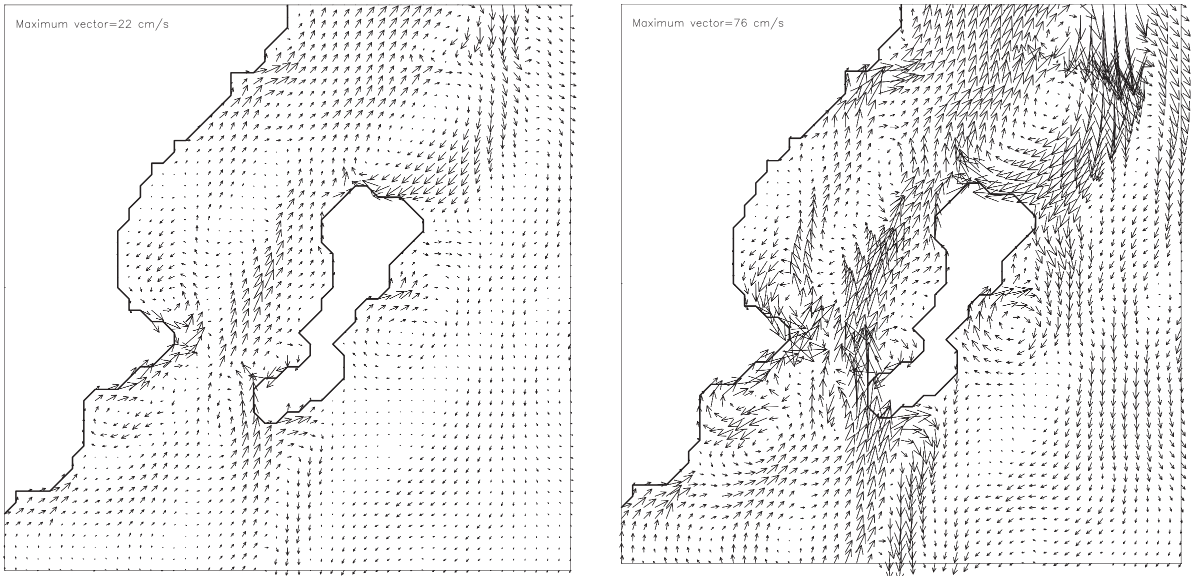

Figure 3.23. Residual tidal circulation around Kalgin Island. Left: under M2 tidal forcing; Right: under M2, S2, K2, N2, 2N2, K1, O1, and P1 tidal waves.

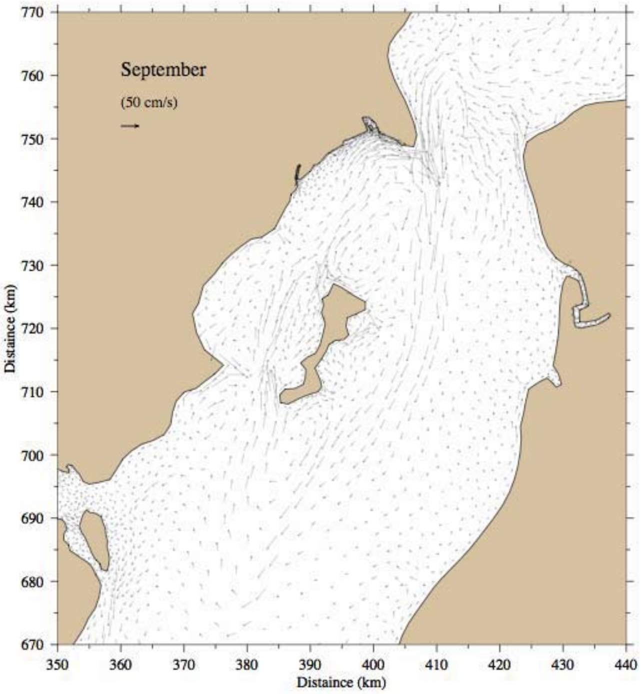

Figure 3.24. (same as Figure 2.7) Surface sub-tidal currents due to water temperature and salinity fields simulated by the 3-D model of Cook Inlet.

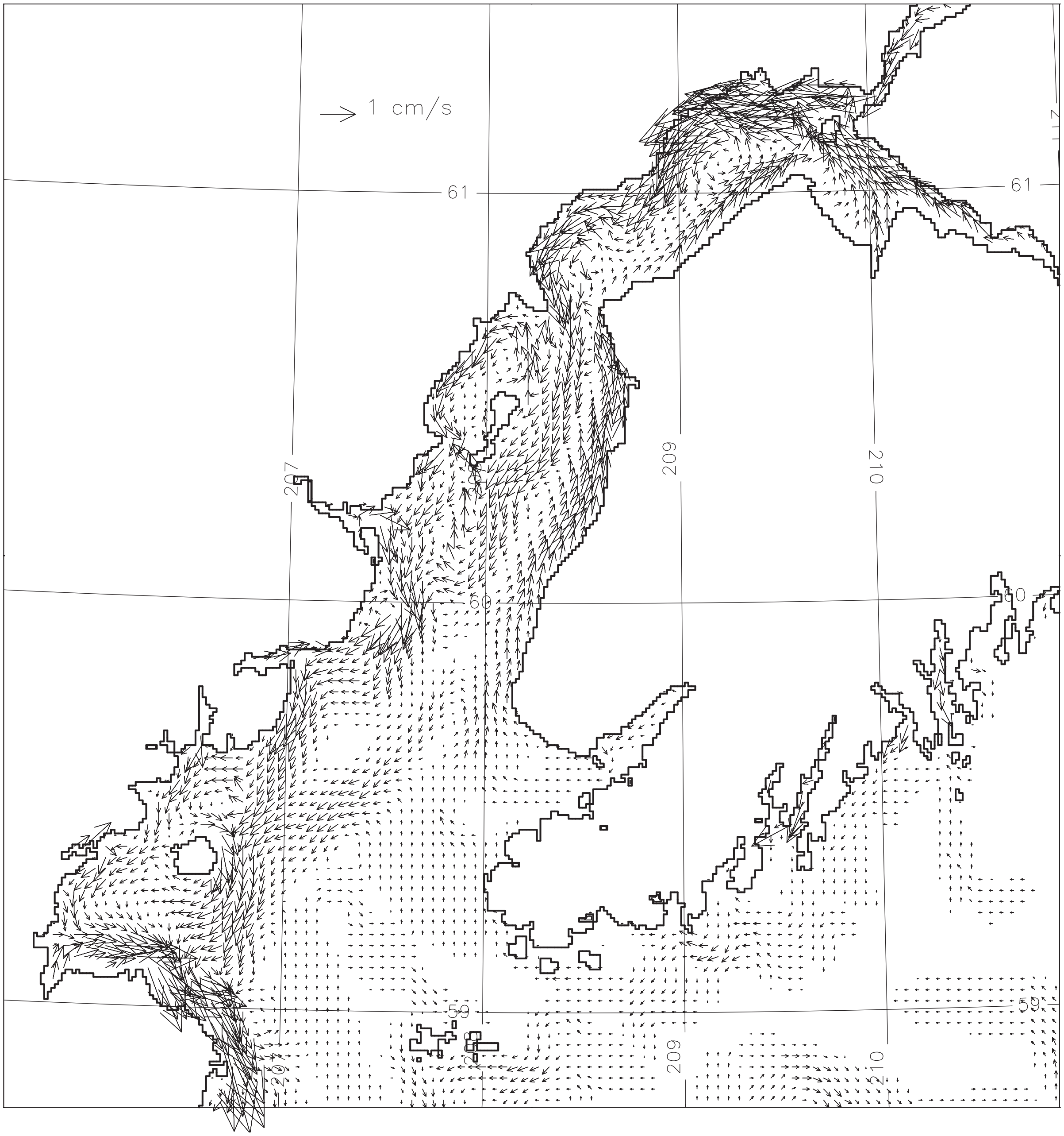

Figure 3.25. Simulated water circulation in Cook Inlet forced by river discharge. Note southward flow along western coasts and northward flow along eastern coast. Comparing with Figure 3.1 (left) allows us to conclude that river runoff is responsible for a general outflow of Cook Inlet waters to the Pacific Ocean.

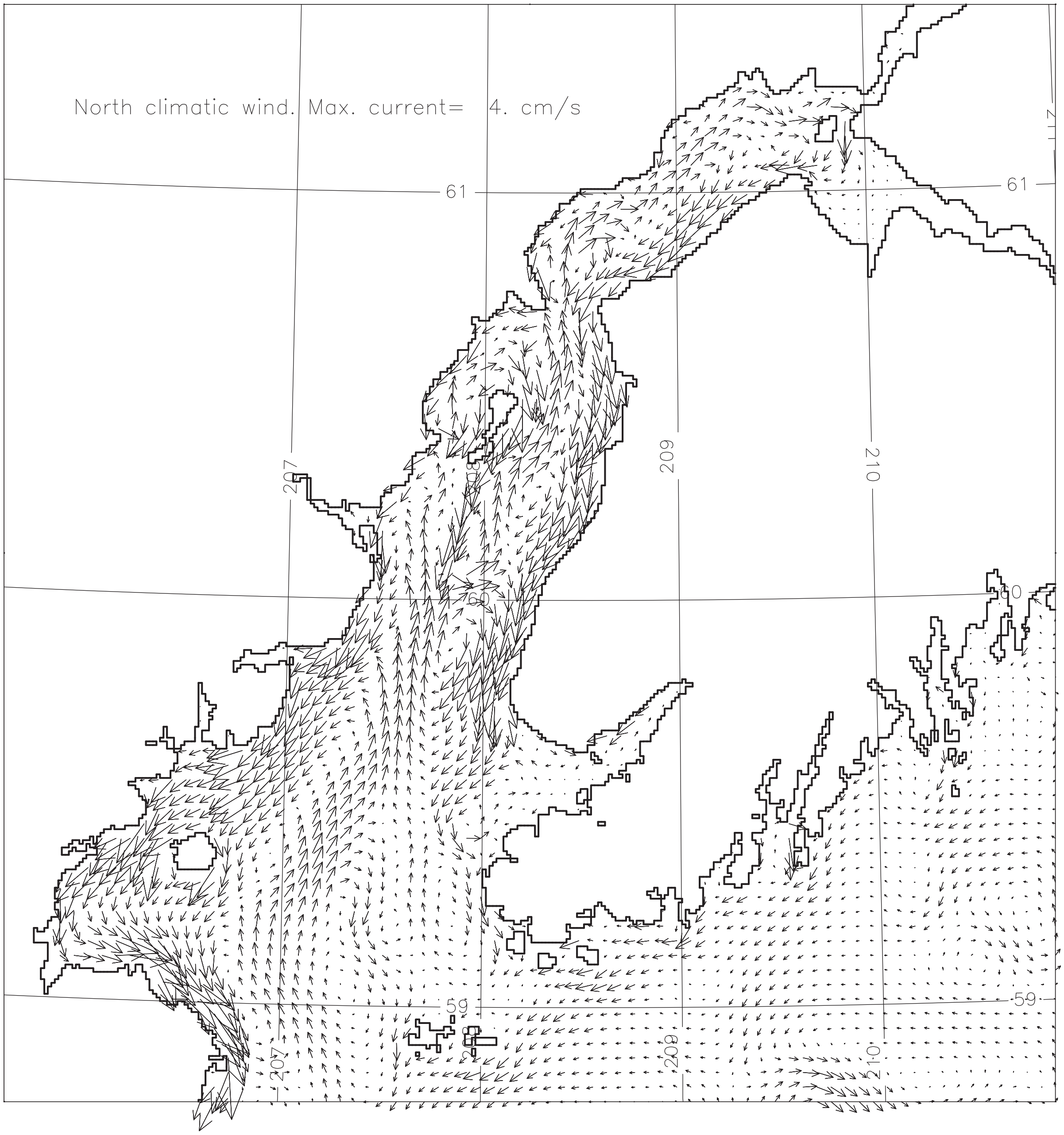

Figure 3.26. Simulated vertically averaged water circulation under climatic north wind (see Table 3.4).

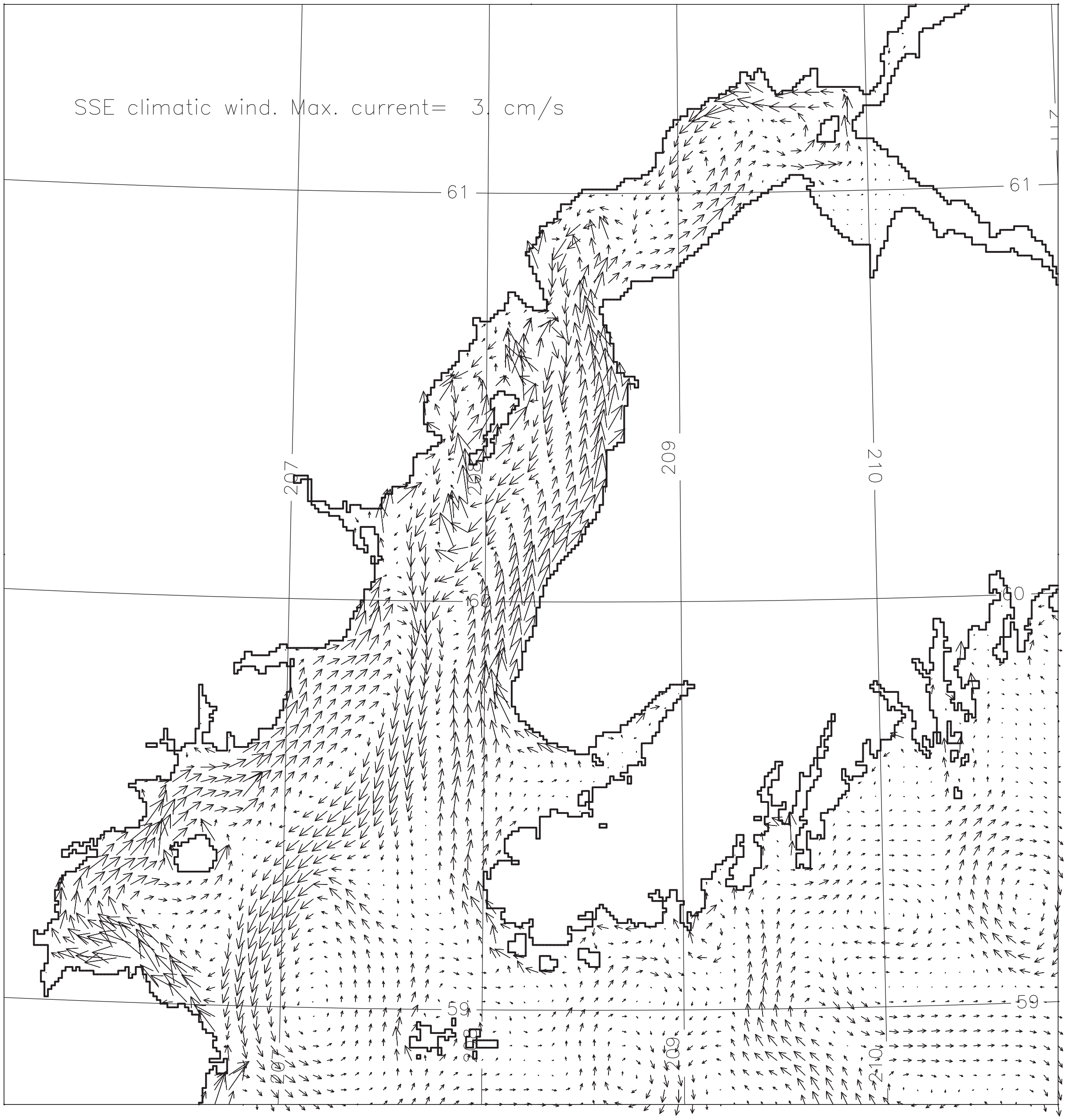

Figure 3.27. Simulated vertically averaged water circulation under climatic SSE wind (see Table 3.4).

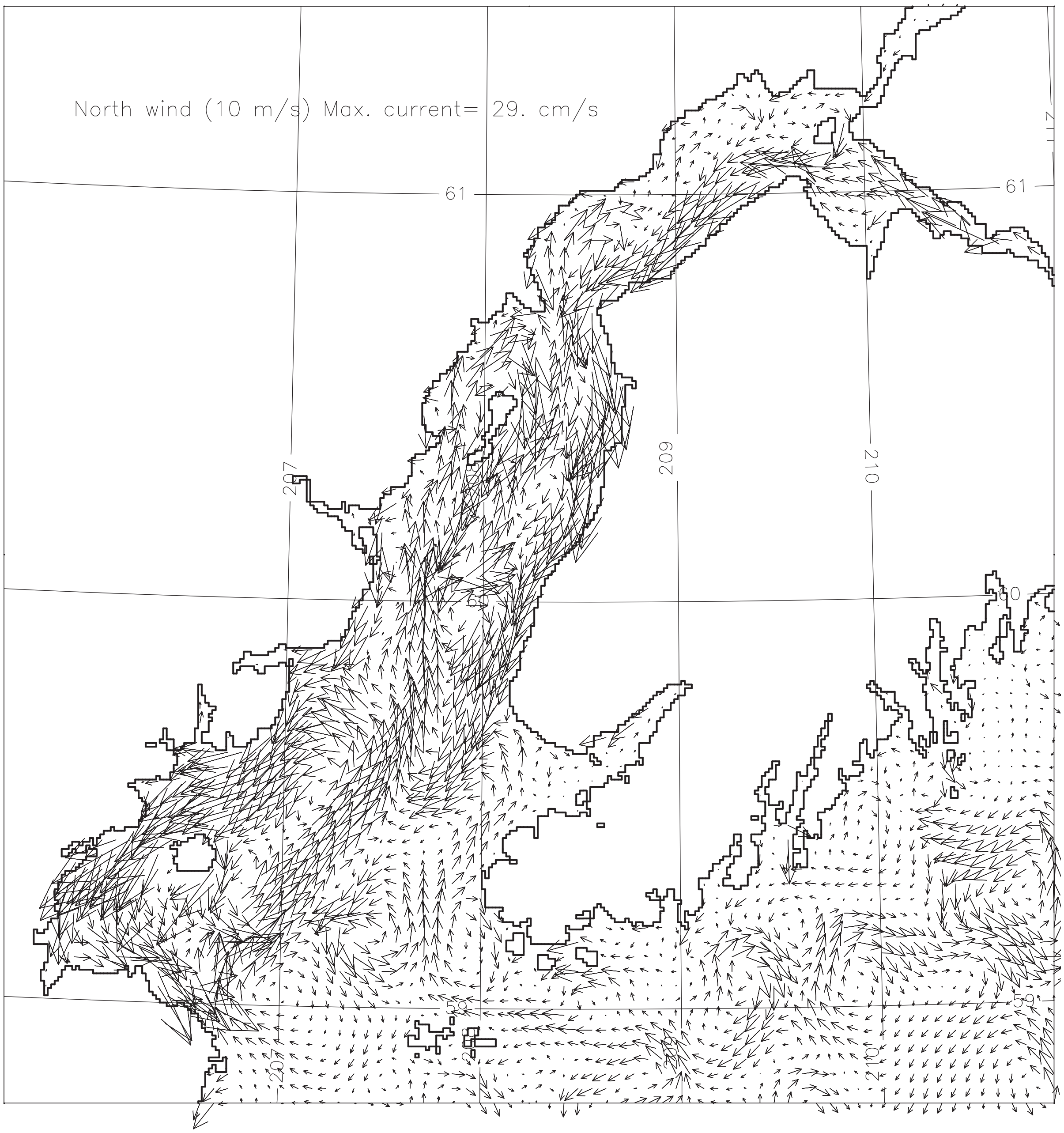

Figure 3.28. Simulated vertically averaged water circulation under north 10 m/s wind.

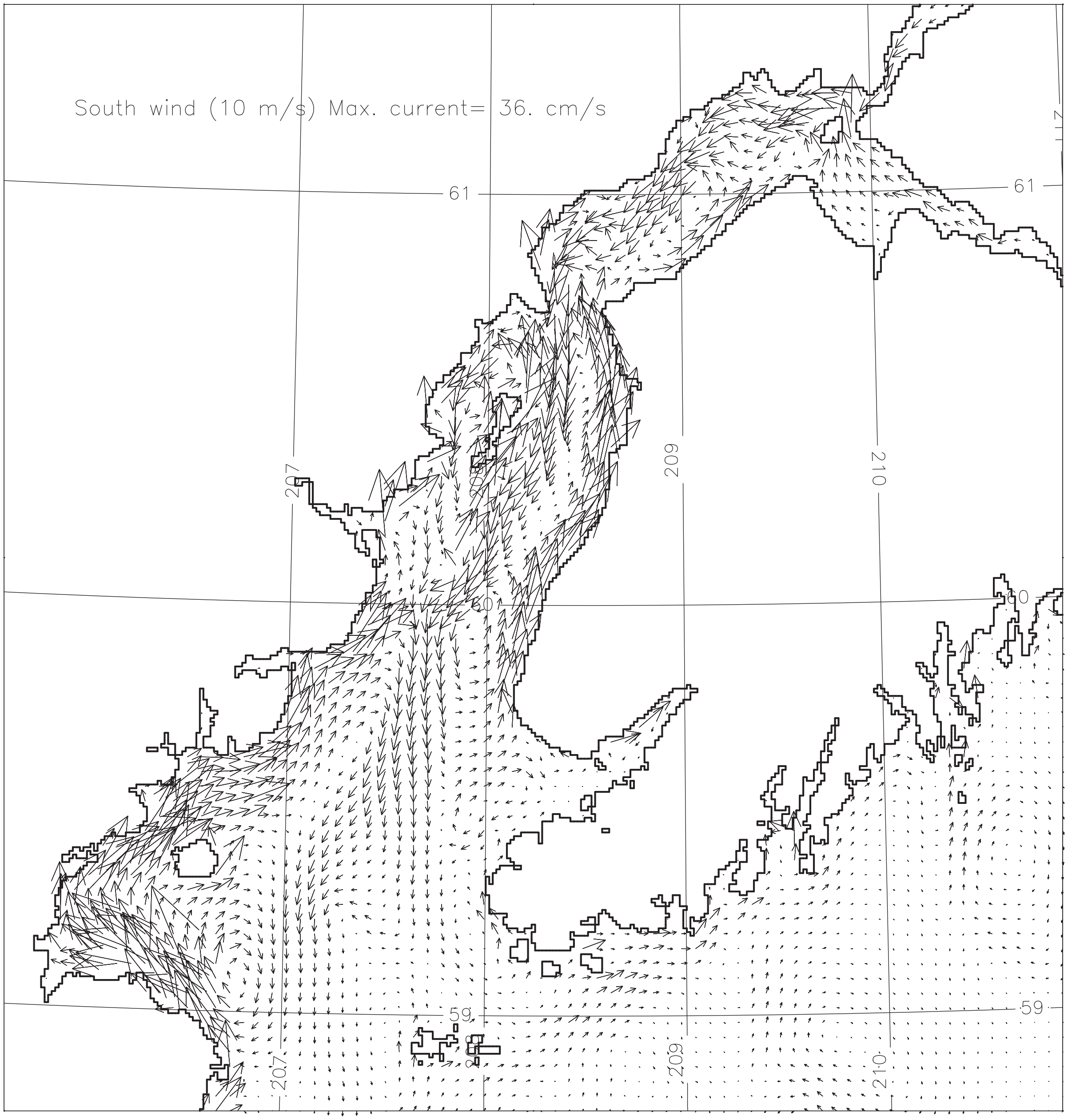

Figure 3.29. Simulated vertically averaged water circulation under south 10 m/s wind.

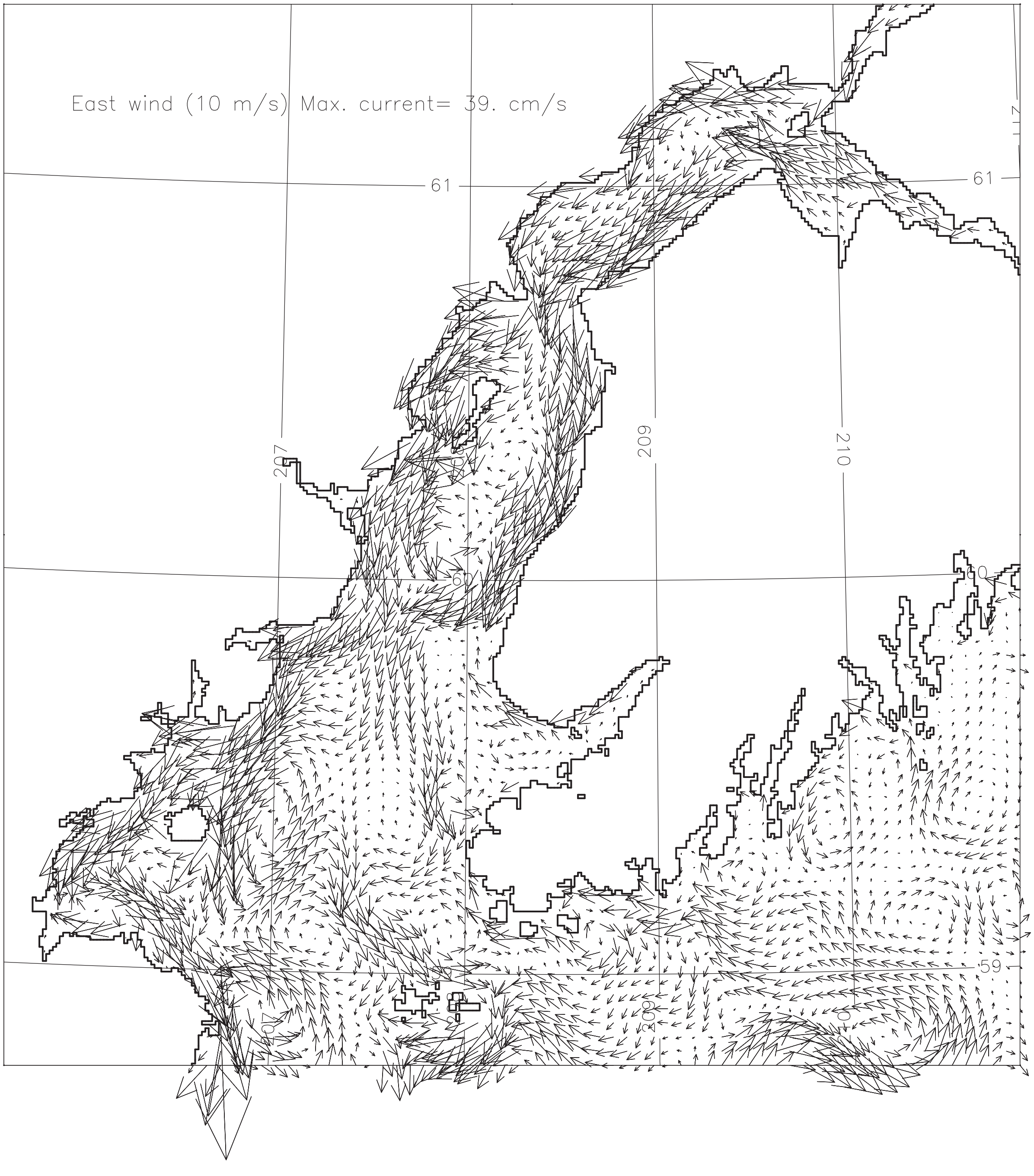

Figure 3.30. Simulated vertically averaged water circulation under east 10 m/s wind.

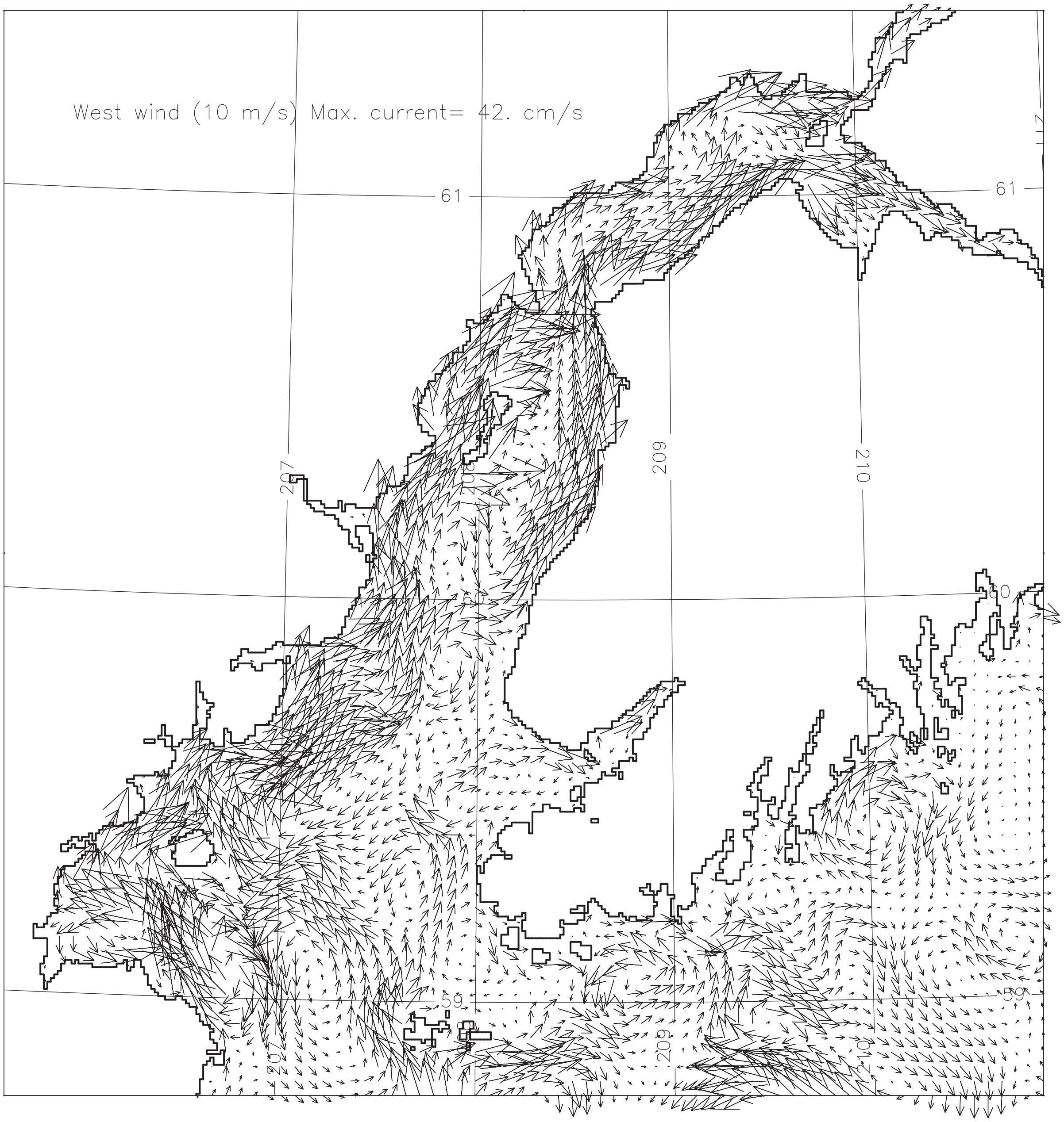

Figure 3.31. Simulated vertically averaged water circulation under west 10 m/s wind.

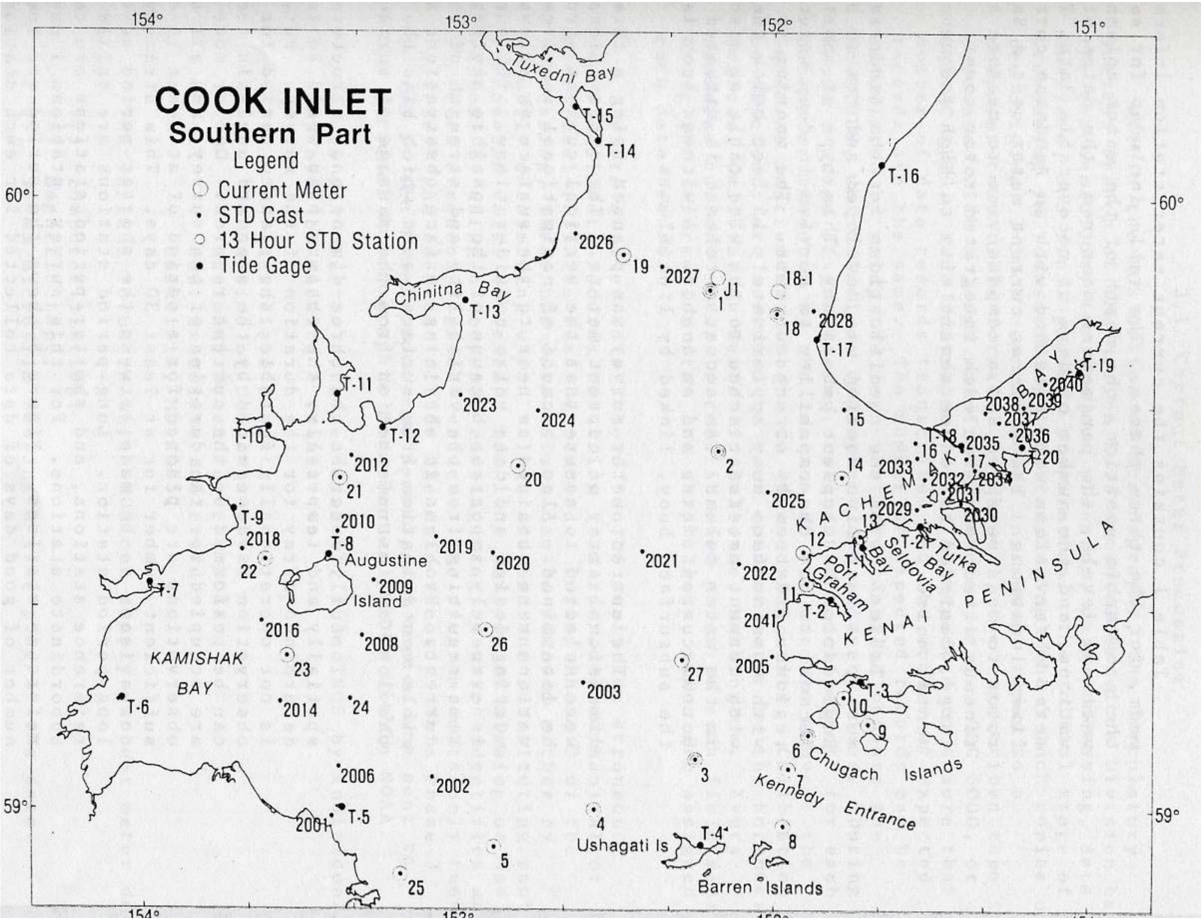

Figure 3.32. Locations of current meters and tide gauges in the NOAA circulatory survey of Cook Inlet in 1973-75. Note that all tide gauge data were lost because of fire in NOAA's arcives. In order to improve model results it is recommended repeating observations of sea levels and currents at stations 25, 5, 4, 3, 6, 9 and 10 for a period of at least one month. Year-round observations are preferable.

Chapter 4: SAR Data Processing

Introduction

This chapter summarizes the results on what might arguably be the signature circulation features in central Cook Inlet, the tide rips. Within the broad goals of improving our understanding of Cook Inlet circulation and improving the capabilities of numerical circulation models, this satellite-based component of the project focuses on tide rips, oceanographic frontal zones characterized by strong velocity shears and very strong convergences (Johnson et al., 2000). Cook Inlet tide rips act as migratory pathways for salmon returning to inlet tributaries to spawn and as forage sites for sea birds. Of particular importance and relevance with respect to MMS framework issues is, and as was demonstrated in the immediate aftermath of the 1987 grounding of the *T/V Glacier Bay*, the propensity of the tide rips to collect, advect, and submerge spilled oil.

Summary

Wintertime synthetic aperture radar imagery was used to identify prominent convergence zones locally known as tide rips in central Cook Inlet. Drifting sea ice tends to collect along tide rip fronts, creating large, readily detectable spatial gradients in radar backscatter. The locations of the maximum spatial gradients in backscatter were assumed to be proxies for the locations of convergence zones. Prominent convergences were observed to occur along the flanks of channels and shoals. The locations of these observed convergence zones were in very good agreement with the locations predicted by a simple analytical model derived from the continuity equation.

Fronts are typically associated with convergence zones. In Cook Inlet, drifting sea ice tends to collect along tide rip fronts thereby providing strong visual signatures for frontal locations. Radar backscatter (brightness) from sea ice is typically larger than from open water. As a consequence, the ice edge (frontal) location exhibits a relatively large spatial gradient in radar backscatter. Spatial brightness gradients are computed from SAR imagery and the locations of the largest gradients (assumed to represent frontal locations) are written to file.

Objectives

The objectives for this component of the project were to identify times and locations during the semidiurnal tidal cycle at which tide rip fronts characteristically occur. The more specific objective was to then use this information to ascertain the dynamics governing the temporal and spatial evolution of Cook Inlet tide rips.

The strategy employed to meet these objectives involved using a satellite-based platform to provide synoptic observations of Cook Inlet and, in so doing, mitigate some of the significant logistical and sampling limitations associated with vessel-based in situ oceanographic surveys. Synthetic aperture radar (SAR) satellites provide all-weather imaging capabilities because cloud cover does not affect image acquisition.

Because radar backscatter (brightness) from sea ice is typically much larger than from open water, wintertime imagery was used to detect tide rip fronts. In Cook Inlet, drifting sea ice tends to collect along tide rip fronts creating large, readily detectable spatial gradients in radar backscatter. The locations of the maximum brightness gradients are assumed to be proxies for the tide rip locations. Although Haley et al. (2000) also used SAR imagery to investigate Cook Inlet tide rip fronts, their analyses were somewhat hampered because the imagery they used was acquired during ice free months when frontal signatures were relatively weaker.

Methodology

Seasonal sea ice is typically observed in upper and central Cook Inlet from late December through March, with ice concentrations generally greatest in January and February. RadarSat SAR images were browsed (fermi.jhuapl.edu/sar/stormwatch/web_wind/) to identify dates on which appreciable sea ice was present in central Cook Inlet. Twenty-six images, acquired between January 2000 and March 2004 (Table 4.1), were selected for analyses and identification of frontal features.

RadarSat standard beam imagery (12.5 m pixel,

Table 4.1. Dates of SAR image acquisition and the corresponding temporal offset (hours) of the image acquisition time from the time of high tide at the mouth of the Kenai River.

Image Date	Image time (hrs) relative to high tide at Kenai River mouth
25 JAN 04	-5.55
18 JAN 04	-5.01
01 JAN 04	-3.90
15 JAN 00	-2.63
15 JAN 04	-2.05
29 DEC 03	-1.57
04 FEB 02	-1.41
12 FEB 00	-1.22
26 JAN 00	-0.61
04 JAN 02	-0.33
18 FEB 02	-0.10
27 MAR 04	0.10
25 JAN 04	0.80
10 MAR 04	1.21
08 FEB 00	1.54
15 JAN 02	1.66
08 FEB 04	1.71
19 FEB 00	3.19
06 MAR 04	3.47
28 JAN 02	3.61
25 FEB 02	4.34
11 JAN 02	4.52
03 MAR 00	4.53
19 JAN 00	4.61
17 MAR 04	5.17
02 JAN 00	5.71

normal processing) of the central Cook Inlet area was ordered on compact discs for these twenty-six dates from the Alaska Satellite Facility (ASF), University of Alaska Fairbanks. ASF supplied information for each scene in three files: metadata (.M extension), geographic/orbital information (.L extension), and the radar backscatter (.D extension). While the .L file provided the longitudes and latitudes corresponding to the corner pixels in the .D file, the backscatter image (.D file) itself was not georeferenced. That is, geographic positions were not imbedded/associated with individual image pixels, nor was the image rotated/warped to a map projection.

ENVI software was used to reference the pixel-based radar images of Cook Inlet to geographic coordinates. Generally, eight to ten ground control points (GCPs) were identified in each image (i.e. the longitudes and latitudes were associated with specified image pixels). Four of the GCPs were the image corners and the remaining GCPs typically included headlands and/or the middle tanker dock at Nikiski. These GCPs constrained the warping of the image within a common domain (152.8°W-150.4°W, 59.7°N-60.9°N), fixed grid (0.0004° longitude x 0.0002° latitude pixels, i.e. ~ 22 m x 22 m pixels) map projection (geographic lat/lon, WGS-84 datum). The georeferenced images were saved in GeoTIFF format. Figure 4.1 shows a representative SAR image warped to map coordinates within the geographic domain of interest.

Accomplishments

The large tidal range and energetic tidal currents

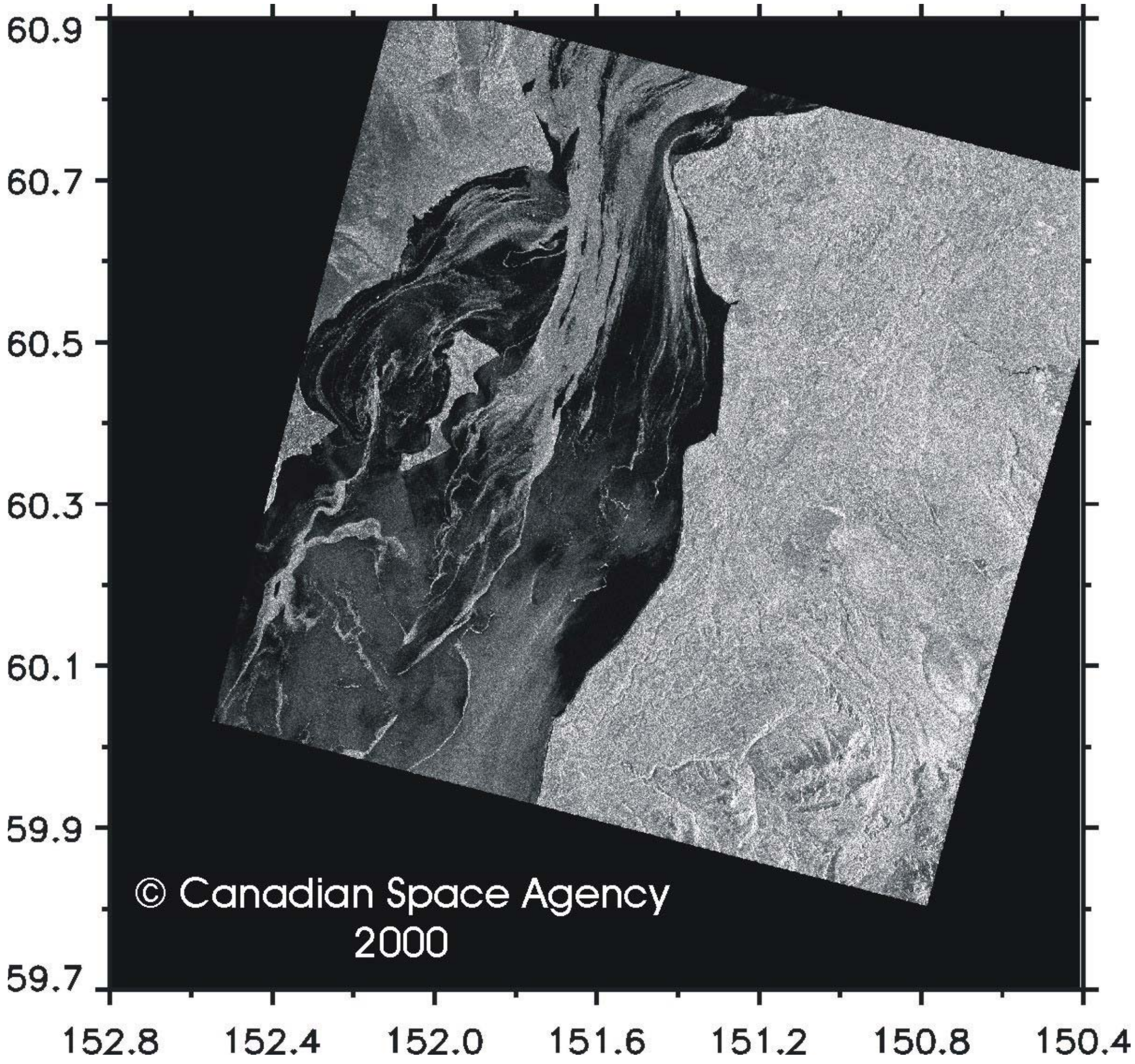

Figure 4.1 Radarsat image of central Cook Inlet, 8 February 2000. Plot axes show north latitudes and west longitudes of the geographic domain.

encountered in Cook Inlet break the sea ice into largely free-floating chunks that collect along convergence zones. The surface of broken sea ice is much rougher than that of open water and, as a consequence, the radar return from sea ice is much larger than that from open water making ice appear bright in a radar image (Figure 4.1). The validity of the present strategy for identifying the locations of tide rips from radar imagery depends on the degree to which the sharp gradient between ice and water is indicative of an oceanic front.

The along-channel axis of Cook Inlet is roughly oriented south-southwest to north-northeast and, as Figure 4.1 illustrates, most ice edge features (frontal proxies) are similarly oriented. Consequently, the geographic locations of the ice edges/fronts in each SAR image can be located numerically by computing the zonal (west-to-east) gradient in pixel brightness and selecting those locations at which the absolute values of the gradients are large (Figure 4.2).

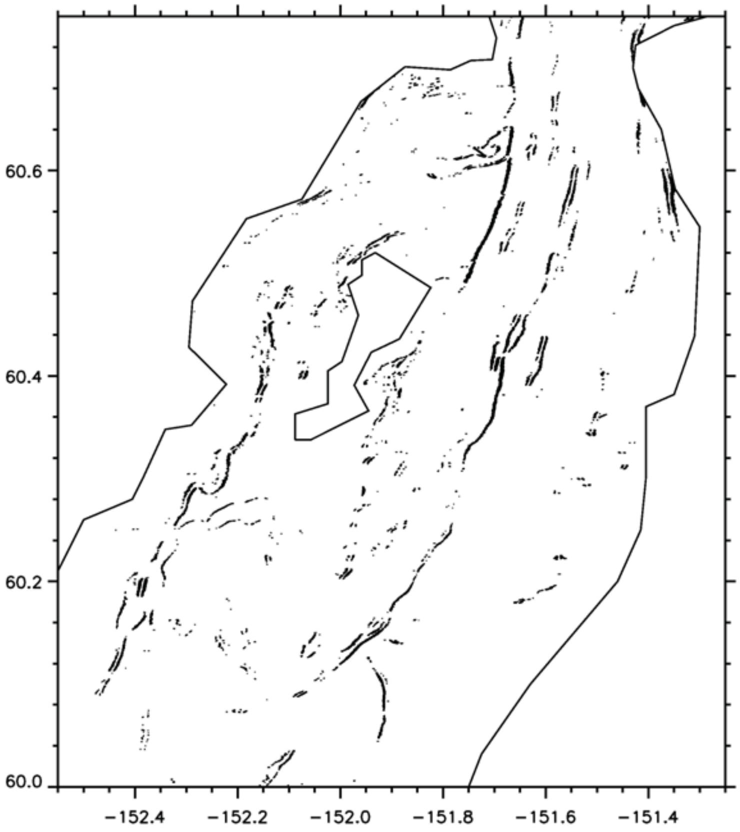

Figure 4.2. Plot showing the ice edge locations numerically identified from the 8 Feb 2000 SAR image in Figure 4.1. The solid lines delineate the boundaries of the terrestrial and intertidal mask.

This process was repeated for all images and the number of images in which an ice edge front was detected in each 510 m x 510 m (23 pixel x 23 pixel) bin was recorded. The aggregate record of ice edge front locations provides a generalized representation of convergence zones in central Cook Inlet (Figure 4.3). The most pronounced convergence/frontal feature extends southward from near the West Foreland to the northeast side of Kalgin Island whereupon the front turns south-southwestward to run along the east side of Kalgin Island. This frontal feature is known locally as the 'West Rip'. A somewhat weaker frontal feature, 'the Middle Rip', lies about 7 km east of the West Rip extends southwestward from the East Foreland becoming progressively less well defined. Other moderately prominent fronts occur between Harriet Point and the southern end of Kalgin Island and between the northern end of Kalgin Island and West Foreland where a zonal-oriented convergence zone intersects the West Rip.

It is common knowledge among Cook Inlet fishermen and mariners that the strength of the tide rips vary with the tidal stage. A hydrographic survey conducted by Okkonen (2005) described the semidiurnal evolution of the three principal tide rips (West, Middle, and East Rips) lying between Kalgin Island and the eastern side of the inlet. The strongest and most variable hydrographic gradients were associated with the West Rip. The hydrographic survey also indicated that the West and Middle Rip convergences

Figure 4.3. Plot showing the distribution of ice edge detections in each 0.0092° longitude x 0.0046° latitude (510 m x 510 m) bins. Only bins with two or more ice edge detections are shown. The solid lines delineate the boundaries of the terrestrial and intertidal mask.

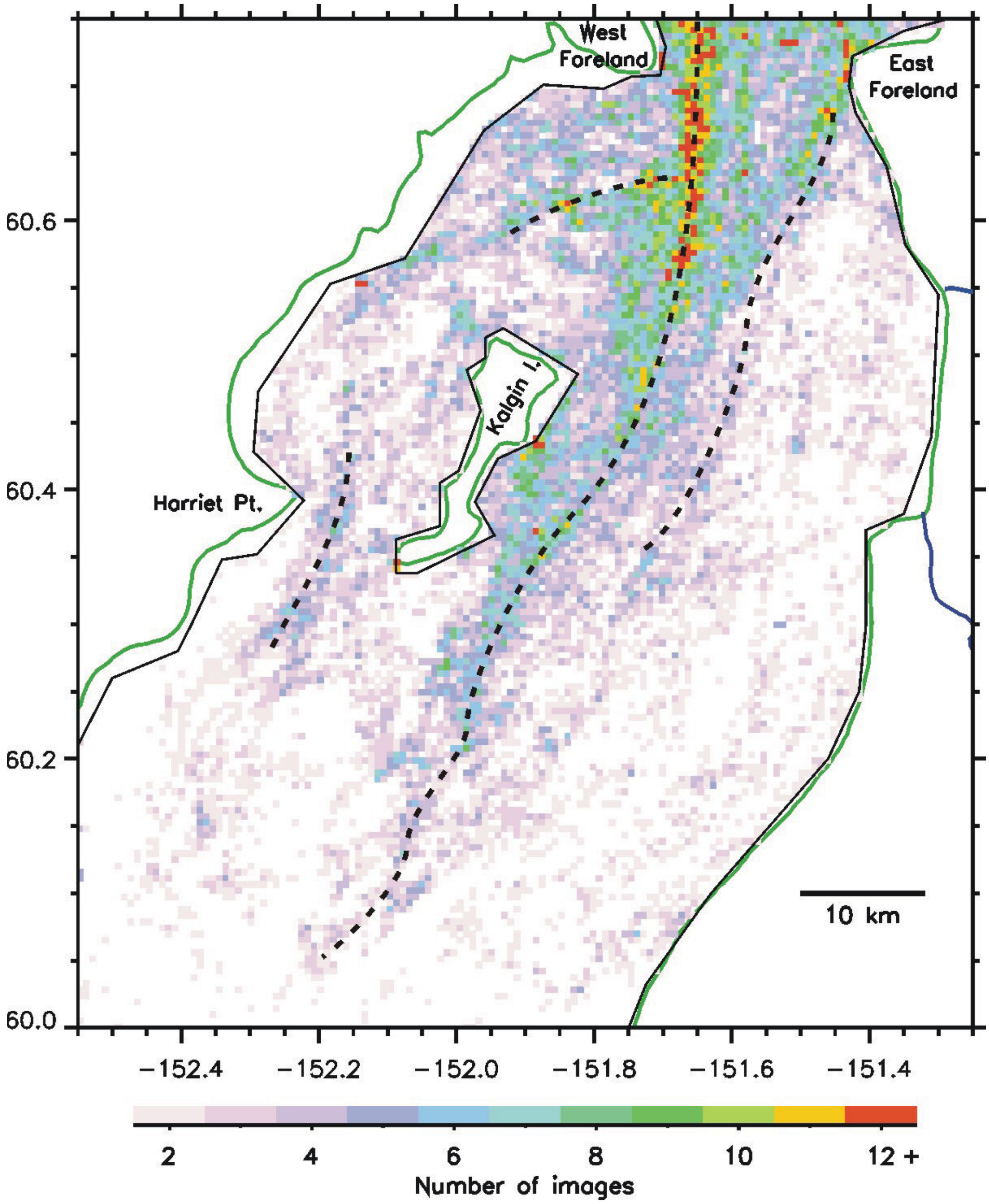

were strongest a few hours after high tide (as measured at the mouth of the Kenai River) whereas the East Rip was strongest during the first few hours after low tide.

A simple characterization of the phase relationships associated with the tide rips was obtained from the ensemble of SAR images in which ice edge fronts were detected. The temporal offset between the

Figure 4.4. Plot showing the average temporal offsets relative to the time of high tide at the mouth of the Kenai River in each 510 m x 510 m (0.0092° longitude x 0.0046° latitude) bins. Only bins with two or more ice edge detections are shown. High tide corresponds to a 0.0 hour offset. Low tide occurs at +/- 6.2 hours. The black dotted lines show the locations of the tide rips as identified in Figure 4.3. The solid gray line shows an inferred tide rip location associated with a temporal offset of 3-5 hours after high tide. It should be noted that high tide near the southern edge of the plot domain (60°N) occurs about an hour earlier than high tide at the mouth of the Kenai River.

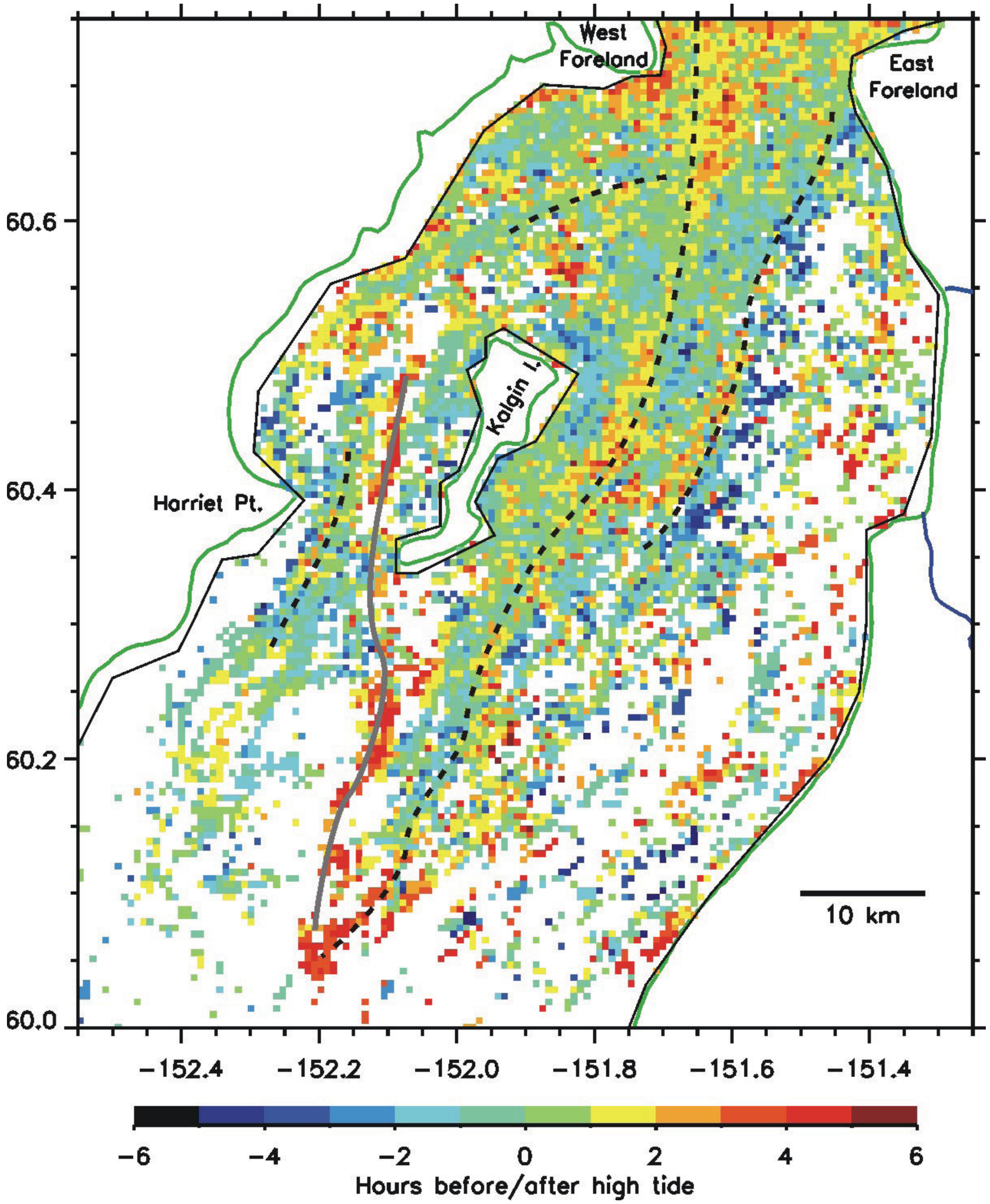

Figure 4.5. Bathymetry of central Cook Inlet overlaid with rip locations inferred from SAR Imagery.

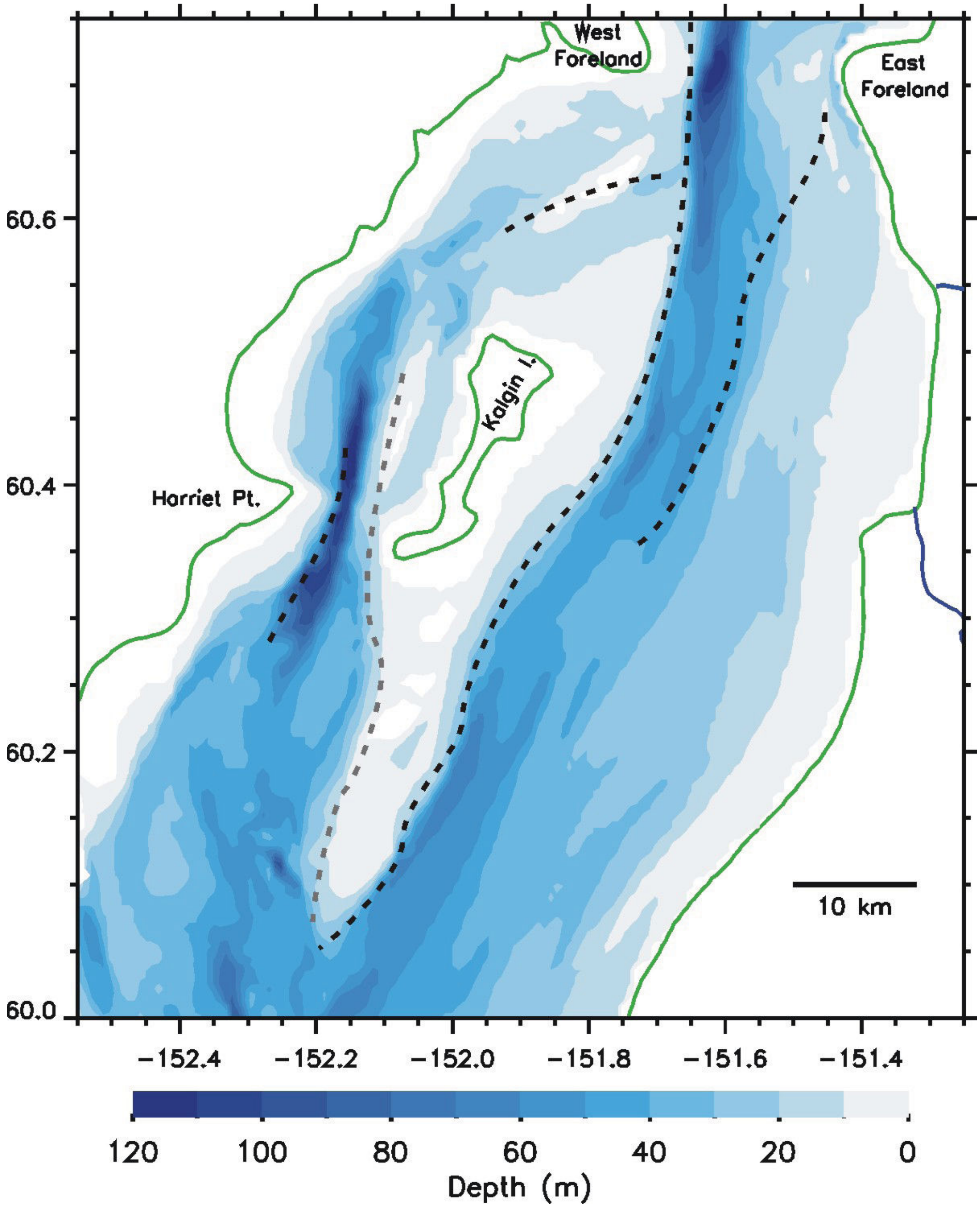

image acquisition time and the time of high tide at the mouth of the Kenai River (151.29°W, 60.55°N) was determined for each of the twenty-six images listed in Table 4.1. Within each 510 m x 510 m bin for which there were two or more images in which an ice edge front was detected (Figure 4.3), the average of the individual temporal offsets associated with those images (from Table 4.1) was computed. These average temporal offsets, which are interpreted to represent the times (relative to high tide at the Kenai River mouth) at which frontal features are strongest, are depicted in Figure 3.4.

Figure 4.6. Magnitude of the depth-scaled zonal bathymetric gradient (1/h dh/dy) overlaid with rip locations inferred from SAR imagery.

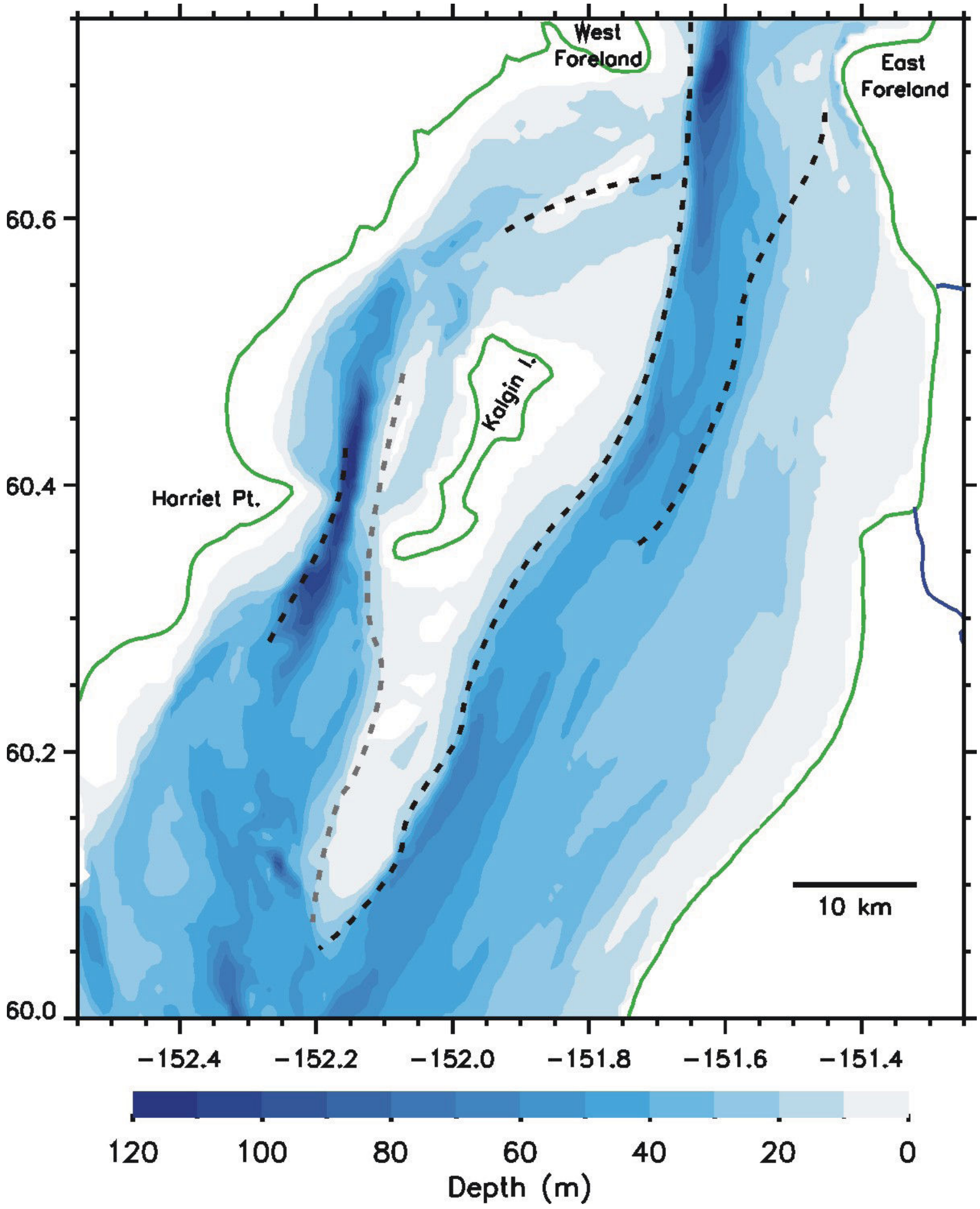

Although the plot is noisy, some quasi-linear frontal features are suggested. The most extensive of these fronts corresponds to the West Rip identified in Figure 4.3. The West Rip is indicated to be strongest from ~1-4 hours after high tide.

The Middle Rip location which extends south-southwestward from near the East Foreland appears to correspond to a frontal region along which the side immediately to the west of the rip is strongest 1-4 hours after high tide and along which the side immediately to the east of the rip is strongest 2-5 hours before high tide. The fronts between Kalgin Island and the West Foreland and between Kalgin Island and Harriet Point, as identified in Figure 4.3, do not appear to have readily identifiable temporal offset signatures in Figure 4.4. However, the existence of a separate frontal feature residing to the west and south of Kalgin Island (solid gray line) and inclined a few degrees from the 151.15°W meridian is inferred from its temporal offset signature (3-5 hours after Kenai high tide).

Tide Rip fronts: governing dynamics

In addition to the relationship between tidal stage and strength of the tide rips mentioned above, Cook Inlet drift gillnet fishermen have long noted an association between the locations of tide rips and changes in the underlying bathymetry. These associations provide starting points for investigating the governing dynamics. Figure 3.5 shows the locations of tide rips inferred from the SAR imagery (cf. Figures 3.3 and 3.4) overlaid on the bathymetry of the central Cook Inlet region. It is readily apparent that the rips lie along the flanks of channels and shoals.

While there are many papers that address aspects of fronts (rips) in estuaries, two papers in particular (Valle-Levinson et al., 2000a and Valle-Levinson et al., 2000b) capture the essential dynamics applicable to the formation of tide rips in Cook Inlet. The continuity equation can be restated in terms of the cross-channel velocity gradient (convergence/divergence), $\partial v/\partial y$

$$\frac{\partial v}{\partial y} = -\frac{v}{h}\frac{\partial h}{\partial y} - \frac{\partial u}{\partial x} - \frac{1}{h}\frac{\partial \zeta}{\partial t} \qquad \text{Equation 1}$$

Here the x-axis corresponds to the along-channel direction, the y-axis corresponds to the cross-channel direction, h is the water depth, and ζ is the sea level. The first term on the right-hand side of equation 1 is proportional to product of the cross-channel component of tidal velocity and the cross-channel bathymetric slope, the second term describes the along-channel gradient of the along-channel component of tidal velocity, and the last term is proportional to the time rate of change in tidal elevation. Representative tidal velocities in Cook Inlet are 2-3 m s^{-1} along-channel and 0.1-1.0 m s^{-1} cross-channel. A representative tidal range is 5 m. Using these values and depths from Figure 4.5, the first term in equation 1 scales as 10^{-4} to 10^{-3} whereas the second and third terms scale as 10^{-5}. Consequently, for conditions in Cook Inlet, the first term on the right hand side of equation 1 is the dominant factor controlling the rips. This means that the strongest convergences will occur where there are steep bathymetric slopes and when cross-channel tidal currents are strongest.

Rip locations identified from the SAR imagery agree very well with locations at which values of 1/h dh/dy are large (Figure 4.6). Although there was not a rip feature identified in the SAR imagery corresponding to the relatively steep bathymetric gradient feature that parallels the coast on the eastern side of the inlet, the ‘East Rip’ does occur along this feature. Because warmer oceanic water intrudes northward along the east side of the inlet, sea ice is less prevalent locally and a weaker radar signature associated with the East Rip results.

Remarks and Recommendations

The satellite-based component of this project demonstrates that the dynamics governing the locations of tide rips in Cook Inlet are relatively simple and that the rip locations are associated with steep bathymetric slopes. The implication for realistic modeling of tide rips is that a high-resolution digital bathymetry is required. Changes in the bathymetry due to natural or other causes would therefore influence the location of the rips. Figure 4.3 suggests that the West Rip convergence and the convergence zone between Kalgin Island and the West Foreland may be major aggregation areas. In Figure 4.3, one also sees red-colored bins (one on the east side of Kalgin Island (near 151.88W, 60.44N) and one near the south end of Kalgin Island (near 152.08W, 60.34N) that mark locations that are essentially the same locations at which drift cards were found on Kalgin in 2003 (see Okkonen, CMI final report OCS Study MMS 2003-036, Figure 15), again suggesting “keeper beaches”. Figure 4.3 also suggests that the east side of Kalgin Island could be heavily oiled in the event of a spill.

References

Haley, B. et al. 2000. Mapping Cook Inlet rip tides using local knowledge and remote sensing. LGL Alaska Research Associates, Inc. et al., OCS Study MMS 2000-025. US Department of the Interior, Minerals Management Service, Alaska OCS Region, 56 pp.

Johnson, M.A., S. Okkonen, and S. Sweet. 2000. Modern velocity data from Cook Inlet. Report to Cook Inlet Regional Citizen's Advisory Council. 16 pp.

Okkonen, S.R. 2005. Observations of hydrography and currents in central Cook Inlet, Alaska during diurnal and semidiurnal tidal cycles. Final Report. OCS Study MMS 2004-058. US Department of the Interior, Minerals Management Service, Alaska OCS Region, 27 pp.

Appendix:

Comparison results of simulated and observed tidal ellipses

Table 1. M2 ellipse characteristics: calculated (Calk, cm/s) and Observed (Obs, cm/s); major half-axis (max) and minor half axis (min); azimuth angle major axis (degree) and tidal vector rotation (Rot; 1 – clockwise and 0 – counterclockwise).

Stat	I	K	max		min		Dir		Rot	Lat	Lon
#			Calc	Obs	Calc	Obs	Calc	Obs		N, deg	degree
1.	199	137	95.6	97.9	6.6	10.4	15.9	6.6	1.0	59.863	207.807
2.	232	132	48.3	75.1	2.3	2.5	14.9	10.0	1.0	59.566	207.725
3.	286	132	55.4	50.6	21.2	11.8	355.4	308.0	1.0	59.081	207.736
4.	294	115	22.3	25.0	5.7	1.2	356.1	314.0	1.0	59.007	207.441
5.	301	96	16.2	18.2	3.6	2.1	175.9	152.0	1.0	58.941	207.113
6.	282	153	89.4	85.1	11.4	3.3	360.0	312.0	1.0	59.119	208.101
7.	288	150	76.0	68.1	15.6	13.1	179.4	130.0	1.0	59.065	208.050
8.	298	148	57.4	84.6	1.6	3.5	179.9	129.0	0.0	58.975	208.016
9.	280	164	76.8	146.2	0.0	3.4	266.4	272.0	1.0	59.138	208.294
12.	245	153	61.6	107.5	1.9	3.0	180.1	140.0	1.0	59.451	208.098
14.	234	160	32.0	35.0	4.1	9.7	179.6	142.0	0.0	59.550	208.220
15.	222	159	32.3	40.2	13.1	4.4	348.3	315.0	1.0	59.658	208.201
17.	230	182	22.2	18.0	7.0	2.1	4.9	320.0	0.0	59.586	208.610
18.	204	148	85.3	71.0	7.9	1.2	191.9	160.0	1.0	59.819	208.004
19.	193	121	82.2	99.0	13.1	7.0	19.3	22.0	1.0	59.916	207.520
20.	231	101	49.7	56.4	4.6	20.5	37.7	44.0	1.0	59.571	207.176
22.	248	55	37.0	36.1	0.1	10.9	43.4	50.0	0.0	59.408	206.372
25.	306	79	7.8	19.9	1.5	10.3	349.1	333.0	1.0	58.893	206.820
26.	261	95	29.1	4.5	4.4	2.1	21.1	350.0	0.0	59.300	207.081
27.	267	132	34.5	67.3	0.7	11.1	0.6	14.0	0.0	59.252	207.732
29.	173	116	0.0	78.0	0.0	3.0	0.0	330.0	0.0	60.094	207.424
30.	170	126	82.6	82.5	2.6	3.4	191.5	198.0	1.0	60.122	207.603
31.	175	132	96.1	99.9	2.5	1.6	189.3	190.4	1.0	60.078	207.713
33.	187	151	94.0	121.6	12.5	1.4	199.8	200.0	1.0	59.972	208.056
34.	169	152	120.4	136.7	13.5	18.6	208.3	210.2	1.0	60.134	208.071
36.	142	139	163.6	174.0	3.9	4.3	192.9	194.0	1.0	60.375	207.832
37.	146	155	121.3	147.5	14.7	10.0	210.1	212.0	1.0	60.340	208.123
38.	152	164	128.4	126.2	10.2	7.9	207.6	208.0	1.0	60.287	208.286
41.	134	138	118.2	96.5	5.2	1.8	356.2	358.0	1.0	60.447	207.813
42.	123	143	96.2	124.5	7.3	0.5	220.0	222.0	1.0	60.546	207.902
47.	117	163	118.7	166.9	5.1	20.7	231.0	234.0	0.0	60.601	208.266
48.	114	154	112.3	137.2	7.9	7.8	234.2	235.0	1.0	60.627	208.101
49.	102	168	218.5	194.1	1.8	1.5	178.6	171.0	1.0	60.736	208.357
50.	104	173	222.3	187.1	3.0	16.8	12.2	17.0	1.0	60.718	208.449
51.	103	180	131.9	188.0	2.6	10.0	201.8	188.0	1.0	60.727	208.577
52.	108	180	140.0	190.0	3.5	3.7	171.4	173.0	0.0	60.682	208.577
53.	94	187	146.8	156.0	9.7	0.1	238.0	234.0	1.0	60.807	208.705
54.	90	185	146.2	188.7	14.3	5.6	55.8	54.5	0.0	60.843	208.669
55.	83	178	112.7	170.5	14.0	0.7	233.7	236.0	0.0	60.906	208.540
67.	62	231	120.9	130.9	74.1	3.5	247.3	260.0	0.0	61.091	209.523
68.	67	232	140.2	167.3	34.9	5.9	64.2	72.0	0.0	61.046	209.540
69.	65	236	133.5	218.0	48.1	2.1	275.3	281.0	0.0	61.063	209.615
77.	52	244	135.8	182.5	28.1	0.1	63.2	66.0	0.0	61.179	209.768
81.	47	253	106.1	9.0	95.1	5.4	321.1	340.0	0.0	61.222	209.937
82.	49	253	89.7	155.1	43.7	7.2	64.8	105.0	0.0	61.204	209.937
83.	51	253	37.4	116.3	12.8	4.7	80.5	51.0	1.0	61.186	209.936
84.	48	256	122.5	163.7	0.0	7.2	264.3	253.0	0.0	61.213	209.993
85.	47	256	120.8	153.1	54.0	2.0	81.0	86.5	0.0	61.221	209.993
86.	46	256	129.2	147.8	78.7	6.1	90.0	84.0	0.0	61.230	209.994
87.	46	259	144.7	136.0	65.5	3.9	209.4	253.0	0.0	61.230	210.049
88.	44	260	162.8	165.5	53.9	4.0	195.3	237.0	0.0	61.247	210.069
89.	44	261	120.3	197.7	26.6	7.9	203.7	200.0	0.0	61.247	210.088
90.	45	262	44.1	99.1	0.0	3.8	223.6	204.0	0.0	61.238	210.105
93.	42	262	128.8	181.0	17.6	1.6	18.7	20.0	0.0	61.265	210.107

Table 2. S2 ellipses characteristics: calculated (Calk, cm/s) and Observed (Obs, cm/s); major half-axis (max) and minor half axis (min); azimuth angle major axis (degree) and tidal vector rotation (Rot; 1 – clockwise and 0 – counterclockwise).

Stat	I	K	max		min		Dir		Rot	Lat	Lon
#			Calc	Obs	Calc	Obs	Calc	Obs			
1.	199	137	41.4	35.0	0.6	2.0	17.4	18.1	0.0	59.863	207.807
2.	232	132	29.2	26.9	0.6	0.5	8.5	5.8	0.0	59.566	207.725
3.	286	132	18.8	21.9	7.9	1.3	321.5	304.0	1.0	59.081	207.736
4.	294	115	8.6	11.2	2.6	1.8	330.1	308.0	1.0	59.007	207.441
5.	301	96	6.2	8.2	1.7	1.4	154.4	140.5	1.0	58.941	207.113
6.	282	153	29.0	33.2	14.0	2.1	320.4	320.0	1.0	59.119	208.101
7.	288	150	21.9	26.5	11.3	5.0	325.1	312.0	1.0	59.065	208.050
8.	298	148	19.3	32.0	9.6	0.5	150.9	134.0	1.0	58.975	208.016
9.	280	164	6.6	45.7	0.0	2.5	268.1	275.0	1.0	59.138	208.294
12.	245	153	26.2	43.0	9.4	1.5	212.0	139.0	1.0	59.451	208.098
14.	234	160	11.8	14.4	2.2	2.2	8.4	47.0	1.0	59.550	208.220
15.	222	159	19.3	14.7	2.5	1.4	311.7	230.0	1.0	59.658	208.201
17.	230	182	6.8	7.1	1.7	1.0	183.0	247.0	1.0	59.586	208.610
18.	204	148	46.7	37.0	0.7	0.9	15.8	21.0	1.0	59.819	208.004
19.	193	121	40.9	33.0	1.1	2.3	21.9	21.0	0.0	59.916	207.520
20.	231	101	24.3	17.9	2.4	7.4	24.0	20.0	0.0	59.571	207.176
22.	248	55	12.5	10.5	3.0	4.4	31.4	38.8	0.0	59.408	206.372
25.	306	79	4.5	10.2	0.3	4.7	341.2	330.0	1.0	58.893	206.820
26.	261	95	15.1	6.7	0.6	4.8	5.1	323.0	0.0	59.300	207.081
27.	267	132	22.3	24.2	1.4	1.0	350.0	15.0	1.0	59.252	207.732
29.	173	116	0.0	26.0	0.0	1.2	0.0	326.0	0.0	60.094	207.424
30.	170	126	35.2	29.9	0.9	3.5	194.2	207.0	0.0	60.122	207.603
31.	175	132	38.3	32.3	0.5	1.3	192.4	188.8	0.0	60.078	207.713
33.	187	151	48.9	43.0	1.3	0.5	201.6	202.0	0.0	59.972	208.056
34.	169	152	47.0	42.4	3.6	4.5	207.6	213.0	0.0	60.134	208.071
36.	142	139	69.8	56.1	0.9	2.4	13.6	6.2	0.0	60.375	207.832
37.	146	155	51.8	45.8	6.6	2.9	29.7	35.2	0.0	60.340	208.123
38.	152	164	50.1	40.0	5.2	4.5	25.1	22.0	0.0	60.287	208.286
41.	134	138	45.7	27.1	1.1	2.1	180.1	172.0	1.0	60.447	207.813
42.	123	143	40.4	32.7	8.3	0.1	212.8	218.0	0.0	60.546	207.902
47.	117	163	62.6	44.7	16.5	3.4	215.0	232.0	0.0	60.601	208.266
48.	114	154	54.0	34.3	19.2	0.2	219.6	232.0	0.0	60.627	208.101
49.	102	168	75.3	51.7	1.9	2.1	178.3	174.0	0.0	60.736	208.357
50.	104	173	76.6	51.2	4.1	1.5	199.7	198.0	0.0	60.718	208.449
51.	103	180	73.7	53.5	0.3	2.8	23.9	7.0	0.0	60.727	208.577
52.	108	180	73.9	48.8	1.6	1.6	352.4	355.0	0.0	60.682	208.577
53.	94	187	72.9	46.9	27.4	0.5	44.3	53.0	0.0	60.807	208.705
54.	90	185	63.1	58.6	29.0	0.8	212.5	235.0	0.0	60.843	208.669
55.	83	178	47.1	51.5	21.0	2.1	212.3	232.0	0.0	60.906	208.540
67.	62	231	64.3	37.2	31.6	2.5	1.5	80.0	0.0	61.091	209.523
68.	67	232	65.1	38.7	32.4	0.7	238.2	254.0	0.0	61.046	209.540
69.	65	236	54.3	52.8	39.2	0.8	270.2	280.0	0.0	61.063	209.615
77.	52	244	30.3	58.9	18.6	1.4	43.3	65.0	0.0	61.179	209.768
81.	47	253	73.8	17.2	8.2	9.3	0.0	0.0	1.0	61.222	209.937
82.	49	253	34.8	47.4	0.8	1.9	180.1	235.0	1.0	61.204	209.937
83.	51	253	9.9	36.0	6.6	10.2	225.8	227.0	1.0	61.186	209.936
84.	48	256	13.3	36.7	0.0	2.8	270.1	250.0	0.0	61.213	209.993
85.	47	256	39.2	51.0	4.2	1.6	180.0	267.0	1.0	61.221	209.993
86.	46	256	56.0	41.2	1.7	1.8	0.0	85.0	1.0	61.230	209.994
87.	46	259	73.6	36.2	3.5	1.2	180.3	257.0	1.0	61.230	210.049
88.	44	260	90.3	56.1	6.1	0.3	180.4	220.0	1.0	61.247	210.069
89.	44	261	42.7	62.3	5.1	2.6	1.9	20.0	1.0	61.247	210.088
90.	45	262	6.8	25.5	0.0	0.2	221.1	202.0	0.0	61.238	210.105
93.	42	262	39.2	56.3	7.4	2.0	5.5	14.0	1.0	61.265	210.107

Table 3. K1 ellipses characteristics: calculated (Calk, cm/s) and Observed (Obs, cm/s); major half-axis (max) and minor half axis (min); azimuth angle major axis (degree) and tidal vector rotation (Rot; 1 – clockwise and 0 – counterclockwise).

Stat	I	K	max		min		Dir		Rot	Lat	Lon
#			Calc	Obs	Calc	Obs	Calc	Obs			
1.	199	137	13.0	11.2	0.3	0.7	12.5	5.0	1.0	59.863	207.807
2.	232	132	10.2	7.0	0.5	0.7	10.5	14.0	0.0	59.566	207.725
3.	286	132	7.7	5.3	1.7	0.8	302.6	301.0	0.0	59.081	207.736
4.	294	115	3.9	4.1	0.9	0.9	317.4	301.0	0.0	59.007	207.441
5.	301	96	3.1	3.1	0.5	0.5	327.1	266.0	0.0	58.941	207.113
6.	282	153	11.3	7.7	0.2	3.5	307.5	308.0	0.0	59.119	208.101
7.	288	150	9.3	7.9	0.1	1.2	301.2	299.0	0.0	59.065	208.050
8.	298	148	8.8	9.6	1.1	0.2	307.3	298.0	1.0	58.975	208.016
9.	280	164	9.0	4.9	0.0	0.7	265.3	257.0	0.0	59.138	208.294
12.	245	153	8.2	7.7	2.4	0.1	216.9	233.0	1.0	59.451	208.098
14.	234	160	2.5	3.0	0.5	0.1	193.9	204.0	1.0	59.550	208.220
15.	222	159	3.7	4.5	1.7	1.2	165.0	124.0	1.0	59.658	208.201
17.	230	182	1.9	2.6	0.3	1.0	50.6	54.0	1.0	59.586	208.610
18.	204	148	12.9	9.2	0.2	0.1	13.1	17.0	1.0	59.819	208.004
19.	193	121	13.4	7.8	0.3	0.8	22.2	30.0	1.0	59.916	207.520
20.	231	101	8.8	8.0	0.8	5.1	19.2	18.0	0.0	59.571	207.176
22.	248	55	3.9	5.2	0.8	1.1	21.4	46.0	0.0	59.408	206.372
25.	306	79	2.1	5.2	0.1	0.4	348.2	343.0	0.0	58.893	206.820
26.	261	95	6.2	5.6	0.2	1.6	354.3	27.0	1.0	59.300	207.081
27.	267	132	9.1	8.3	0.3	2.1	344.7	346.0	1.0	59.252	207.732
29.	173	116	0.0	4.7	0.0	0.5	330.0	330.0	0.0	60.094	207.424
30.	170	126	11.8	9.3	0.3	0.6	13.1	11.2	0.0	60.122	207.603
31.	175	132	13.7	12.1	0.1	2.2	190.5	205.0	0.0	60.078	207.713
33.	187	151	12.9	11.0	0.3	0.8	22.1	33.0	1.0	59.972	208.056
34.	169	152	13.7	12.7	0.4	1.6	30.5	42.8	0.0	60.134	208.071
36.	142	139	18.0	16.1	0.3	2.4	13.3	3.6	1.0	60.375	207.832
37.	146	155	13.9	16.0	0.4	4.0	29.1	25.7	1.0	60.340	208.123
38.	152	164	14.4	14.2	0.7	0.8	27.0	19.3	0.0	60.287	208.286
41.	134	138	14.4	9.2	0.1	4.6	2.4	7.4	1.0	60.447	207.813
42.	123	143	10.7	11.9	0.9	0.6	41.0	40.5	1.0	60.546	207.902
47.	117	163	14.5	6.5	1.2	3.4	58.1	53.6	1.0	60.601	208.266
48.	114	154	11.2	8.9	1.9	0.4	62.0	51.7	1.0	60.627	208.101
49.	102	168	29.7	10.1	0.6	1.1	182.4	192.6	0.0	60.736	208.357
50.	104	173	23.1	10.8	0.5	3.1	12.4	194.0	1.0	60.718	208.449
51.	103	180	11.2	11.4	0.3	0.7	29.3	0.0	1.0	60.727	208.577
52.	108	180	9.1	9.5	0.3	0.8	344.4	359.0	0.0	60.682	208.577
53.	94	187	18.6	8.4	1.6	1.3	234.1	225.0	1.0	60.807	208.705
54.	90	185	15.6	12.9	0.4	0.9	233.9	240.0	0.0	60.843	208.669
55.	83	178	10.3	6.7	0.6	2.1	54.1	54.0	0.0	60.906	208.540
67.	62	231	13.5	6.8	2.5	1.0	66.3	85.0	1.0	61.091	209.523
68.	67	232	14.4	8.2	2.4	1.6	246.2	263.1	1.0	61.046	209.540
69.	65	236	8.7	7.2	5.4	2.8	86.0	95.6	1.0	61.063	209.615
77.	52	244	12.8	9.4	0.6	1.1	64.0	68.5	1.0	61.179	209.768
81.	47	253	16.6	2.5	2.1	2.1	91.7	58.7	0.0	61.222	209.937
82.	49	253	13.6	11.3	0.1	1.5	242.6	227.3	1.0	61.204	209.937
83.	51	253	5.2	10.1	0.8	0.8	242.0	232.6	1.0	61.186	209.936
84.	48	256	22.7	11.8	0.0	0.1	265.1	256.0	0.0	61.213	209.993
85.	47	256	17.1	7.6	0.9	0.3	264.7	260.3	0.0	61.221	209.993
86.	46	256	19.0	6.3	1.1	0.8	270.0	261.0	0.0	61.230	209.994
87.	46	259	18.7	6.6	1.1	1.1	225.3	250.0	0.0	61.230	210.049
88.	44	260	17.9	9.4	0.8	1.0	219.1	232.2	0.0	61.247	210.069
89.	44	261	17.8	13.3	0.5	0.8	29.9	24.9	0.0	61.247	210.088
90.	45	262	7.9	7.3	0.0	0.2	223.4	199.9	1.0	61.238	210.105
93.	42	262	22.5	8.6	0.4	0.4	205.4	192.5	0.0	61.265	210.107

Table 4. O1 ellipses characteristics: calculated (Calk, cm/s) and Observed (Obs, cm/s); major half-axis (max) and minor half axis (min); azimuth angle major axis (degree) and tidal vector rotation (Rot; 1 – clockwise and 0 – counterclockwise).

Stat	I	K	max		min		Dir		Rot	Lat	Lon
#			Calc	Obs	Calc	Obs	Calc	Obs			
1.	199	137	13.0	11.2	0.3	0.7	12.5	5.0	1.0	59.863	207.807
2.	232	132	10.2	7.0	0.5	0.7	10.5	14.0	0.0	59.566	207.725
3.	286	132	7.7	5.3	1.7	0.8	302.6	301.0	0.0	59.081	207.736
4.	294	115	3.9	4.1	0.9	0.9	317.4	301.0	0.0	59.007	207.441
5.	301	96	3.1	3.1	0.5	0.5	327.1	266.0	0.0	58.941	207.113
6.	282	153	11.3	7.7	0.2	3.5	307.5	308.0	0.0	59.119	208.101
7.	288	150	9.3	7.9	0.1	1.2	301.2	299.0	0.0	59.065	208.050
8.	298	148	8.8	9.6	1.1	0.2	307.3	298.0	1.0	58.975	208.016
9.	280	164	9.0	4.9	0.0	0.7	265.3	257.0	0.0	59.138	208.294
12.	245	153	8.2	7.7	2.4	0.1	216.9	233.0	1.0	59.451	208.098
14.	234	160	2.5	3.0	0.5	0.1	193.9	204.0	1.0	59.550	208.220
15.	222	159	3.7	4.5	1.7	1.2	165.0	124.0	1.0	59.658	208.201
17.	230	182	1.9	2.6	0.3	1.0	50.6	54.0	1.0	59.586	208.610
18.	204	148	12.9	9.2	0.2	0.1	13.1	17.0	1.0	59.819	208.004
19.	193	121	13.4	7.8	0.3	0.8	22.2	30.0	1.0	59.916	207.520
20.	231	101	8.8	8.0	0.8	5.1	19.2	18.0	0.0	59.571	207.176
22.	248	55	3.9	5.2	0.8	1.1	21.4	46.0	0.0	59.408	206.372
25.	306	79	2.1	5.2	0.1	0.4	348.2	343.0	0.0	58.893	206.820
26.	261	95	6.2	5.6	0.2	1.6	354.3	27.0	1.0	59.300	207.081
27.	267	132	9.1	8.3	0.3	2.1	344.7	346.0	1.0	59.252	207.732
29.	173	116	0.0	4.7	0.0	0.5	330.0	330.0	0.0	60.094	207.424
30.	170	126	11.8	9.3	0.3	0.6	13.1	11.2	0.0	60.122	207.603
31.	175	132	13.7	12.1	0.1	2.2	190.5	205.0	0.0	60.078	207.713
33.	187	151	12.9	11.0	0.3	0.8	22.1	33.0	1.0	59.972	208.056
34.	169	152	13.7	12.7	0.4	1.6	30.5	42.8	0.0	60.134	208.071
36.	142	139	18.0	16.1	0.3	2.4	13.3	3.6	1.0	60.375	207.832
37.	146	155	13.9	16.0	0.4	4.0	29.1	25.7	1.0	60.340	208.123
38.	152	164	14.4	14.2	0.7	0.8	27.0	19.3	0.0	60.287	208.286
41.	134	138	14.4	9.2	0.1	4.6	2.4	7.4	1.0	60.447	207.813
42.	123	143	10.7	11.9	0.9	0.6	41.0	40.5	1.0	60.546	207.902
47.	117	163	14.5	6.5	1.2	3.4	58.1	53.6	1.0	60.601	208.266
48.	114	154	11.2	8.9	1.9	0.4	62.0	51.7	1.0	60.627	208.101
49.	102	168	29.7	10.1	0.6	1.1	182.4	192.6	0.0	60.736	208.357
50.	104	173	23.1	10.8	0.5	3.1	12.4	194.0	1.0	60.718	208.449
51.	103	180	11.2	11.4	0.3	0.7	29.3	0.0	1.0	60.727	208.577
52.	108	180	9.1	9.5	0.3	0.8	344.4	359.0	0.0	60.682	208.577
53.	94	187	18.6	8.4	1.6	1.3	234.1	225.0	1.0	60.807	208.705
54.	90	185	15.6	12.9	0.4	0.9	233.9	240.0	0.0	60.843	208.669
55.	83	178	10.3	6.7	0.6	2.1	54.1	54.0	0.0	60.906	208.540
67.	62	231	13.5	6.8	2.5	1.0	66.3	85.0	1.0	61.091	209.523
68.	67	232	14.4	8.2	2.4	1.6	246.2	263.1	1.0	61.046	209.540
69.	65	236	8.7	7.2	5.4	2.8	86.0	95.6	1.0	61.063	209.615
77.	52	244	12.8	9.4	0.6	1.1	64.0	68.5	1.0	61.179	209.768
81.	47	253	16.6	2.5	2.1	2.1	91.7	58.7	0.0	61.222	209.937
82.	49	253	13.6	11.3	0.1	1.5	242.6	227.3	1.0	61.204	209.937
83.	51	253	5.2	10.1	0.8	0.8	242.0	232.6	1.0	61.186	209.936
84.	48	256	22.7	11.8	0.0	0.1	265.1	256.0	0.0	61.213	209.993
85.	47	256	17.1	7.6	0.9	0.3	264.7	260.3	0.0	61.221	209.993
86.	46	256	19.0	6.3	1.1	0.8	270.0	261.0	0.0	61.230	209.994
87.	46	259	18.7	6.6	1.1	1.1	225.3	250.0	0.0	61.230	210.049
88.	44	260	17.9	9.4	0.8	1.0	219.1	232.2	0.0	61.247	210.069
89.	44	261	17.8	13.3	0.5	0.8	29.9	24.9	0.0	61.247	210.088
90.	45	262	7.9	7.3	0.0	0.2	223.4	199.9	1.0	61.238	210.105
93.	42	262	22.5	8.6	0.4	0.4	205.4	192.5	0.0	61.265	210.107